POLITECNICO DI TORINO

DEPARTMENT OF CONTROL AND COMPUTER ENGINEERING

Master's Degree in Mechatronic Engineering

MASTER'S DEGREE THESIS

Design and analysis of an Electromagnetic Automotive Suspension System with Finite Element Method for Energy Harvesting

Supervisor: **Prof. Maizza Giovanni**
Adviser: **Dr. Jamolov Umid**

Candidate:
Peccini Francesco

Academic Year 2019-2020

Abstract

Given the growing interest in electric mobility, and analysed its problems, we can notice that the most relevant is the one related to the range. For this reason, the development of innovative recovery systems, together with batteries, is essential for the advent of electric mobility.

Analysing deeply the method of energy recover we can see that the majority concern with the recovery of the kinetic energy, in particular of two methodologies: Regenerative Braking System and Energy Harvesting Suspension, the first is the best known (in fact in the last years was also commercialized) while the latter is less common, and so, the most interesting to study and develop.

By definition, energy recovery is the conversion of energy losses that we can observe in various stages of the processes, taking place in mechanical systems that are powered by an energy source in the way of available energy by means of specially designed devices and re-use if needed. The recovered/harvested energy can be used to start various electrical devices or to recharge the battery. The search for maximum energy recovery leads us to work in conditions of low damping, this leads us to deduce that our damper will have a variable behaviour depending on the road on which it is located, in particular, it will be preferred to make it works as a generator only in situations of low damping, i.e., on the motorways; while in the remaining conditions (i.e. high damping factor) it will have to work like classical shock absorber.

Regarding the model, the two main parts are stator and slider. In the first one there is a casing in which there are housed coils - in particular, a block of three since we want a three-phase output signal. The stator is the part where the eddy currents were generated, for that reason the coils are made of copper (material with very high electrical conductivity); after that the current is conveyed to the energy management systems of the vehicle itself.

The second one is the slider, here we can find the permanent magnets alternated by iron poles that are used to concentrate the magnetic flux and block physically the magnets - since they are threaded into the shaft. It is the relative motion of the slider with respect to the stator that generates the currents which we have already talked about.

Therefore, my thesis, starts from the analysis of the future mobility, understanding both its current advantages and limitations and trying to solve them. Moreover, it continues with a comparison among the various technologies present to date and ends with the development of an eddy current electromagnetic shock absorber to convert the kinetic energy into electrical ones, energy which would otherwise be dissipated in heat.
The whole development was done utilizing the Finite Element Method using COMSOL Multiphysics software.

Contents

Nomenclature

H	Magnetic Field Strength
$\vec{B}$	Magnetic Induction
μ_0	Vacuum Magnetic Permeability
μ	Magnetic Permeability
μ_a	Absolute Magnetic Permeability
M	Magnetization Vector
A	Area
SI	International Unit System
$\vec{B}_{tot}$	Total Magnetic Induction
$\vec{B}_0$	External Induction
χ	Magnetic Susceptibility
B_s	Magnetic Induction Saturation
B_r	Residual Magnetic Induction
H_c	Coercive Magnetic Field
PM	Permanent Magnet

BH_{max}	Maximum Potential Energy
B_x,B_y,B_z	Components of the Magnetic
SmCo	Samarium Cobalt
NdFeB	Neodymium Iron Boron
ε (or emf)	Electromotive Force
ϕ_b	Magnetic Flux
E, $E_{transformer}$, $E_{motional}$	Electromotive forces
J	Current Density
σ	Conductivity
v	Velocity between the permanent magnet and the conductor
F	Total Lorentz Force
F_z	Total Lorentz Force
r	Radial coordinate
z	Axial coordinate
τ	Pole Pitch
τ_m	PM height
R_{rod}	Rod radius

R_o	Outer radius
C	Damping coefficient
M_0	Magnetization per unit length
$E(k)$	Elliptic integral of the first kind
$K(k)$	Elliptic integral of the second kind
I	Equivalent current
δ	Depth of penetration
ω	Frequency of the system
Ω	Ohms
ρ	Resistivity
ω_n	Resonant frequency of the system
R_o	External diameter of the conductor
R_{ic}	Internal Diameter of the conductor
l	Total Length of the conductor
f	Frequency

Chapter 1

Introduction

1.1 Introduction

One of the greatest inventions of the modern era, and one that has contributed to the development of society by satisfying mobility of everyday life, is certainly the automobile. However, as we can see in Figure 1[1], in the next 50 years there will be an increase of global population from 6 billion to 10 billion and that will cause an increase of vehicles from 700 million to 2.5 billion. That large amount of vehicle around the world has caused continuous problems for the environment and human life, in particular Air pollution, global warming and depletion of Earth's resources, with our trend of oil discovery/consumption the world oil resource will be used by about 2038. [2] [3]

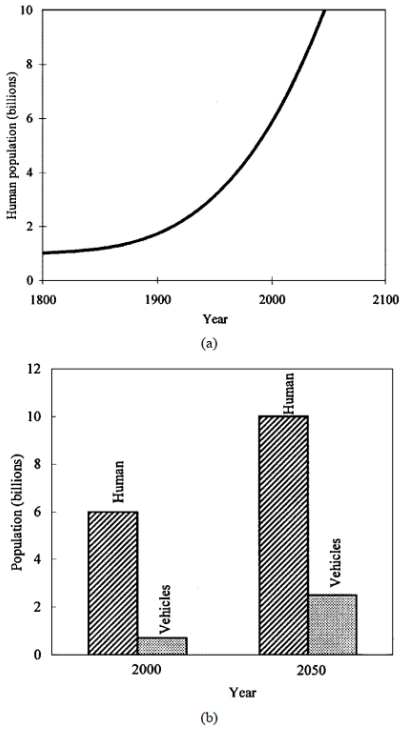

Figure 1: Growth of population and vehicles [1]

In the first chapter we saw how the introduction of the electric car will certainly be a necessary step for global mobility. In fact, without it, we will be facing an unsustainable world. As already seen, the main problems are related to the supply of fossil fuel and the pollution due from it, that's why, even if we can classify EVs as a road vehicle which involves electric propulsion, and so, including battery electric vehicles (BEVs), hybrid vehicles (HEVs), and fuel-cell electric vehicle (FCEVs); only the first technology is a real solution, and, therefore, more interesting to study.
Focusing on the BEV we can notice that the critical issue is the battery. Therefore, at the actual State of Art, BEV is mainly suitable for small EV for short-range low-speed transport. HEV can meet consumers' meet, but cost is the major issue.

1.2 Present and Future of EV's

1.2.1 Present Major Issues

Analysing deeply the world of the EVs we can notice that the major issue are the range (in Km) and the cost. The latter can be tackle improving EV subsystems, such as EV subsystems, such as electric motors, power converters, electronic controllers, energy management units, battery chargers, batteries, and other EV auxiliaries, as well as EV system-level integration and optimization [state of art]. The former instead with the development of advanced batteries (nickel-metal hydride (Ni-MH), zinc/air (Zn/Air), and lithium-ion (Li-Ion)) or energy recovery systems, such as Energy Harvesting Brakes or Energy Harvesting Damper. The latter is more interesting since the development point of view due there are not commercial products.

1.2.2 Development Trends

The figure 2 shows the development trends of EVs and HEVs, and as we can see, some core technologies can be shared among the different solutions. Our goal is the use of clean, efficient, and intelligent energy to achieve sustainable transportation system for the 21st century.[1]

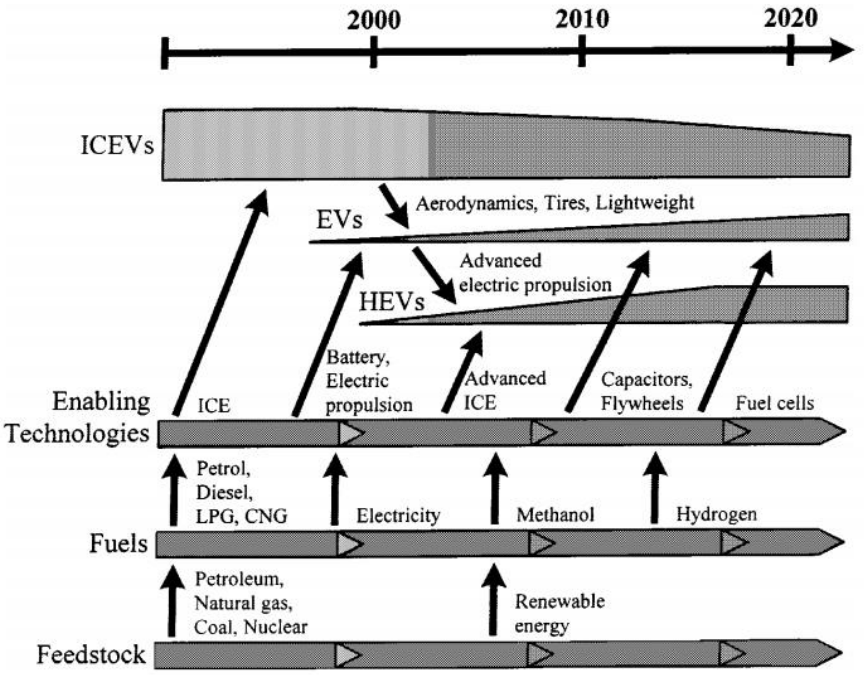

Figure 2: Development trends of EV's and HEV's (courtesy of EVAA)

Thanks to the growing interest, the transversal use of knowledge and accumulated years of development, EV are becoming mature. Nowadays we can benefit from the use of advanced IM drives and PM brushless motor drives improves the propulsion system, the advanced battery, as valve-regulated lead-acid (VRLA), Ni-MH and Li-Ion; the FCs and the ultracapacitor that improve a lot the energy source; the use of light materials; the study on aerodynamics; the adoption of advanced charging, power steering or variable temperature have allowed us to achieve good objectives in terms of range and power. Nevertheless, development is still moving, particularly in energy recovery systems that would otherwise be lost.

1.3 Engineer Philosophy

"The Engineering Philosophy essentially is the integration of automobile and electrical engineering. The system integration and optimization are prime considerations to achieve good EV performance at affordable cost. Since the characteristics of electric propulsion are fundamentally different from those of engine propulsion, a novel design

approach is essential for EV engineering. Moreover, advanced energy sources and intelligent energy management are key factors to enable EVs competing with ICEVs. Of course, the overall cost effectiveness is the fundamental factor for the marketability of EVs. The design approach of modern EVs should include state-of-the-art technologies from automobile engineering, electrical and electronic engineering, and chemical engineering, adopt unique designs particularly suitable for EVs, and develop special manufacturing techniques particularly suitable for EVs. Every effort should be made to optimize the energy utilization of EVs. The following points are those typical considerations for EV design.

1) Identify the niche market and environment.

2) Determine the technical specifications including the driving cycle.

3) Determine the infrastructure required including the recycling of batteries.

4) Determine the overall system configuration—BEV, HEV, or FCEV configurations.

5) Determine the chassis and body. 6) Determine the energy source—generation or storage, single or hybrid.

7) Determine the propulsion system—motor, converter, and transmission types, single or multiple motors, gearless or geared, mounting methods, and ICE systems in case of an HEV.

8) Determine the specifications of electric propulsion (power, torque, speed) and energy source (capacity voltage, current) according to various driving cycles; for example, Fig. 13 shows that the torque-speed requirement of the Federal Urban Driving Schedule (FUDS) is very different from that of the Federal Highway Driving Schedule (FHDS). In Fig. 13, the density of dots represents the frequency of operating condition. Hence, in FUDS, the powertrain often operates at low speed and high torque, while in FHDS, it operates at a high-speed low-torque profile.

9) Adopt intelligent EMS.

10) Analyse the interaction of EV subsystems by using the quality function matrix as shown in Fig. 3, hence, understanding the degree of interaction that affects the cost, performance, and safety.

11) Optimize the efficiency of the motor drive according to the selected driving pattern and operating conditions.

12) Optimize the overall system using computer simulation."[1]

1.4 Final consideration

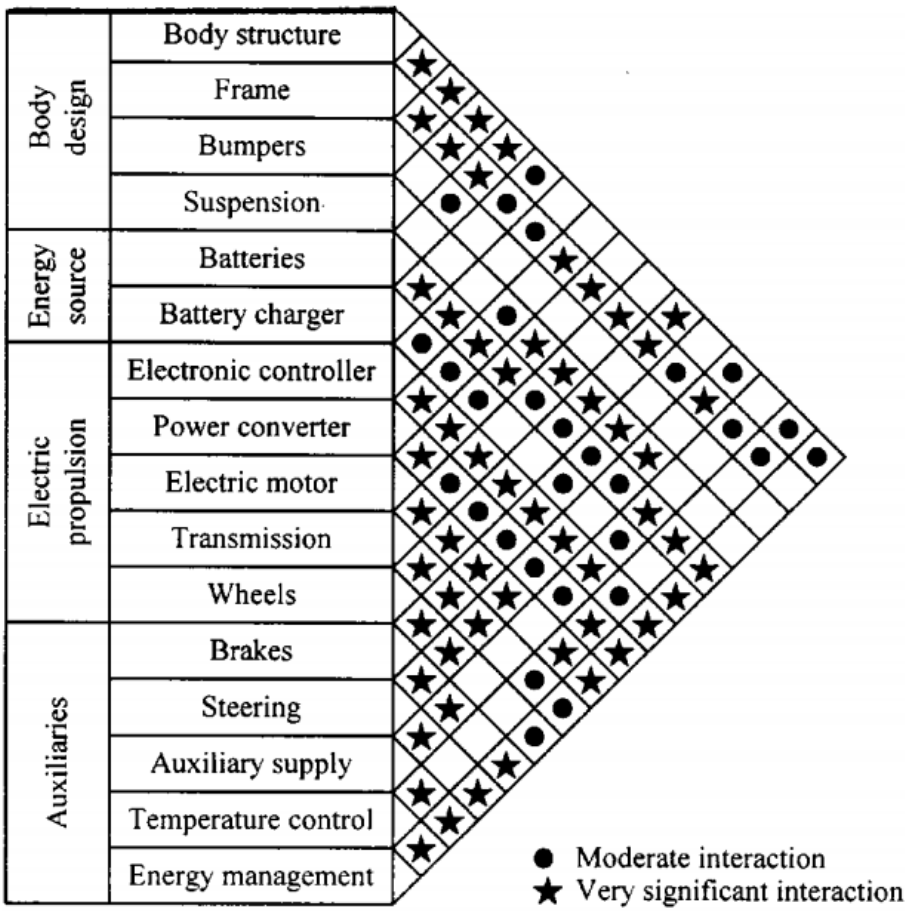

Figure 3: Interactions among EV subsystems [1]

As we can see from the table the Energy Management is one of the most important aspects of the Auxiliaries, that confirm the necessity to study deeply that aspect. “In conclusion, we can therefore summarize some important concept for EV: The EV is a road vehicle based on modern electric propulsion that consists of the electric motor, power converter, and energy source and it has its own distinct characteristics. The EV is not just a car, but a new system for our society, realizing clean and efficient road transportation. EV users’ expectations must be studied and, hence, appropriate education must be conducted.”[1]

“In summary, the system-level simulation and optimization of EVs should consider the following key issues.

1) As the interactions among various subsystems greatly affect the performance of EVs, the significance of those interactions should be analysed and taken into account.

2) As the model accuracy is usually coherent with the model complexity but may be contradictory to the model usability, trade-offs among the accuracy, complexity, and usability as well as simulation time should be considered.

3) As the system voltage generally causes contradictory issues for EV design, including the battery weight (higher voltage requires higher number of battery modules in series, hence more weight for the battery case), motor drive voltage and current ratings, acceleration performance, driving range and safety, it should be optimized on the system level.

4) In order to increase the driving range, multiple energy sources may be adopted for modern EVs. The corresponding combination and hybridization ratio should be optimized based on the vehicle performance and cost.

5) Since EVs generally adopt fixed gearing, the gear ratio can greatly affect the vehicle performance and drive- ability. An optimal ratio should be determined through iterative optimization under different driving profiles.”[1]

Chapter 2

Development Environment and Methodologies[4]

2.1 Introduction

The description of the laws of physics for space and time-dependent problems are usually expressed in terms of *partial differential equations* (PDEs). For many geometries and problems, these PDEs cannot be solved with analytical methods. Instead, an approximation of the equations can be constructed, typically based upon different types of *discretization's*. These discretization methods approximate the PDEs with *numerical model equations*, which can be solved using numerical methods. The solution to the numerical model equations is, in turn, an approximation of the real solution to the PDEs. The *finite element method* (FEM) is used to compute such approximations. Take, for example, a function u that may be the dependent variable in a PDE (i.e., temperature, electric potential, pressure, etc.) The function u can be approximated by a function u_h using linear combinations of basic functions according to the following expressions:

$$u \approx u_{\mathrm{h}} \tag{2.1}$$

and

$$u_{\mathrm{h}} = \sum_i u_i \varphi_i \tag{2.2}$$

Here, ψ_i denotes the basic functions and u_i denotes the coefficients of the functions that approximate u with u_h. The figure below illustrates this principle for a 1D problem. u could, for instance, represent the temperature along the length (x) of a rod

that is nonuniformly heated. Here, the linear basis functions have a value of 1 at their respective nodes and 0 at other nodes. In this case, there are seven elements along the portion of the *x*-axis, where the function *u* is defined (i.e., the length of the rod).

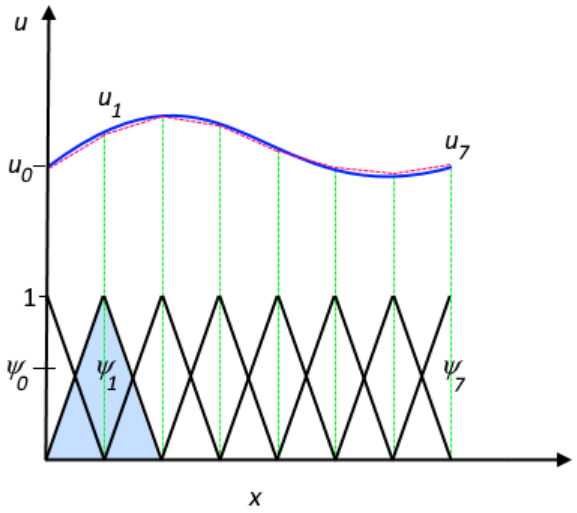

Figure 4: The function u (solid blue line) is approximated with uh (dashed red line), which is a linear combination of linear basis functions (ψi is represented by the solid black lines). The coefficients are denoted by u0 through u7 [4]

"One of the benefits of using the finite element method is that it offers great freedom in the selection of discretization, both in the elements that may be used to discretize space and the basic functions. In the figure above, for example, the elements are uniformly distributed over the *x*-axis, although this does not have to be the case. Smaller elements in a region where the gradient of *u* is large could also have been applied, as highlighted below."[4]

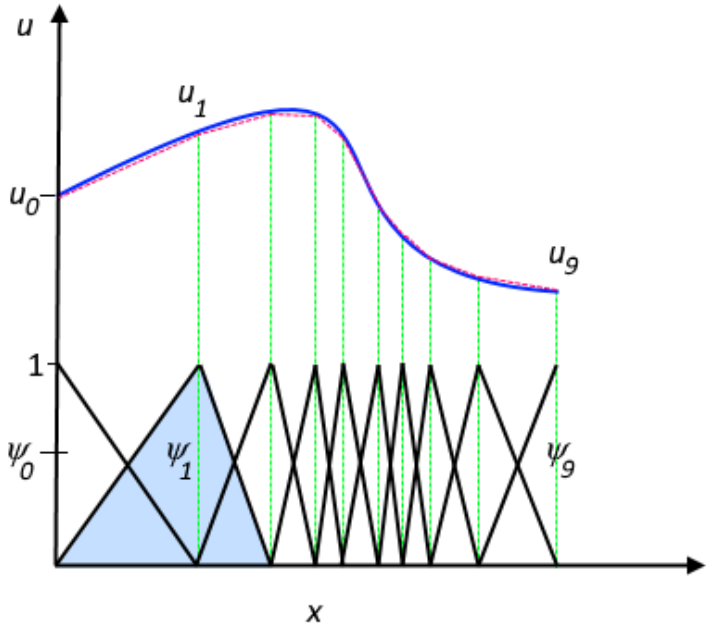

Figure 5: The function u (solid blue line) is approximated with uh (dashed red line), which is a linear combination of linear basis functions (ψi is represented by the solid black lines). The coefficients are denoted by u0 through u7.[4]

Both figures show that the selected linear basis functions include very limited support (nonzero only over a narrow interval) and overlap along the *x*-axis. Depending on the problem at hand, other functions may be chosen instead of linear functions.

Another benefit of the finite element method is that the theory is well developed. The reason for this is the close relationship between the numerical formulation and the weak formulation of the PDE problem. For instance, the theory provides useful error estimates, or *bounds* for the error, when the numerical model equations are solved on a computer.

Looking back at the history of FEM, the usefulness of the method was first recognized at the start of the 1940s by Richard Courant, a German American mathematician. While Courant recognized its application to a range of problems, it took several decades before the approach was applied generally in fields outside of structural mechanics, becoming what it is today.

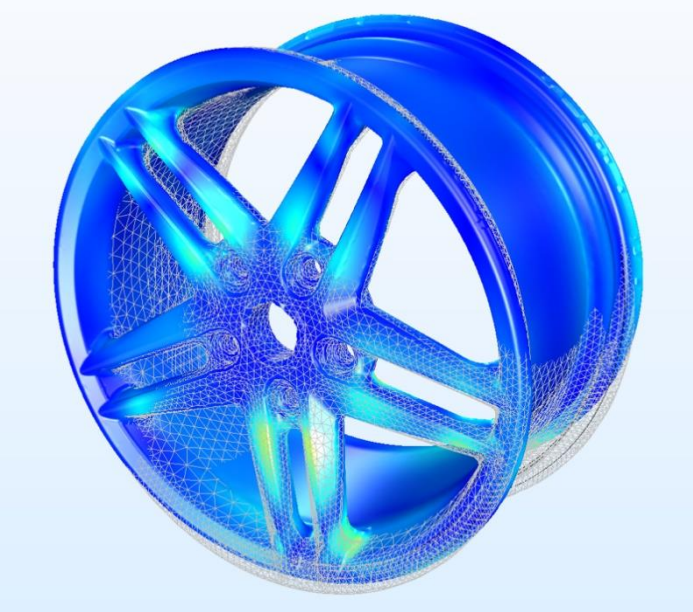

Figure 6: Finite element discretization, stresses, and deformations of a wheel rim in a structural analysis.[4]

2.2 Algebraic Equations, Ordinary Differential Equations, Partial Differential Equations, and the Laws of Physics

The laws of physics are often expressed in the language of mathematics. For example, conservation laws such as the law of conservation of energy, conservation of mass, and conservation of momentum can all be expressed as partial differential equations (PDEs). Constitutive relations may also be used to express these laws in terms of variables like temperature, density, velocity, electric potential, and other *dependent variables.* Differential equations include expressions that determine a small change in a dependent variable with respect to a change in an *independent variable* (x, y, z, t). This small change is also referred to as the derivative of the dependent variable with respect to the independent variable. Say there is a solid with time-varying temperature but negligible variations in space. In this case, the equation for conservation of internal (thermal)

energy may result in an equation for the change of temperature, with a very small change in time, due to a heat source *g*:

$$\rho C_p \frac{dT}{dt} = g(T, t) \tag{2.3}$$

Here, denotes the density and C_p denotes the heat capacity. Temperature, T, is the dependent variable and time, t, is the independent variable. The function may describe a heat source that varies with temperature and time. Eq. (2.3) states that if there is a change in temperature in time, then this must be balanced (or caused) by the heat source. The equation is a differential equation expressed in terms of the derivatives of one independent variable (t). Such differential equations are known as *ordinary differential equations* (ODEs).

In some situations, knowing the temperature at a time t_0, called an *initial condition*, allows for an analytical solution of Eq. (2.3) that is expressed as:

$$T = f(t) \tag{2.4}$$

The temperature in the solid is therefore expressed through an *algebraic equation* (2.4), where giving a value of time, t_1, returns the value of the temperature, T_1, at that time. Oftentimes, there are variations in time and space. The temperature in the solid at the positions closer to a heat source may, for instance, be slightly higher than elsewhere. Such variations further give rise to a heat flux between the different parts within the solid. In such cases, the conservation of energy can result in a heat transfer equation that expresses the changes in both time and spatial variables (x), such as:

$$\rho C_p \frac{\delta T}{\delta t} + \nabla \cdot \boldsymbol{q} = g(T, t, x) \tag{2.5}$$

As before, T is the dependent variable, while x (x = (x, y, z)) and t are the independent variables. The heat flux vector in the solid is denoted by q = (q_x, q_y, q_z) while the *divergence* of q describes the change in heat flux along the spatial coordinates. For a Cartesian coordinate system, the divergence of q is defined as:

$$\nabla \cdot \boldsymbol{q} = \frac{\partial q_x}{\partial x} + \frac{\partial q_y}{\partial y} + \frac{\partial q_z}{\partial z} \tag{2.6}$$

Eq. 2.6 thus states that if there is a change in net flux when changes are added in all directions so that the divergence (sum of the changes) of q is not zero, then this must be balanced (or caused) by a heat source and/or a change in temperature in time (accumulation of thermal energy).

The heat flux in a solid can be described by the constitutive relation for heat flux by conduction, also referred to as *Fourier's law*:

$$q = -k\nabla T \rightarrow q = \left(-k\frac{\partial T}{\partial x}, -k\frac{\partial T}{\partial y} - k\frac{\partial T}{\partial z}\right) \tag{2.7}$$

In the above equation, k denotes the thermal conductivity. Eq. 2.7 states that the heat flux is proportional to the gradient in temperature, with the thermal conductivity as proportionality constant. Eq. 2.7 in Eq. 2.6 gives the following differential equation:

$$\rho C_p \frac{\delta T}{\delta t} + \nabla \cdot (-k\nabla T) = g(T, t, x) \tag{2.8}$$

Here, the derivatives are expressed in terms of t, x, y, and z. When a differential equation is expressed in terms of the derivatives of more than one independent variable, it is referred to as a partial differential equation (PDE), since each derivative may represent a change in one direction out of several possible directions. Further note that

the derivatives in ODEs are expressed using d, while partial derivatives are expressed using the curlier ∂.

In addition to Eq. 2.8, the temperature at a time t_0 and temperature or heat flux at some position x_0 could be known as well. Such knowledge can be applied in the initial condition and boundary conditions for Eq. 2.8. In many situations, PDEs cannot be resolved with analytical methods to give the value of the dependent variables at different times and positions. It may, for example, be very difficult or impossible to obtain an analytic expression such as:

$$T = f(t, x) \tag{2.9}$$

Rather than solving PDEs analytically, an alternative option is to search for approximate *numerical solutions* to solve the numerical model equations. The finite element method is exactly this type of method – a numerical method for the solution of PDEs.

Like the thermal energy conservation referenced above, it is possible to derive the equations for the conservation of momentum and mass that form the basis for fluid dynamics. Further, the equations for electromagnetic fields and fluxes can be derived for space- and time-dependent problems, forming systems of PDEs.

2.3 The Finite Element Method from the Weak Formulation: Basis Functions and Test Functions

Assume that the temperature distribution in a heat sink is being studied, given by Eq. (2.8), but now at steady state, meaning that the time derivative of the temperature field is zero in Eq. (2.8). The domain equation for the model domain, Ω, is the following:

$$\nabla \cdot (-k\nabla T) = g(T,x) \quad in\ \Omega \tag{2.10}$$

Further, assume that the temperature along a boundary ($\partial\Omega_1$) is known, in addition to the expression for the heat flux normal to some other boundaries ($\partial\Omega_2$). On the remaining boundaries, the heat flux is zero in the outward direction ($\partial\Omega_3$). The boundary conditions at these boundaries then become:

$$T = T_0 \quad on \quad \delta\Omega_1 \tag{2.11}$$

$$(-k\nabla T) \cdot \boldsymbol{n} = h(T - T_{amb}) \ \ on \ \ \delta\Omega_2 \tag{2.12}$$

$$(-k\nabla T) \cdot \boldsymbol{n} = 0 \quad on \quad \delta\Omega_3 \tag{2.13}$$

where h denotes the heat transfer coefficient and T_{amb} denotes the ambient temperature. The outward unit normal vector to the boundary surface is denoted by **n**. Equations (2.10) to (2.13) describe the mathematical model for the heat sink, as shown below.

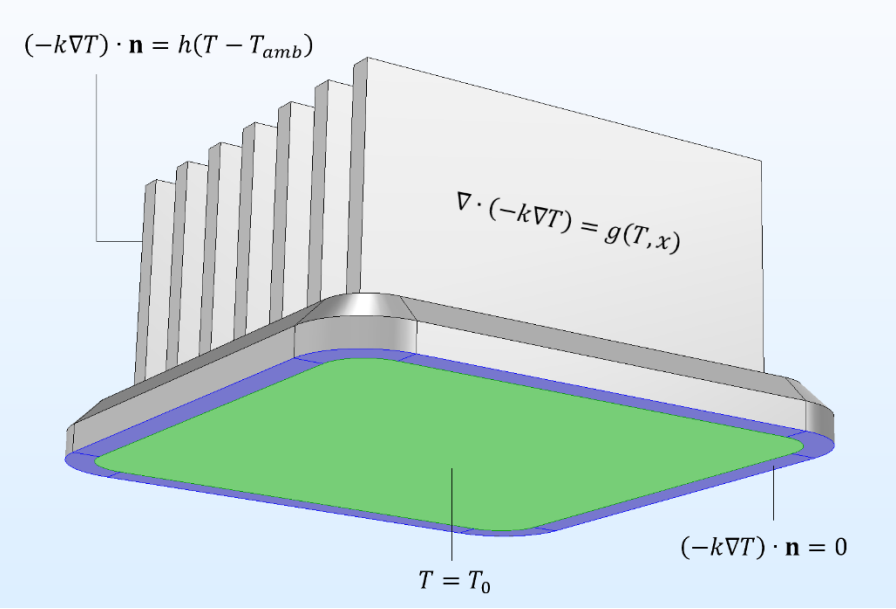

Figure 7: The domain equation and boundary conditions for a mathematical model of a heat sink[4]

The next step is to multiply both sides of Eq. (2.10) by a *test function* φ and integrate over the domain Ω:

$$\int_{\Omega} \nabla \cdot (-k\nabla T)\varphi dV = \int_{\Omega} g\varphi dV \tag{2.14}$$

The test function φ and the solution T are assumed to belong to Hilbert space. A Hilbert space is an infinite-dimensional *function space* with functions of specific properties. It can be viewed as a collection of functions with certain nice properties, such that these functions can be conveniently manipulated in the same way as ordinary vectors in a vector space. For example, you can form linear combinations of functions in this collection (the functions have a well-defined length referred to as *norm*) and you can measure the angle between the functions, just like Euclidean vectors.

Indeed, after applying the finite element method on these functions, they are simply converted to ordinary vectors. The finite element method is a systematic way to convert the functions in an infinite dimensional function space to first functions in a finite dimensional function space and then finally ordinary vectors (in a vector space) that are tractable with numerical methods.

The weak formulation is obtained by requiring (2.14) to hold for all test functions in the test function space instead of Eq. (2.10) for all points in Ω. A problem formulation based on Eq. (2.10) is thus sometimes referred to as the *pointwise formulation*. In the so-called *Galerkin method*, it is assumed that the solution T belongs to the same Hilbert space as the test functions. This is usually written as $\varphi \in H$ and $T \in H$, where H denotes the Hilbert space. Using Green's first identity (essentially integration by parts), the following equation can be derived from (2.14):

$$\int_{\Omega} k\nabla T \cdot \nabla\varphi dV + \int_{\delta\Omega} (-k\nabla T) \cdot \boldsymbol{n}\varphi dS = \int_{\Omega} \mathrm{g}\varphi dV \tag{2.15}$$

The weak formulation, or *variational formulation*, of Eq. (2.10) is obtained by requiring this equality to hold for *all* test functions in the Hilbert space. It is called "weak" because it relaxes the requirement (2.10), where all the terms of the PDE must be well defined in all points. The relations in (2.14) and (2.15) instead only require equality in an integral sense. For example, a discontinuity of a first derivative for the solution is perfectly allowed by the weak formulation since it does not hinder integration. It does, however, introduce a *distribution* for the second derivative that is not a function in the ordinary sense. As such, the requirement (2.10) does not make sense at the point of the discontinuity.

A distribution can sometimes be integrated, making (2.14) well defined. It is possible to show that the weak formulation, together with boundary conditions (2.11) through (2.13), is directly related to the solution from the pointwise formulation. And, for cases where the solution is *differentiable* enough (i.e., when second derivatives are well defined), these solutions are the same. The formulations are equivalent, since deriving (2.15) from (2.10) relies on Green's first identity, which only holds if T has continuous second derivatives.

This is the first step in the finite element formulation. With the weak formulation, it is possible to discretize the mathematical model equations to obtain the numerical model equations. The Galerkin method – one of the many possible finite element method formulations – can be used for discretization.

First, the discretization implies looking for an approximate solution to Eq. (2.15) in a finite-dimensional subspace to the Hilbert space H so that $T \approx T_h$. This implies that the approximate solution is expressed as a linear combination of a set of *basic functions* ψ_i that belong to the subspace:

$$T_h(x) = \sum_i T_i \psi_i(x) \tag{2.16}$$

The discretized version of Eq.(2.15) for every test function ψ_j therefore becomes:

$$\sum_i T_i \int_\Omega k\nabla\psi_i \cdot \nabla\psi_j dV + \sum_i \int_{\delta\Omega} (-kT_i\nabla\psi_i) \cdot n\psi_j dS = \int_\Omega g\left(\sum_i T_i\psi_i\right)\psi_i \tag{2.17}$$

The unknowns here are the coefficients T_i in the approximation of the function T(x). Eq. (2.17) then forms a system of equations of the same dimension as the finite-dimensional function space. If n number of test functions ψ_j are used so that j goes from 1 to n, a system of n number of equations is obtained according to (2.17). From Eq. (2.16), there are also n unknown coefficients (T_i).

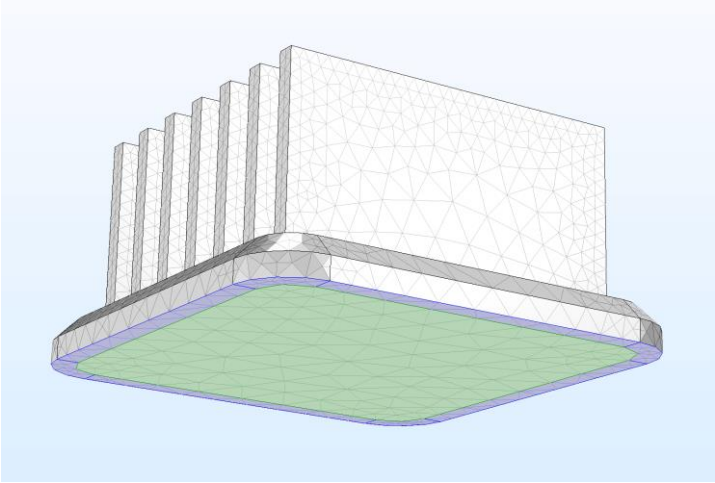

Figure 8: Finite element discretization of the heat sink model from the earlier figure [4]

Once the system is discretized and the boundary conditions are imposed, a system of equations is obtained according to the following expression:

$$AT_h = b \tag{2.18}$$

where T is the vector of unknowns, $T_h = \{T_1, .., T_i, \ldots, T_n\}$, and Ais an n x n matrix containing the coefficients of T_i in each equation j within its components A_{ji}. The right-hand side is a vector of the dimension 1 to n. A is the *system matrix*, often referred to as the (eliminated) *stiffness matrix*, harkening back to the finite element method's first application as well as its use in structural mechanics.

If the source function is nonlinear with respect to temperature or if the heat transfer coefficient depends on temperature, then the equation system is also nonlinear, and the vector b becomes a nonlinear function of the unknown coefficients T_i.

One of the benefits of the finite element method is its ability to select test and basic functions. It is possible to select test and basic functions that are supported over a very small geometrical region. This implies that the integrals in Eq. (2.17) are zero everywhere, except in very limited regions where the functions ψ_j and ψ_i overlap, as all of the above integrals include products of the functions or gradients of the functions i and j. The support of the test and basic functions is difficult to depict in 3D, but the 2D analogy can be visualized.

Assume that there is a 2D geometrical domain and that linear functions of x and y are selected, each with a value of 1 at a point i, but zero at other points k. The next step is to discretize the 2D domain using triangles and depict how two basic functions (test or shape functions) could appear for two neighbouring nodes i and j in a triangular mesh.

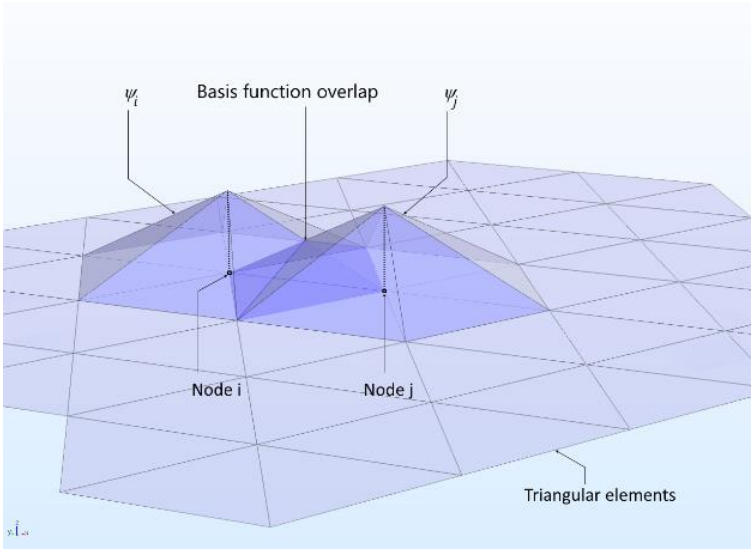

Figure 9: Tent-shaped linear basis functions that have a value of 1 at the corresponding node and zero on all other nodes. Two base functions that share an element have a basis function overlap [4]

Two neighbouring basis functions share two triangular elements. As such, there is some overlap between the two basic functions, as shown above. Further, note that if $i = j$, then there is a complete overlap between the functions. These contributions form the coefficients for the unknown vector T that correspond to the diagonal components of the system matrix A_{ij}.

Say the two basic functions are now a little further apart. These functions do not share elements, but they have one element vertex in common. As the figure below indicates, they do not overlap.

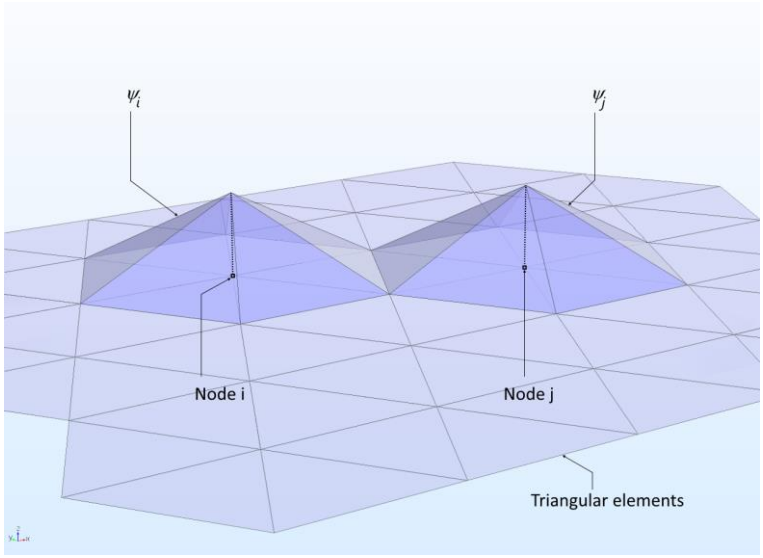

Figure 10: Two basis functions that share one element vertex but do not overlap in a 2D domain [4]

When the basic functions overlap, the integrals in Eq. (2.17) have a nonzero value and the contributions to the system matrix are nonzero. When there is no overlap, the integrals are zero and the contribution to the system matrix is therefore zero as well.

This means that each equation in the system of equations for (2.17) for the nodes 1 to n only gets a few nonzero terms from neighbouring nodes that share the same element. The system matrix A in Eq. (2.18) becomes sparse, with nonzero terms only for the matrix components that correspond to overlapping *ij*:*s*. The solution of the system of algebraic equations gives an approximation of the solution to the PDE. The denser the mesh, the closer the approximate solution gets to the actual solution.

2.4 Time-Dependent Problems

Thermal energy balance in the heat sink can be further defined for time-dependent cases. Discretized weak formulation for every test function ψ_j, using Galerkin, is

$$\rho C_p \frac{\partial T_i}{\partial t} \sum_i \int_\Omega \psi_i \psi_j dV + \sum_i T_i \int_\Omega k \nabla \psi_i \cdot \nabla \psi_j dV + \sum_i \int_{\partial\Omega} (-k T_i \nabla \psi_i \cdot \mathbf{n}) \psi_j dS = \int_\Omega g \left(\sum_i T_i \psi_i \right) \psi_j dV \qquad (2.19)$$

Coefficients T_i: time-dependent functions while basis and test functions depend on spatial coordinates. In addition, time derivative is not discretized in time domain.

Use FEM for time domain is computationally expensive so an alternative can be the introduction of an independent discretization of time domain using the method of lines (i.e. technique to solve PDEs in which all but one dimension is discretized).
If we state

$$\frac{\delta T_i}{\delta t} \approx \frac{T_{i,t+\Delta t} - T_{i,t}}{\Delta t} \tag{2.20}$$

we can reformulate the Eq.(19) in two different form approximation.
The first one is when the unknow coefficients $T_{i,t}$ are expressed in terms of $t + \Delta t$, the second one when are expressed in terms of the solution at *t*.
For the former we note that if the problem is linear/non-linear a linear/non-linear system of equations needs to be solved for each time step. The time-marching scheme is referred to as an implicit method, as the solution at $t + \Delta t$ is implicitly given by the equation. While, the latter implies once the solution $T_{i,t}$ is known at a given time then corresponding equation explicitly gives the solution at $t + \Delta t(T_{i,t+\Delta t})$ (i.e., for an explicit time-marching scheme there is no need to solve an eq. system at each time step).
Even the last method can be better there is a drawbacks regards the time-marching schemes, in fact, they come with a stability time-stepping restriction.

In practice, in modern time-stepping the switch between explicit and implicit is automatically.

2.5 Different Elements

Let's now analyse what are the ways of defining the basic functions related to Galerkin's method. First of all, let's analyse the linear functions and in figure X we will show only the most common ways.

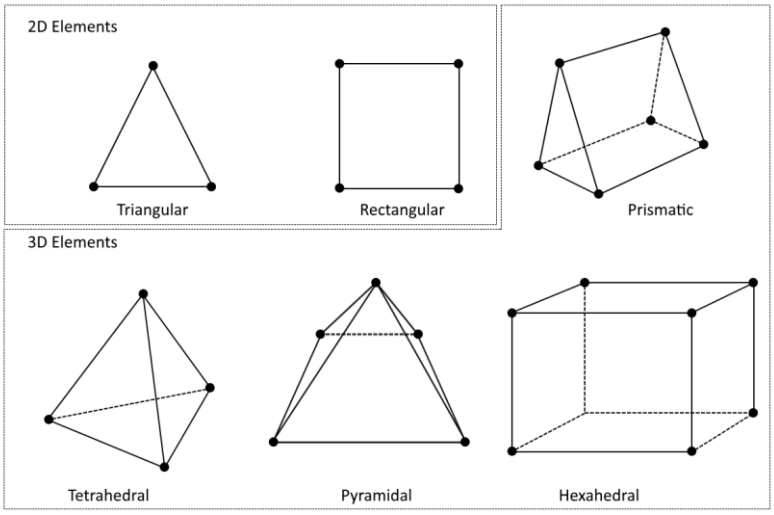

Figure 11: Node placement and geometry for 2D and 3D linear elements [4]

We start with the analysis of 2D elements, in which rectangular elements are often applied to mesh for the boundary layer in CFD and heat transfer modelling. Their 3D analogue is the hexahedral element. In the transition from hexahedral boundary layer elements to tetrahedral elements, pyramidal elements are usually positioned above boundary layer elements.

Now, let's go and analyse the quadratic elements. In this case, edges and surfaces facing a domain border are often curved, while edges and surfaces facing the inner portion of the domain are lines or flat surfaces.

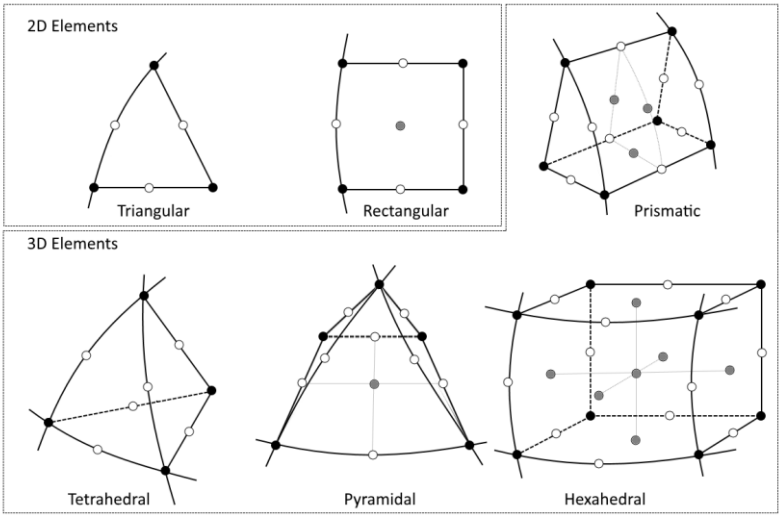

Figure 12: Second-order elements. If the gray nodes are removed, we get the corresponding serendipity elements. The black, white, and gray nodes are all present in the Lagrangian elements [4]

2.6 Error estimation

When talking about FEM a fundamental element to consider is the estimation of the error, in fact, when the estimated tolerance value is reached convergence occurs. The FEM method gives an approximate solution to the mathematical model, and, for that reason, the difference between the solution to the numerical equations and the exact solution to the mathematical model equations has an error, that is: $e = u - u_h$.

To establish the convergence order of the FEM method we estimate *a priori* the error. For instance, if the problem is well posed and the numerical method converges, the norm of the error decreases with the typical element size h according to $O(h^{\alpha})$, where α denotes the order of convergence. This simply indicates how fast the norm of the error is expected to decrease as the mesh is made denser.

However, it must be said that the *a priori* estimation can be found only for simple problems.

The other way to estimate the error is obviously the *a posteriori* ones. That technique uses the approximate solution, in combination with other approximations to related problems.

2.7 Mesh convergence

We now present a very simple method to compare approximate solutions obtained for different meshes, i.e., mesh convergence.

If we go to calculate a solution in a very fine mesh we will surely reduce the error to a value close to zero, for this reason we can assume the solution as actual. With this assumption we can now define the error for larger meshes as

$$e = u_{h1} - u_h \tag{1}$$

where u_h is the solution obtained from the fine mesh and u_{h1} from the coarser mesh.

If we now consider a body of the type in figure 13 and calculate its equations for various mesh types and element sizes, we can verify this.

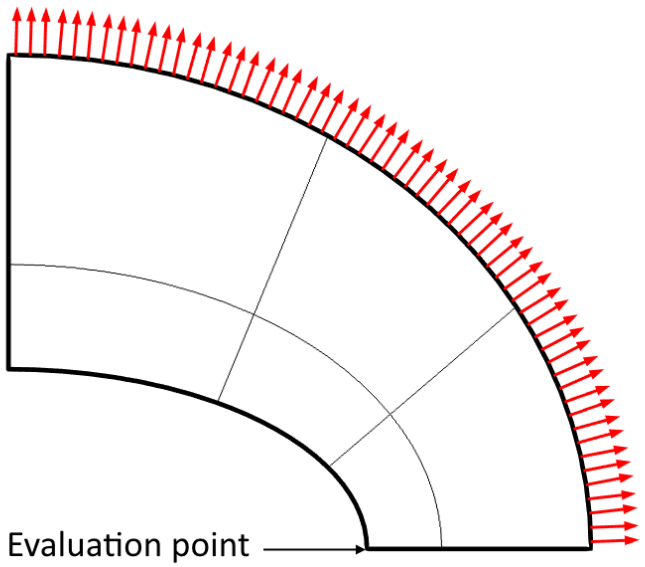

Figure 13: Benchmark model of an elliptic membrane. The load is applied at the outer edge while symmetry is assumed at the edges positioned along the x- and y-axis (roller support) [4]

For example, Figure 14 represents the rectangular Lagrange elements used for the basic quadratic functions

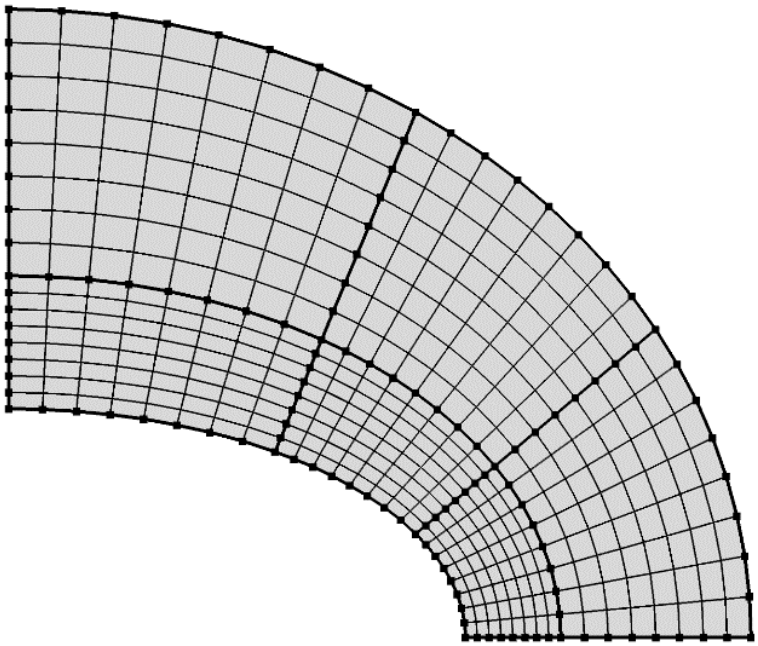

Figure 14: Rectangular elements used for the quadratic base functions [4]

The figure 15 below shows that the relative error decreases with decreasing element size (h) for all elements. In this case, the convergence curve becomes steeper as the order of the basic functions (elements order) becomes higher. Note, however, that the number of unknowns in the numerical model increases with the element order for a given element size. This means that when we increase the order of the elements, we pay the price for higher accuracy in the form of increased computational time. An alternative to using higher-order elements is therefore to implement a finer mesh for the lower-order elements.

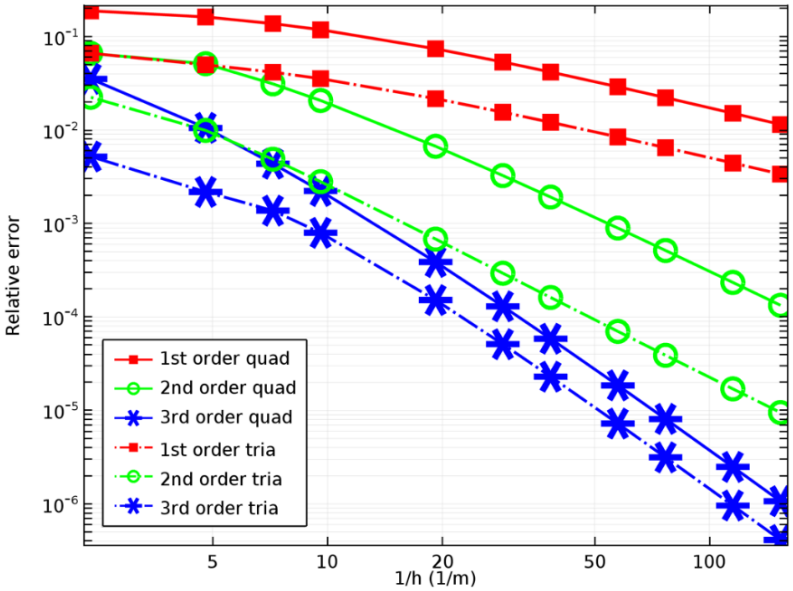

Figure 15: Relative error in σx at the evaluation point in the previous figure for different elements and element sizes (element size = h). Quad refers to rectangular elements, which can be linear or with quadratic basis functions [4]

Chapter 3

Materials

3.1 Introduction

In this chapter we will discuss the materials that are used in electrical machines. Starting from general considerations we will then go on to deduce two fundamental concepts for our study, the B-H curve and therefore hysteresis. Finally, we summarize the various materials used in the model parts.

3.2 Magnetic Materials

The magnetic materials are divided into two main categories:

1. Soft magnetic materials: diamagnetic, paramagnetic, and ferromagnetic materials

2. Hard magnetic materials: permanent magnets

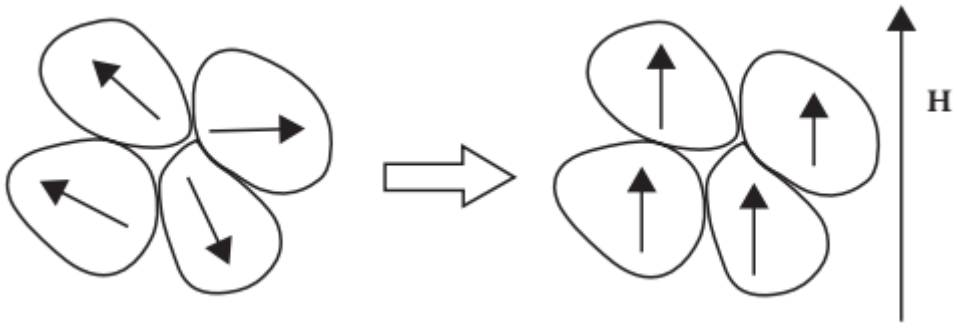

Figure 16: Magnetic domains before and after alignment with the external magnetic field [5]

Analysing from a macroscopic point of view these materials we can see in Figure 16a how they initially possess magnetic fields directed in arbitrary directions.
Only later, when an external H magnetic field is applied, the magnetic fields of the domains tens to align with it. We also note from Figure 16b that when the magnetic

field is removed, the domains maintain their alignment.
The accumulation of this effect over time forms the residual flux density of the permanent magnet (Br).
The difference between Soft and Hard magnetic is whether it is easy to change the initial alignment. In the former it is sufficient to apply a weak external magnetic field in the opposite direction to the internal field to eliminate the residual flux density; while in the latter the magnetic field H must be very strong.
Therefore, considering an analytical point of view, we must define the relative permeability as

$$\mu_r = \frac{\mu}{\mu_0} \tag{3.1}$$

Where μ is the actual permeability of the material and $\mu_0 = 4\pi \times 10^{-7} \frac{H}{m}$ is the permeability of air (actually free space). Therefore, μ_r of air is equal to 1.
We can now calculate the total magnetic induction B_{tot} as

$$B_{tot} = B_0 + B_r = \mu_0 H + \mu_0 M = \mu_0 (H + M) \tag{3.2}$$

where B_0 is the external induction and B_r the residual one (i.e. induction due material type).

3.3 Soft Magnetic Materials

3.3.1 Introduction

The soft magnetic materials can be classified into three categories: diamagnetic, paramagnetic and ferromagnetic materials. Paramagnetic and Ferromagnetic have atoms with permanent magnetic moments and the Diamagnetic, made of atoms that do not have permanent magnetic moments.

So, the classification depends on the magnetic dipole moment of atoms of the material and on the interactions among the atoms. When the different magnetic materials are placed in a uniform magnetic field, the field lines changes. Since soft magnetic materials can be demagnetized at low magnetic field, coercivity H_c is low. As they can be easily magnetized, permeability is high.

3.3.2 Diamagnetic

The permeability of diamagnetic materials is slightly less than, or equals, to the free space permeability (slightly less than 1). Since $\mu_r < 1$ most of the flow passes through the air and not through the material, the air has a higher permeability. This behaviour generates small persistent currents, due to the reorganization of the electron orbits, which are opposed to the external magnetic field. This causes a force that tends to repel the diamagnetic body from the source that generates the field. However, since the permeability is very close to one, this effect is very small and difficult to measure. These materials have a very weak and negative susceptibility to external magnetic fields and does not retain the magnetic properties when the external field is removed. Notable materials in this group are mercury, gold, silver, and copper. The field line distribution of a diamagnetic material placed in a uniform magnetic field is shown in Figure 17.

Figure 17: Field lines distribution of diamagnetic materials placed in a uniform magnetic field H [6]

3.3.3 Paramagnetic

The relative permeability of paramagnetic materials is slightly more than the free space permeability (slightly more than 1). "Therefore, as with the diamagnetic materials, we can consider the materials as having $\mu_r = 1$ for most practical purposes. In general, the effect due to the paramagnet- ism is negligible."[5] Notable material in this group is

aluminium. The field line distribution of a diamagnetic material placed in a uniform magnetic field is shown in Figure 18.

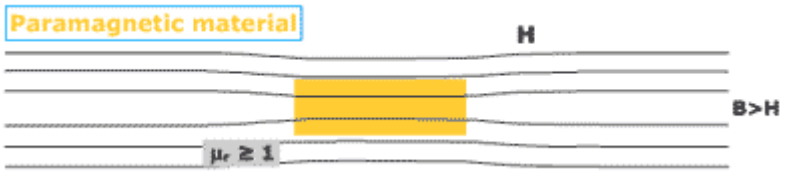

Figure 18: Field lines distribution of paramagnetic materials placed in a uniform magnetic field H [6]

3.3.4 Ferromagnetic materials

The relative permeability of ferromagnetic materials is much greater than one, so, much greater than the free space permeability. This feature allows it to have a large and positive susceptibility to an external magnetic field. As we can see in Figure 19 they exhibit a strong attraction to magnetic fields; in addition, they are able to retain their magnetic properties after the external field has been removed.

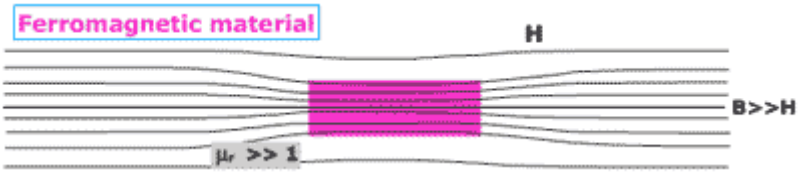

Figure 19: Field lines distribution of ferromagnetic materials placed in a uniform magnetic field H [6]

"If we subject a ferromagnetic material to the influence of a magnetic field, we obtain the situation shown in Figure 20. With $\mu_r \gg 1$, the magnetic flux is strongly attracted by the ferromagnetic material since it is a highly permeable material. In this case, the ferromagnetic material is physically attracted."[5]

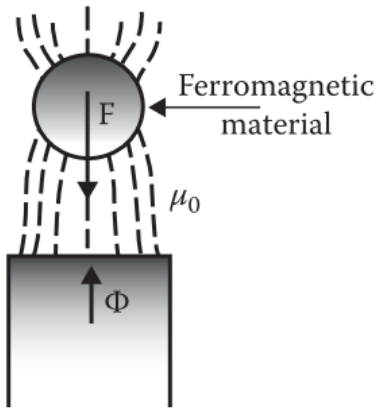

Figure 20: Ferromagnetic material in a magnetic field. Flux lines pass through the mate- rial and the material is attracted to the source of the field [5]

"Ferromagnetic materials have some unpaired electrons, so their atoms have a net magnetic moment. They get their strong magnetic properties due to the presence of magnetic domains within which the magnetic moments of all its atoms (10^{19}) are aligned parallel to each other." [7] Notable materials in this group are iron, nickel and cobalt, and their alloys such as AlNiCo.

An important factor to consider when dealing with ferromagnetic materials is temperature. These materials, in fact, if placed in a hot environment changes its magnetic behaviour become as paramagnetic ones. This change happens when the temperature passes over a critical value, called "Curie temperature". This is because the magnetic domains will organize themselves randomly after theirs atoms are being heated.

We have already seen that how permeability plays a fundamental role; in this kind of material permeability as well as being great is also dependent from the magnitude of the magnetic field intensity $|\mathbf{H}|$; this phenomenon is called non-linearity.

Taking into account the Figure 21 we can see a magnetic circuit made of a high permeability materials with a ferromagnetic sample (black ones) inserted into it.

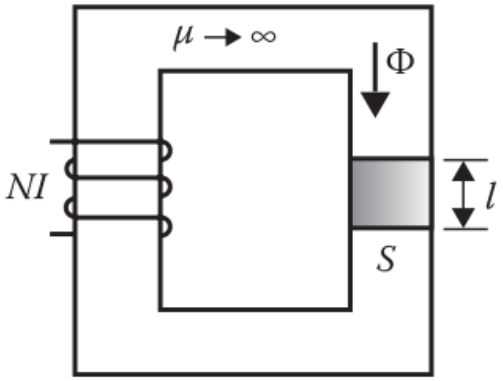

Figure 21: Magnetic circuit used to obtain the magnetic characteristics of a ferromagnetic sample [5]

Knowing that $H = NI/l$ and $B = \Phi/S$ we can compute both the current I applied to a coil and the flux Φ passing through the material.

From the formulas we notice that H and B are directly proportional to I and Φ and so we can plot the curve shown in figure 22.

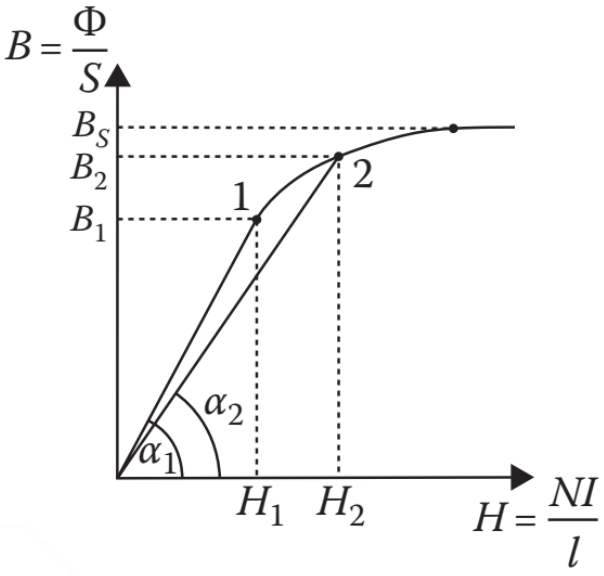

Figure 22: A typical B(H) for a ferromagnetic material [5]

"We point out that the characteristic curve of a magnetic material is always the $B(H)$ curve since the $\Phi(I)$ curve contains, implicitly, the dimensions of surface, length, and the number of turns."[5]

The B-H curve is the curve characteristic of the magnetic properties of a material or element or alloy. It tells you how the material responds to an external magnetic field, and is a critical piece of information when designing magnetic circuits. [8]

"The slope of the B-H curve at some location on its curve is its incremental permeability at that location. However, sometimes the permeability is measured from the origin to the location of interest, and that slope is called its apparent permeability, μ." [8]

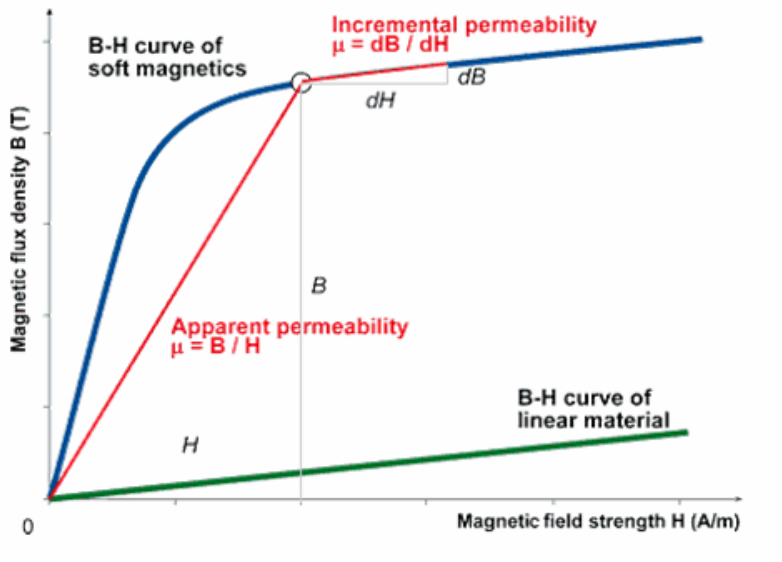

Figure 23: Permeability curve [8]

For non-magnetic materials that do not saturate, the curve has a fixed slope approximately equal to μ_0, for diamagnetic materials have a slightly smaller slope and for paramagnetic materials have a slightly greater slope.

For more detailed information about the BH curve application on COMSOL please refer to Appendix C.

3.3.5 Hysteresis

We have seen that the magnetization behaviour of the ferromagnetic materials belong to the B-H curve. When we have a B-H curve magnetization we experience also the

Hysteresis, that is a situation where the magnetic flux lags the increases or decreases in magnetizing force. The hysteresis comes into play when the material has been magnetized. The B within the material does not go back to what it was before, but is dependent on the history of its magnetization.[9]

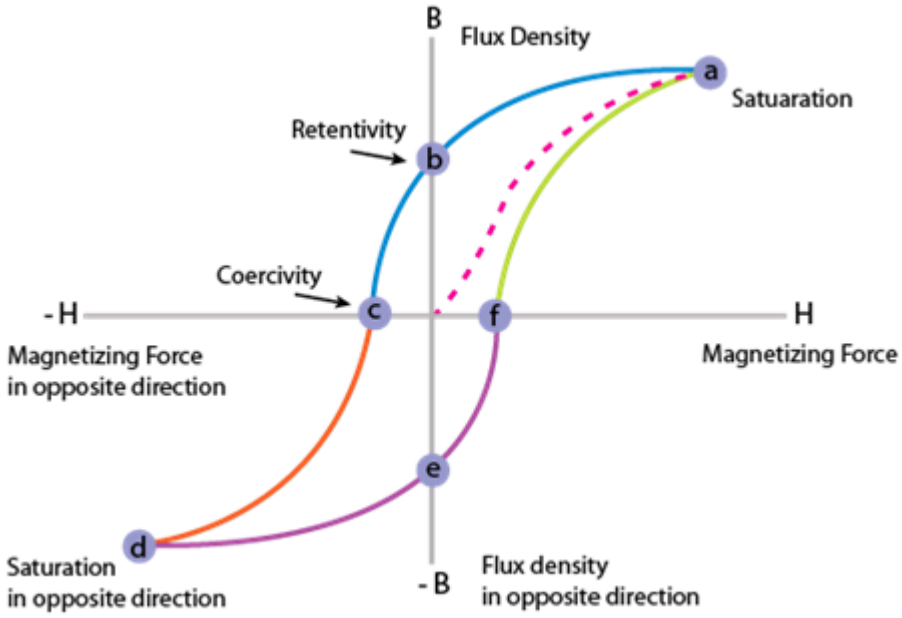

Figure 24: Hysteresis Loop curve [8]

Analysing the Figure 24 we can explain the Hysteresis Loop. Starting with unmagnetized situation we are in 0 (both for H and B) on the curve. Let's go now to increase the magnetization current, this will lead to an increase of H and B and then we will get to the point (a) where all the magnetic domains are aligned and still increasing the current will lead to a very limited increase of the magnetic flux. We are in the condition of magnetic saturation. Going now to remove H the curve moves from (a) to point (b). At this particular point, called Retentivity, we notice that the value of the magnetic flux (B) is not zero even if the magnetizing force is. Going now to invert the applied magnetics force (i.e. applying negative values of H) we go towards point (c) where we have the null flux. This is called the point of coercivity on the curve: the reversed magnetising force has flipped enough of the domains so that the net flux within the material is zero. The force required to remove the residual magnetism from the material, is called the coercive force or coercivity of the material. Continuing to negatively increase H we

arrive in a situation analogous to (a), i.e. of magnetic saturation; the only difference is the direction of magnetization, we are now at point (d).

Finally, by increasing H again (in positive value) we arrive at point (e) where we have a null H but a $B \neq 0$; this happens because also for "the negative part" we have a residual flux ($-B_r$). Increasing H back in the positive direction will return B to zero. Notice that the curve did not return to the origin of the graph because some force is required to remove the residual magnetism. The curve will take a different path from point (f) back to the saturation point where it completes the loop. [7]

As we already have seen the materials are classified in Hard (explained in next paragraph) and Soft. The first one has large hysteresis loop (Fig. 25a) while the latter have smallest one (Fig. 25b).

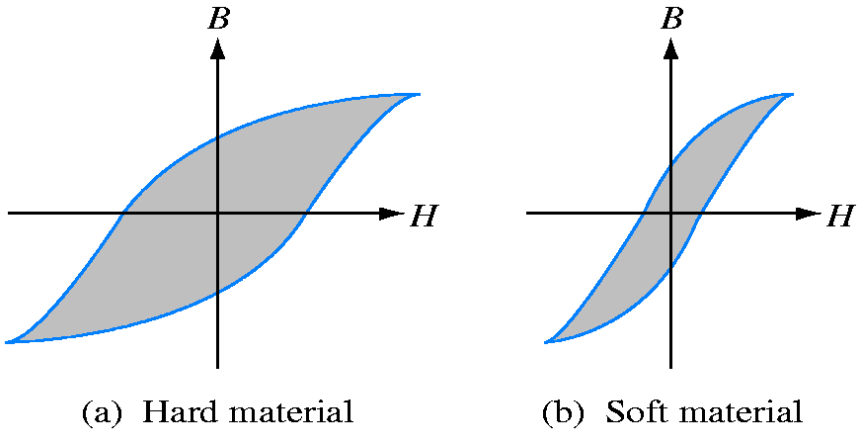

Figure 25: Comparison between hysteresis loop of a hard material (a) and of a soft material (b) [7]

3.4 Hard Magnetic Materials

3.4.1 Introduction

The hard-ferromagnetic materials are hard to magnetize and that happen only when high magnetic field is applied. In other words, this type of ferromagnetic materials is difficult to magnetize, but once magnetized, it is difficult to demagnetize. That materials are suitable for applications such as permanent magnets and magnetic recording media. Since large magnetic field is required to demagnetize, their coercivity H_c is usually high, but coercivity is highly sensitive to the microstructure.
The most popular permanent magnet materials are: Ferrite, AlNiCo, SmCo and NdFeB.[10]

3.4.2 Permanent Magnets

"The basis for the evaluation of a PM is the portion of its hysteresis loop located in the upper left-hand quadrant, called the demagnetization curve (Fig. 26)."

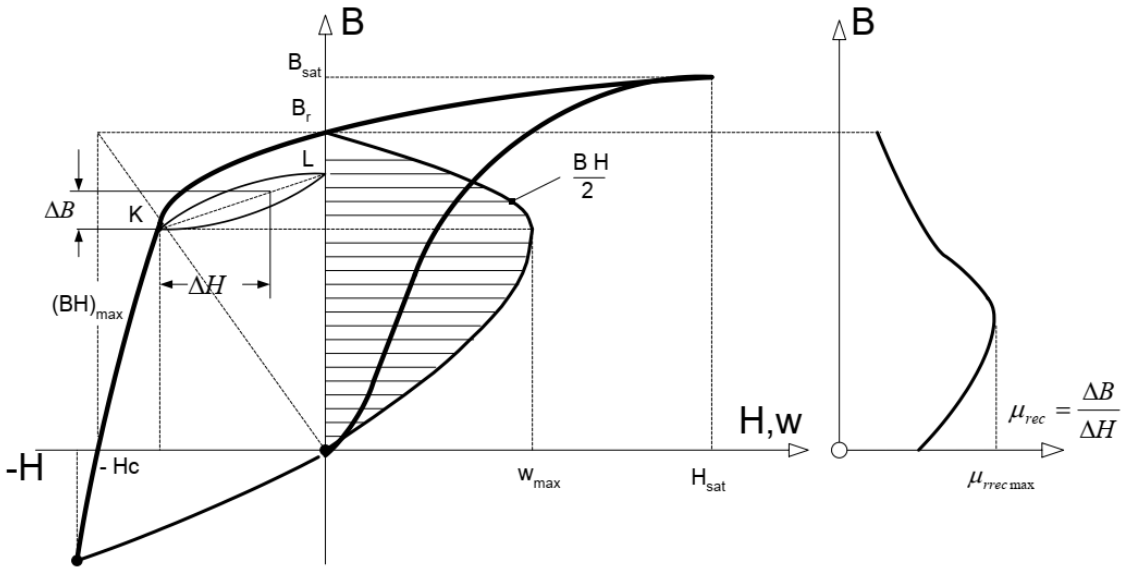

Figure 26: Demagnetization curve, recoil loop, energy of a PM, and recoil magnetic [11]

"If a reverse magnetic field intensity is applied to a previously magnetized, say, toroidal specimen, the magnetic flux density drops down to the magnitude determined by the

point K. When the reverse magnetic flux density is removed, the flux density returns to the point L according to a minor hysteresis loop. Thus, the application of a reverse field has reduced the remanence, or remanent magnetism. Reapplying a magnetic field intensity will again reduce the flux density, completing the minor hysteresis loop by returning the core to approximately the same value of flux density at the point K as before. The minor hysteresis loop may usually be replaced with little error by a straight line called the recoil line. This line has a slope called the recoil permeability μrec. As long as the negative value of applied magnetic field intensity does not exceed the maximum value corresponding to the point K, the PM may be regarded as being reasonably permanent. If, however, a greater negative field intensity H is applied, the magnetic flux density will be reduced to a value lower than that at point K. On the removal of H, a new and lower recoil line will be established." [12]
For completeness of information also the soft ferromagnetic materials also possess hysteresis curves, but the area described by the loop is relatively small.

3.4.3 Magnetic flux density in the Air Gap

The air gap is a necessary element in a dynamic machine (i.e. if you don't take it the relative movement could not exist) and has some interesting features to mention. First of all, since air is a magnetically non-conductive material, it increases the reluctance of the magnetic circuit, thus increasing the amount of current we could put in a coil before saturating it.

One of the main reasons for an Air Gap is to increase the reluctance of the magnetic circuit. The amount of air or other non-magnetic material such as a fibre plate or fibre board increases the reluctance of the circuit, thus increasing the amount of current we could put in a coil before reaching saturation. The air gap also, by creating a disconnection, creates magnetic fringes (i.e. magnetic fluxes that expand outside the circuit break); the latter can be overlooked with small air gaps (i.e. as in our case). However, with a larger air gap we might have to take that change in area into consideration when we start doing flux density calculations.

Analysing the Air gap in analytical point of view we must compute the Ampere's law over a circuit composed by a rectangular cross section consisting of a PM, two mild-steel yokes and an air gap. Make some calculus and considering the fringing flux in the air gap neglected, and we can find the magnetic flux intensity as

$$B_g = \mu_0 H_h = \sqrt{\frac{\mu_0}{\sigma_{lM}} k_{sat}^{-1} \frac{V_M}{V_g} B_M H_M} \tag{3.3}$$

3.4.4 Temperature effect

In the paragraph above about soft magnetic materials we have seen how those of ferromagnetic type are susceptible to temperature, since permanent magnets made from hard ferromagnetic materials will also be susceptible to temperature. It is therefore crucial to take this into account when designing magnetic circuits where it is necessary to obtain a high degree of temperature stability or where high maximum temperatures are likely to be reached in operation.

Demagnetization curves are sensitive to the temperature. Both B_r and H_c decreases as the magnet temperature increase, as we can see in the formulas.

$$B_r = B_{r_{20}}[1 + \frac{\alpha_B}{100}(\vartheta_{PM} - 20)] \tag{3.4}$$

$$H_c = H_{c_{20}}[1 + \frac{\alpha_H}{100}(\vartheta_{PM} - 20)] \tag{3.5}$$

where ϑ_{PM} is the temperature of the PM, $B_{r_{20}}$ and $H_{c_{20}}$ are the remanent magnetic flux density and coercive force at 20°C, respectively, and $\alpha_B < 0$ and $\alpha_H < 0$ are temperature coefficients for B_r and H_c in %/°C, respectively.

In the figure 27 we can see more clearly that dependence, here we see how the curves

trend is, more or less, like each other but with different values of remanence and coercivity..

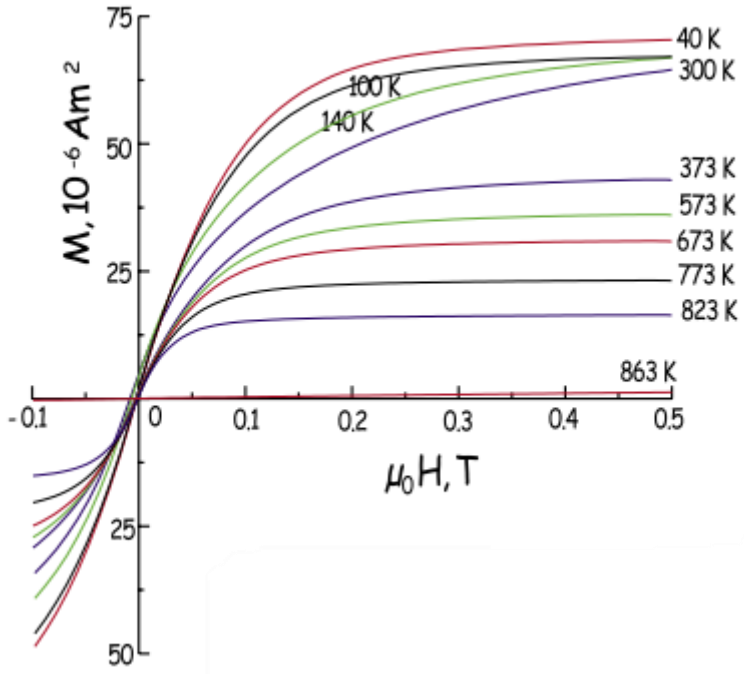

Figure 27: Descending branches of hysteresis loops determined at various temperatures [13]

"To minimise the effect of temperature on the field produced by a permanent magnet, it is advisable to operate above the 'knee' in the demagnetisation curves" [7] [13]

3.5 Characteristics comparison of Soft and Hard magnetic materials

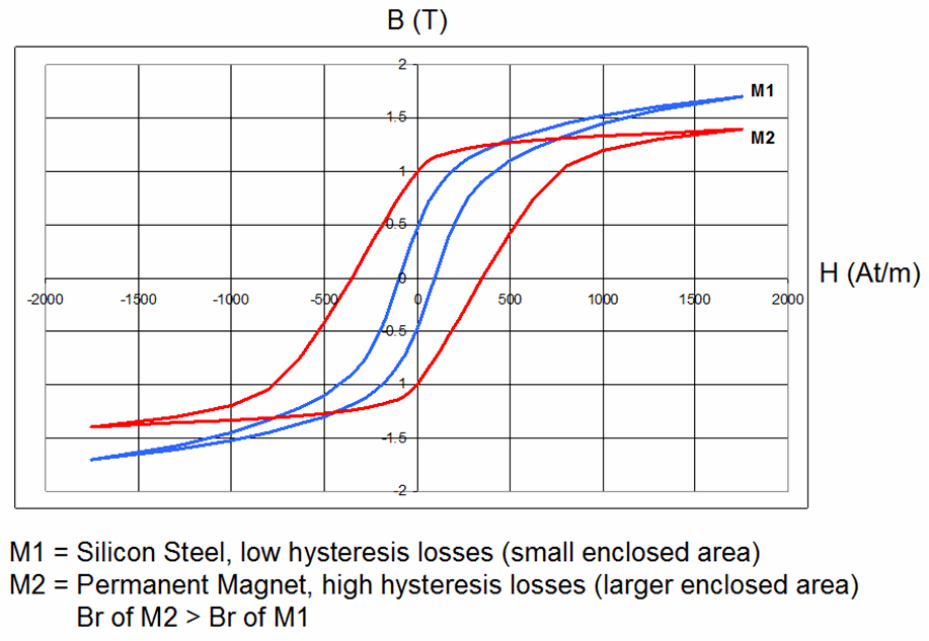

Figure 28: BH curve comparison on Soft and Hard magnetic materials [8]

Analysing Figure 28 we can see clearly what are the differences between the soft and hard magnetic materials. We have resumed the mainly characteristic below:

a) Soft magnetic material

1. "A material with a very low B_r and H_c
2. It does not retain a strong magnetic field (does not make a good permanent magnet), and is easy to demagnetize
3. The area enclosed by the B-H curve is small, so it has low hysteresis losses or core losses
4. This material is desired for use in transformers, motors and electromagnets where the magnetic field is always changing.

5. Electrical steels, which contain about 1-2% Si, is a soft magnetic material.

b) Hard magnetic material

1. A material with a very high Br and Hc
2. It retains a strong magnetic field (makes a good permanent magnet), and is difficult to demagnetize
3. The area enclosed by the B-H curve is large, so it has high hysteresis losses or core losses
4. This material is desired for use in permanent magnets.
5. Alloys such as AlNiCo and NdFeB are hard magnetic materials." [8]

3.6 Jiles-Atherton Model

3.5.1 Introduction

The Jiles-Atherton model is a set of mathematical equation that simulate the magnetization curve and, therefore, is used to fit the magnetic hysteresis curve.

This model, based on the concept of magnetization, is considered a physical model of magnetic hysteresis. The Jiles-Atherton model has differentiated itself from the others thanks to its simplicity of implementation and calculation. In fact, it is composed of an ordinary first degree differential equation composed of only five parameters, the determination of the latter, moreover, is possible through a single cycle of hysteresis which runs far enough into saturation. On the other hand, we can find drawbacks. Indeed, the determination of the parameters is feasible in a cycle, but the process identification is difficult. Moreover, being a simple model, near the loop tips we experience an unphysical behaviour. Finally, we have unsymmetrical and/or not closed

loops if saturation is not reached.
Especially the last drawback is an obstacle for the use of the pure JA model in electromagnetic field computations. [14]

"The main property of the JA hysteresis model is the decomposition of the magnetization M into its reversible component M_{rev}, which corresponds to domain wall bending during the magnetization process, and its irreversible component M_{irr}, which corresponds to domain wall displacement against the pinning effect. [15]
The relationships between these two components and the an hysteretic magnetization Man are derived from physical considerations of the magnetization process." [14]
From an analytically point of view the equations are

$$\frac{dM_{irr}}{dH} = \frac{M_{an} - M_{irr}}{k\delta - \alpha(M_{an} - M_{irr})} \tag{3.6}$$

$$M_{rev} = c(M_{an} - M_{irr}) \tag{3.7}$$

$$M_{an}(H) = M_S \left[\coth\left(\frac{H + \alpha M}{\alpha}\right) - \frac{\alpha}{H + \alpha M}\right] \tag{3.8}$$

a, α, c, k and the saturation magnetization M_s are the five model parameters which have to be determined from measured hysteresis characteristics; δ is a directional parameter and takes the value $\pm 1 \; for \; dH/dt \gtrless 0$

As already said, the determination of parameters is difficult, for this reason and since JA's properties are already included in COMSOL, we prefer not to spend time on them. For a better understanding we refer you to the papers of (Lederer et al. 1999) and (Jiles and Atherton 1984).

3.7 Conductors

3.6.1 Introduction

"Armature windings of electric motors are made of solid copper conductor wires with round or rectangular cross sections. When the cost or mass of the motor are paramount, e.g., long armature LSMs for transportation systems, magnetically levitated vehicles, hand tools, etc., aluminium conductor wires can be more suitable."[5]

3.6.2 Magnet Wire

"The magnetic wire or winding wire is an insulated copper or aluminium conductor typically used to wind electromagnetic devices such as machines and transformers. The American Wire Gauge is the standard used to represent the subsequent wire diameters." [12]

3.6.3 Copper

Copper has the highest conductivity of any non-precious metal. This combined with its high ductility, medium strength, ease of joining and good resistance to corrosion, makes copper the first choice as a conductor for electrical applications. High conductivity copper is the most common form of the metal and it is widely available with consistent high quality. It is the first choice for the manufacture of bulk conductors such as cables, busbars, transformer windings and motor stators and rotors. However, for other electrical applications, such as connector parts, commutators and catenary wires, the mechanical properties may need to be enhanced by the addition of appropriate alloying elements. The ease with which copper can form alloys with other elements results in the availability of a very wide range of materials suitable for all electrical applications.

3.6.5 Resistivity and conductivity

Electric conductivity σ of materials used for windings of electrical machines is given in Table 3.1.

Electric temperature coefficient at 20◦C 1/K or 1/◦C	Material	Electric resistivity ×10-6 Ωm	Electric conductivity ×106 S/m
Aluminium	0.0278	36	+0:00390
Brass (58% Cu)	0.059	17	+0:00150
Brass (63% Cu)	0.071	14	+0:00150
Carbon	40	0.025	-0:00030
Cast iron	1	1	|
Constantan	0.48	2.08	-0:00003
Copper	0.0172	58	+0:00380
Gold	0.0222	45	|
Graphite	8.00	0.125	-0:00020
Iron (pure)	0.10	10	|
Mercury	0.941	1.063	+0:00090
Mild steel	0.13	7.7	+0:00660
Nickel	0.087	11.5	+0:00400
Platinum	0.111	9	+0:00390
Silver	0.016	62.5	+0:00377
Zinc	0.061	16.5	+0:00370

Table 3.1: Electric resistivity, conductivity, and temperature coefficient at 20◦C [12]

"The variation of resistance R, electric resistivity ρ and electric conductivity σ with temperature in temperature range from 0°C to 150°C is expressed by the following equations:"[12]

$$R(\vartheta)R_{20}[1 + \alpha_{20}(\theta - 20)] \tag{3.9}$$

$$\rho(\vartheta) = \rho_{20}[1 + \alpha_{20}(\theta - 20)] \tag{3.10}$$

$$\sigma(\vartheta) = \frac{\sigma_{20}}{1 + \alpha_{20}(\theta - 20)} \tag{3.11}$$

"where $R_{20}, \rho_{20}, \sigma_{20}, \alpha_{20}$ are the resistance, resistivity, conductivity, and temperature coefficient at 20◦C, respectively, and ϑ is the given temperature. For copper wires, α =

0.00393 1/°C, and for aluminium wires α = 0.00403 1/°C. For ϑ > 150°C, additional electric temperature coefficient β20 must be introduced, e.g., for resistance" [12]

$$R(\vartheta) = R_{20}[1 + \alpha_{20}(\vartheta - 20) + \beta_{20}(\vartheta - 20)^2] \tag{3.12}$$

"At temperatures higher than room temperature (up to 1000°C), the resistivity of copper, aluminium, and brass changes more or less linearly with temperature, while the resistivity of steels abruptly increases (Fig. 29)." [12]

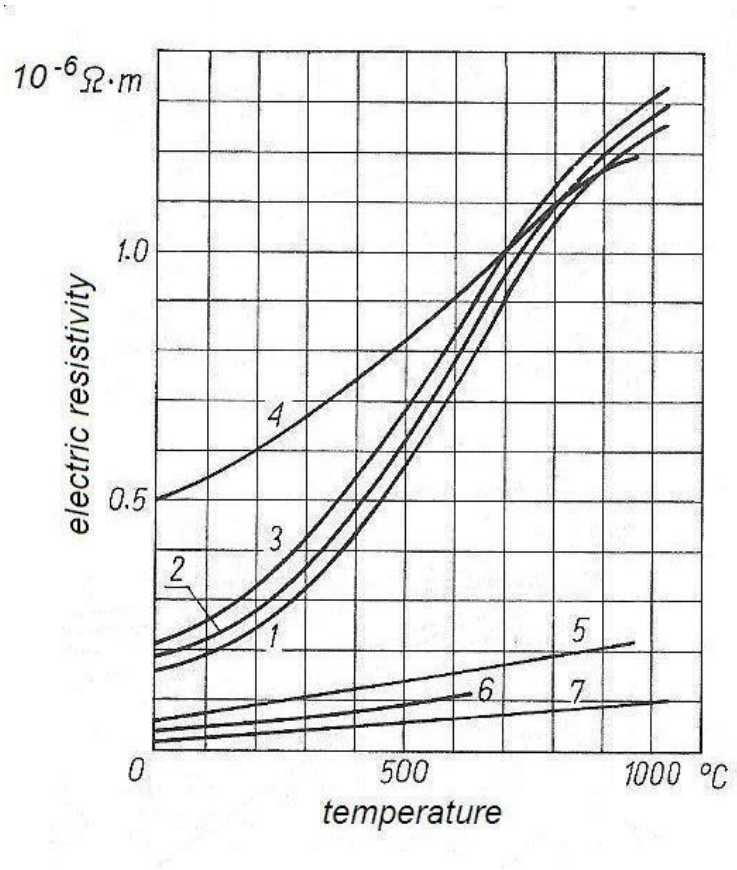

Figure 29: Variation of resistivity ρ of metals with temperature: 1,2,3| various mild steels, 4|stainless and acid resistant steels, 5|brass, 6|aluminium, 7|copper. [12]

3.8 Model Materials

3.8.1 Introduction

In the last part of the chapter we are going to analyse which materials we used in our parts and why.

3.8.2 Iron Poles

For the Iron poles we have used a soft-iron, that because are used to concentrate the magnetic flux that comes from the axially magnetized Magnets, and so the most important aspect to analyse is there way of magnetizing themselves, for that reason is necessary the introduction of the BH-curve (Appendix B).
We start from the Soft Iron (without losses), that is a predefined material in COMSOL. After that, taking in consideration the ARMCO Datasheet we have modified the Electrical Conductivity and the BH Curve, as we can see in figure 30

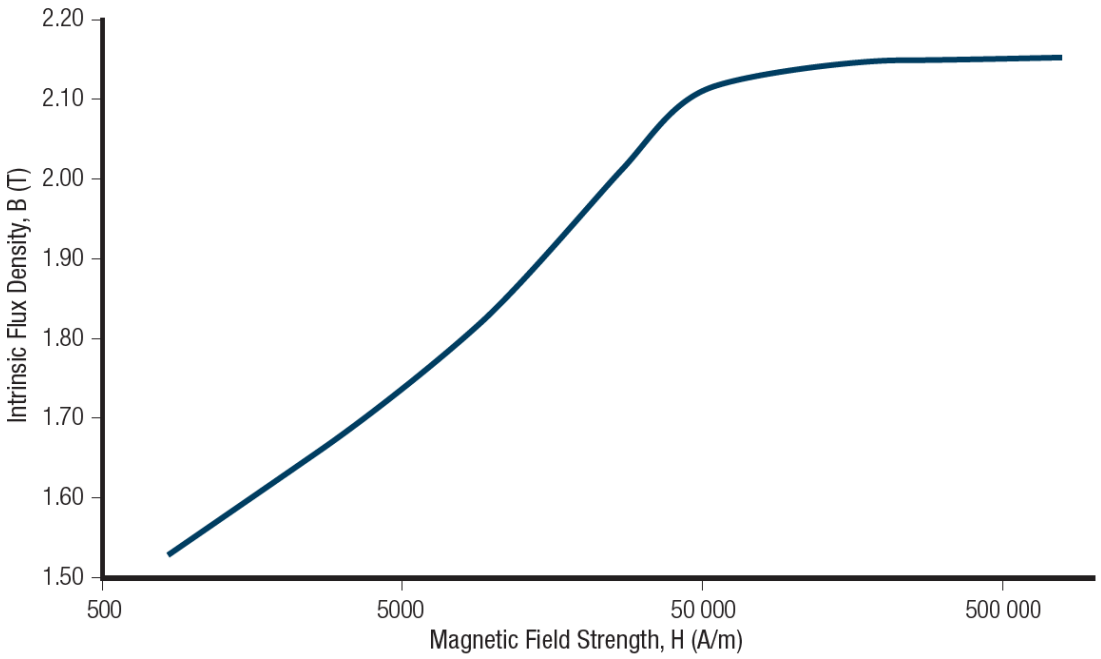

Figure 30: HIGH INDUCTION MAGNETIZATION CURVE FOR ARMCO® PURE IRON

From above figure it is important to extrapolate the saturation values of both the magnetic flux (B) and the magnetic field strength (H).
This because when we are going to model our geometrically optimised system we should also evaluate its compliance with the conditions of the materials used.

From definition, the saturation is the state reached when an increase in applied external magnetic field H cannot increase the magnetization of the material further, so the total magnetic flux density B more or less levels off.
So, this particular situation must be avoided.

3.8.2 Permanent magnets

For the permanent magnets we have used the N50 magnet type, the figure 31 shows the BH curve

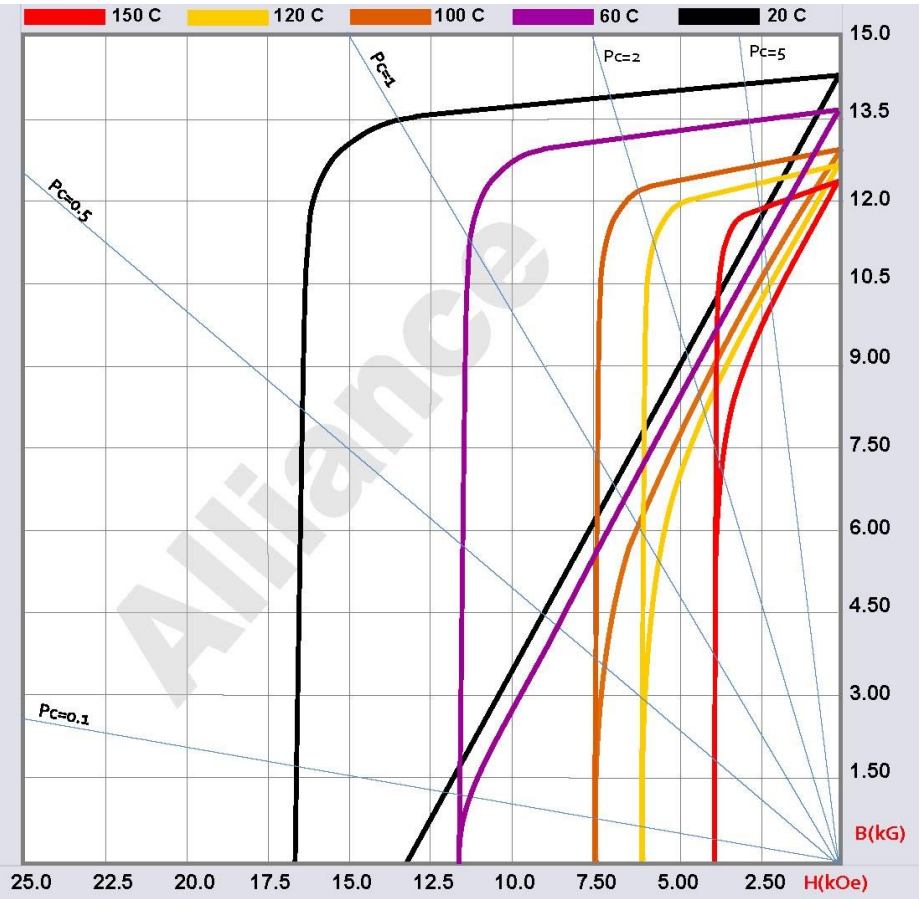

Figure 31: BH-curve of NdFeB N-50H magnet [16]

And the main characteristics are explained in the following table [16]:

Residual Induction Br	G	14,500	14,100
Coercive Force Hc	Oe		13,000
Intrinsic Coercive Force Hci	Oe		17,000
Max. Energy Product (BH)max	MGOe	50	48
Material Density	Lb/in3	.2673	
Max. Operating Temperature	C	120	
Temperature Coefficient for B	-%/C	-0.11	
Temperature Coefficient for H	-%/C	-0.62	
Required Magnetizing Force	Oe	60,000	
Material Composition	Nd, B, Fe, Dy, Co		

The B_r and H_c values in the remanent flux density (that initially have been set constant) are implement through Eq. of demagnetization already explained in this chapter.

3.8.3 Coils

For the coils we have used the copper because we need a low electrical resistance to simplify the birth of the eddy current. In fact, low electrical resistance means that it is easy for the current to flow through it. Also, copper wire can be easily shaped to make a coil.

3.8.4 Back-iron (casing)

For the back-iron (casing) we have used the Jiles-Atherton hysteretic material.
The properties of that material were already explained in this chapter.

Chapter 4

Energy Recovery Systems

4.1 Introduction

Since the energy-saving idea in automobiles was introduced in the 20th century, energy efficiency has gained attention in the automobile industry. That ideas come from the continuously increasing of demand of energy, the environmental problems (as said in Chapter 1) and due the fact efficiency of an ordinary car, as we can see in Figure 32, is below 75%.

Engine losses	**75.2 %**
- Thermal losses	63.5 %
- Pumping losses	5 %
- Combustion inefficiency	3.4 %
- Friction losses	3.3 %
Auxiliary	**2.3 %**
- Alternator	2.3 %
Power to wheels	**22.5 %**
- Vehicle inertia	5.7 %
- Aerodynamic drag	3.8 %
- Rolling resistance	3.8 %
- Torque converter	1.7 %
- Other drag	1.7 %
- Transmission	1.4 %
- Differential	1.2 %
- Others	3.2 %

Figure 32: Energy consumption distribution of an ordinary automobile in the urban transport [17]

The greatest contribution is made by irreversibility (thermal losses, friction losses, pump losses, incomplete combustion, etc.) that occur in the engine section. Looking again the table we can see that the Power to wheels, energy demand for movement and management, is 22.5%; this amount regards the resistance of the wheels against road and due weather conditions, along with other losses. Considering that data development

on reduce energy losses to the minimum at the powertrain of the vehicle have great importance on the fuel economy and global energy efficiency. [18] "By definition, energy recovery is the conversion of energy losses occurring in various stages of the processes occurring in mechanical systems that are powered by an energy source into the form of available energy through specially designed devices and re-use in the case of need. The recovered/harvested energy can be used to actuate various electrical devices" [11] or to recharge the battery to increase range.

Therefore, analysing the various losses, we can conclude that those related to kinetic energy represent a large part of the total and thus certainly deserve to be recovered. Regenerative braking systems and suspension systems for energy harvesting, the two main kinetic recovery systems, are the subjects of the research.

4.2 Kinetic Energy Harvesting

4.2.1 Introduction

"Kinetic energy harvesters, also known as vibration power generators, are typically, although not exclusively, inertial spring-mass systems. Electrical power is extracted by employing one or a combination of different transduction mechanisms. Main transduction mechanisms are piezoelectric, electromagnetic, and electrostatic. As most vibration power generators are resonant systems, they generate maximum power when the resonant frequency of the generator matches ambient vibration frequency." [11]

4.2.2 Principle of Kinetic Energy Harvesting

Kinetic Energy harvester are modelled as a 1-DOF spring-mass system. The model was firstly developed by Williams and Yates.[19] Looking at the Figure 33 we can model the generator with a seismic mass (m) and a spring of constant (k). When the generator vibrates, the mass moves out of phase with generator housing, that cause a relative movement between mass and housing.

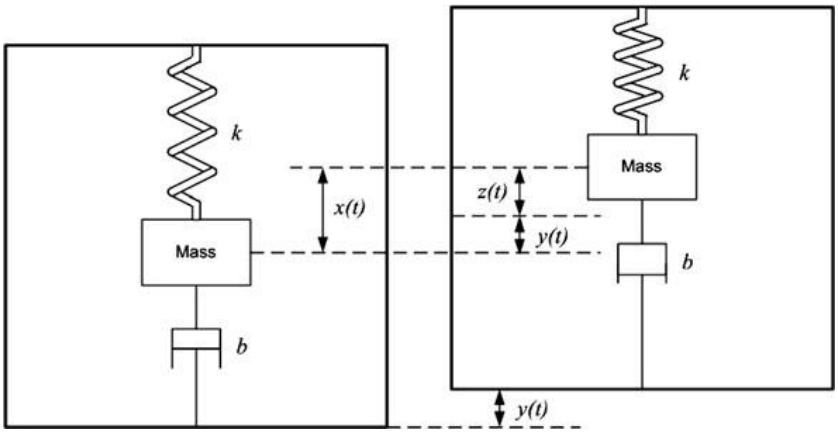

Figure 33: Generic model of kinetic energy harvesters [11]

Generally, this displacement is sinusoidal and drive a transducer, that generates electrical energy. For that kind of input the function *y(t)* can be written as $y(t) = Y \sin \omega t$, where Y is the amplitude of vibration and w is the angular frequency of vibration.

The electrical energy can be generated either by exploiting the mechanical strain or relative displacement. The former utilizes the deformation within the mechanical system, while in the latter either velocity or position can be coupled to a transduction mechanism.

Usually, speed is associated with electromagnetic transduction while relative position is associated with electrostatic transduction. [11]

4.2.3 Mathematical Point of View

For analysing mathematically, the system we must find the Transfer Function. Assuming the mass of the vibration source much greater than seismic one the vibration source is unaffected by the movement of the generator. Considering the dynamic forces on the mass we can write the differential equation of the movement mass with respect to the generator housing, as

$$m \cdot \frac{d^2z(t)}{dt^2} + b \cdot \frac{dz(t)}{dt} + k \cdot z(t) = -m \cdot \frac{d^2y(t)}{dt^2} \tag{4.1}$$

which, after applying Laplace, became

$$m \cdot s^2 \cdot z(s) + b \cdot s \cdot z(s) + k \cdot s \cdot z(s) = -m \cdot a(s) \tag{4.2}$$

where *a(s)* is the Laplace expression of the acceleration of the vibration, *a(t)*, which is given by

$$a(t) = \frac{d^2y(t)}{dt^2} \tag{4.3}$$

Thus, the transfer function is

$$\frac{z(s)}{a(s)} = \frac{1}{s^2 + \frac{b}{m}s + \frac{k}{m}} = \frac{1}{s^2 + \frac{\omega_r}{Q}s + \omega_r^2} \tag{4.4}$$

where $Q = \frac{\sqrt{km}}{b}$ is the quality factor and $\omega_r = \sqrt{k/m}$ is the resonant frequency.

4.2.4 Equivalent Circuit

From the Transfer Function we can also derive the equivalent circuit, that is an equivalent electrical circuit for a kinetic energy harvester, as

$$-m \cdot a(s) = s \cdot Z(s)\left(ms + b + \frac{k}{s}\right) \tag{4.5}$$

that can be rewritten as

$$-I(s) = E(s)\left(sC + \frac{1}{R} + \frac{1}{sL}\right) \tag{4.6}$$

where $I(s) = m \cdot a(s),\ E(s) = s \cdot Z(s),\ C = m,\ R = \frac{1}{b}\ ,\ L = \frac{1}{k}$. Based on Eq. (6), an equivalent electrical circuit can be built as shown in Figure 34.

4.2.5 Damping in Kinetic Energy Harvesting

Damping in kinetic energy harvesting consists of mechanically induced damping and electrically ones.

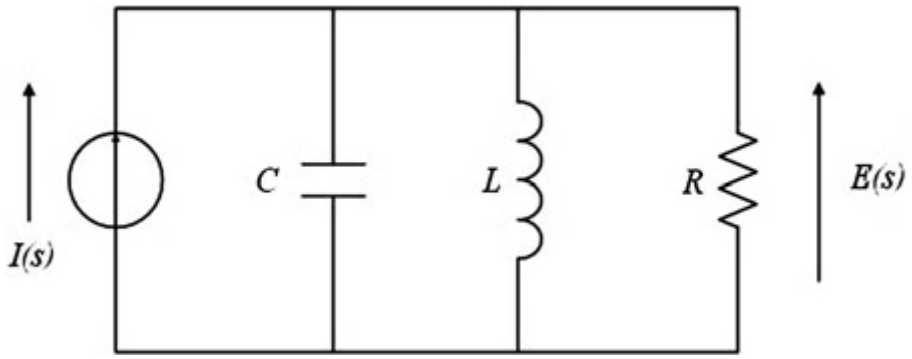

Figure 34: Equivalent circuit of a kinetic energy harvester[11]

$$\zeta_T = \frac{b}{2m\omega_r} = \frac{b_m + b_e}{2m\omega_r} = \zeta_m + \zeta_e \tag{4.7}$$

where $\zeta_m = \frac{b_m}{2m\omega_r}$ and $\zeta_e = \frac{b_e}{2m\omega_r}$ are, respectively, the mechanical and electrical induced damping factors.

We can now introduce the Quality Factor (Q-factor) as function of damping factor, therefore given by

$$Q_T = \frac{1}{2\zeta_T} \tag{4.8}$$

This is the Q-factor when generator is connected to the optimum load. It is therefore possible derive the relationship between total quality factor and the electrical and mechanical damping, as

$$\frac{1}{Q_T} = \frac{1}{Q_{OC}} + \frac{1}{Q_e} \tag{4.9}$$

where $Q_{OC} = \frac{1}{2\zeta_m}$ is in open circuit and reflects the mechanical damping. Instead, $Q_e = \frac{1}{2\zeta_e}$, reflects performance of the transduction mechanism.

4.2.6 Output Power

Considering the same input mentioned above, i.e. $y(t) = \sin \omega t$, we can find the solution of Eq. (4.1) as

$$z(t) = \frac{m\omega^2 Y}{k - m\omega^2 + j\omega b} \cdot \sin \omega t \tag{4.10}$$

that rearranged become

$$z(t) = \frac{\omega^2}{\sqrt{(\omega_r^2 - \omega^2)^2 + \left(\frac{b\omega}{m}\right)^2}} \cdot Y \sin(\omega t + \varphi) \tag{4.11}$$

where phi is the phase angle given by

$$\varphi = \tan^{-1}\left(\frac{b\omega}{k - \omega^2 m}\right) \tag{4.12}$$

"The average power dissipated within the damper, i.e. the sum of the power extracted by the transduction mechanism and the power lost in mechanical damping is given by: "[11]

$$P = b\left(\frac{dz(t)}{dt}\right)^2 \tag{4.13}$$

"Equations (4.11) and (4.13) give the average power dissipated within the damper as follows:"[11]

$$P(\omega) = \frac{m\zeta_T Y^2 \left(\frac{\omega}{\omega_r}\right)^3 \omega^3}{\left[1-\left(\frac{\omega}{\omega_r}\right)^2\right]^2 + \left(2\zeta_T \frac{\omega}{\omega_r}\right)^2} \tag{4.14}$$

"When the generator is at resonance, i.e. $\omega = \omega_r$, the power dissipation reaches maximum. The maximum dissipated power is:"[11]

$$P = \frac{mY^2\omega_r^3}{4\zeta_T} \tag{4.15}$$

or

$$P = \frac{mY^2\omega_r^3}{4(\zeta_m + \zeta_e)} \tag{4.16}$$

"The power dissipation is the sum of maximum electrical energy extracted by the transduction mechanism, P_e, and mechanical loss, P_m. P_e and P_m are as follows:"[11]

$$P_e = \frac{\zeta_e mY^2\omega_r^3}{4(\zeta_m + \zeta_e)} \tag{4.17}$$

$$P_m = \frac{\zeta_m m Y^2 \omega_r^3}{4(\zeta_m + \zeta_e)} \tag{4.18}$$

Where the maximum power conversion occurs when $\zeta_e = \zeta_m$, i.e. when the rise of damp in electrical domain equals mechanical losses. Therefore, we can compute the maximum electrical power harvested from kinetic energy, as

$$P_e = \frac{P}{2} = \frac{m Y^2 \omega_r^3}{16\zeta_m} \tag{4.19}$$

Rearrange consider $a = Y\omega^2$ (peak acceleration of the base) and $Q_{oc} = \frac{1}{2\zeta_m}$ (Open circuit Q-factor) the Eq. 4.19 can be written as

$$P_e = \frac{m a^2}{8\omega_r} \tag{4.20}$$

Analysing deeply the Eq. 4.20 of the power that we have found we can notice that when we design a vibration generator to achieve maximum power output is very important to design the generator with a high Q-factor, that means low damping factor, and make the generator works at its resonant frequency. We can see how what has just been said is confirmed by the function of the power spectrum of a vibration-based micro-generator. That generator has a resonant frequency of 50Hz and, as we can see in the Figure 35, are shown the various curves related to the various Q-factors and damping factors.

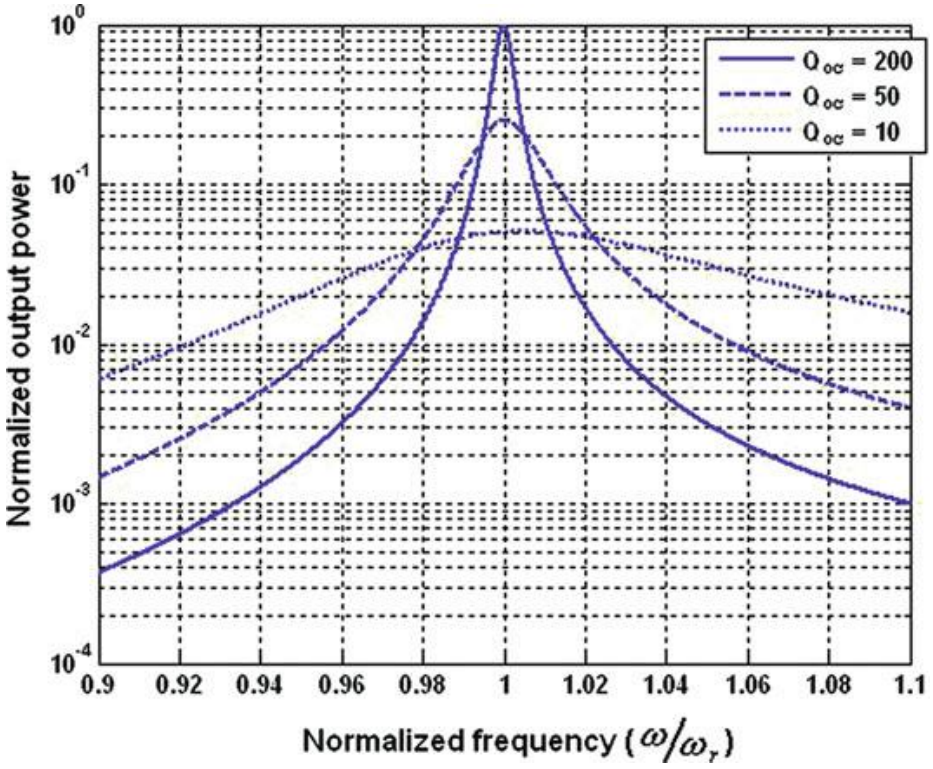

Figure 35: Power spectrum of a Kinetic energy harvester with various Q-factor[11]

"It can be seen that, for generators with a high Q-factor (i.e. low damping factor), the output power drops significantly if the frequency of operation is away from the generators resonance. When the Q-factor is lower (i.e. damping factor is higher), the peak output power decreases while the bandwidth of the generator increases and the device becomes less sensitive to frequency shifts at the expense of lower maxi- mum generated power. In addition, since the output power is inversely proportional to the resonant frequency of the generator for a given acceleration, it is generally preferable to operate at the lowest available fundamental frequency. This is com- pounded by practical observations that acceleration levels associated with environ- mental vibrations tend to reduce with increasing frequency. Application vibration spectra should be carefully studied before designing the generator in order to correctly identify the frequency of operation given the design constraints on generator size and maximum permissible z(t). Furthermore, the mass of the mechanical structure should be maximized within the given size constraints in order to maximize the electrical power

output. It should also be noted that the energy delivered to the electrical domain will not necessarily all be usefully harvested (e.g. coil losses)." [11]

The problem just shown is of central importance for our study, in fact, the search for maximum energy recovery leads us to work in conditions of low damping, this leads us to deduce that our damper will have a variable behaviour depending on the road on which it is located, in particular, it will be preferable to make it work as a generator only in situations of low damping, i.e. in the motorways; while in the remaining conditions (i.e. high damping factor) it will have to work like classical shock absorber.

4.3 Transductor Generator

4.3.1 Introduction

The key component allows you to extract electrical energy from motion is the transducer, which can be of type piezoelectric, electrostatic, and electromagnetic. The generator also requires a mechanical system, that must be designed to maximize coupling between mechanical energy source and transduction mechanism, to couple environmental displacements to transduction mechanism.

4.3.2 Piezoelectric Generator (PZ)

As mentioned above there are various kind of transducer; the Piezoelectric Generator (PZ) exploit the homonymous effect, i.e. "ability of some materials (notably crystals and certain ceramics) to generate an electric potential in response to applied mechanical stress. The electrical polarization is proportional to the applied strain. This is the piezoelectric effect used for mechanical to electrical energy conversion." [11]

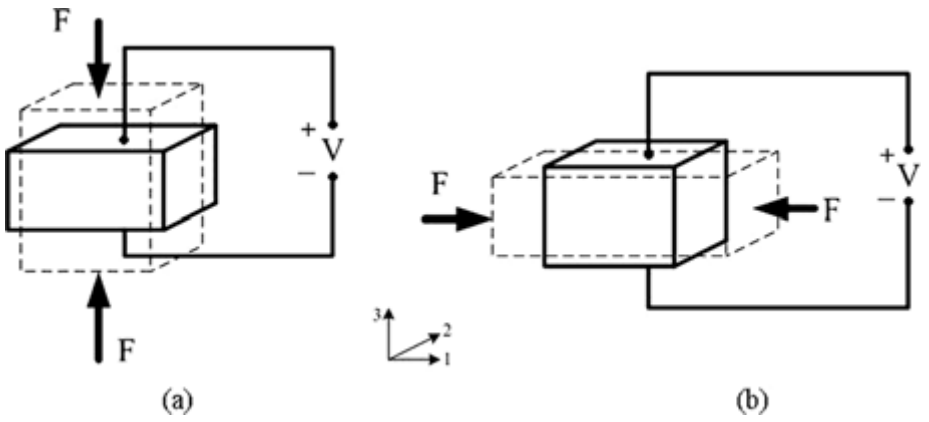

Figure 36: Piezoelectric generators: (a)33mode and(b) 31 mode[11]

As we can see in the Figure 36 above they works in two mode. "In the 33 mode, a force is applied in the same direction as the poling direction, such as the compression of a piezoelectric block that has electrodes on its top and bottom surfaces. In the 31 mode, a lateral force is applied in the direction perpendicular to the poling direction, an example of which is a bending beam that has electrodes on its top and bottom surfaces. Generally, the 31 mode has been the most commonly used coupling mode although the 31 mode has a lower coupling coefficient than the 33 mode." [20] [11]

4.3.3 Electrostatic Generators (ES)

Another kind of transducer is the Electrostatic Generators (ES); that kind of generator works with a variable capacitance that is driven by mechanical vibrations. "If the charge on the capacitor is constrained, charge will move from the capacitor to a storage device or to the load as the capacitance decreases. Thus, mechanical energy is converted to electrical energy. Electrostatic generators can be classified into three types, i.e. in-plane overlap (Fig. 34a) which varies the overlap area between electrode fingers, in-plane gap closing (Fig. 34b) which varies the gap between electrode fingers and out-of-plane gap closing (Fig. 34c) which varies the gap between two large electrode plates."[18] [11]

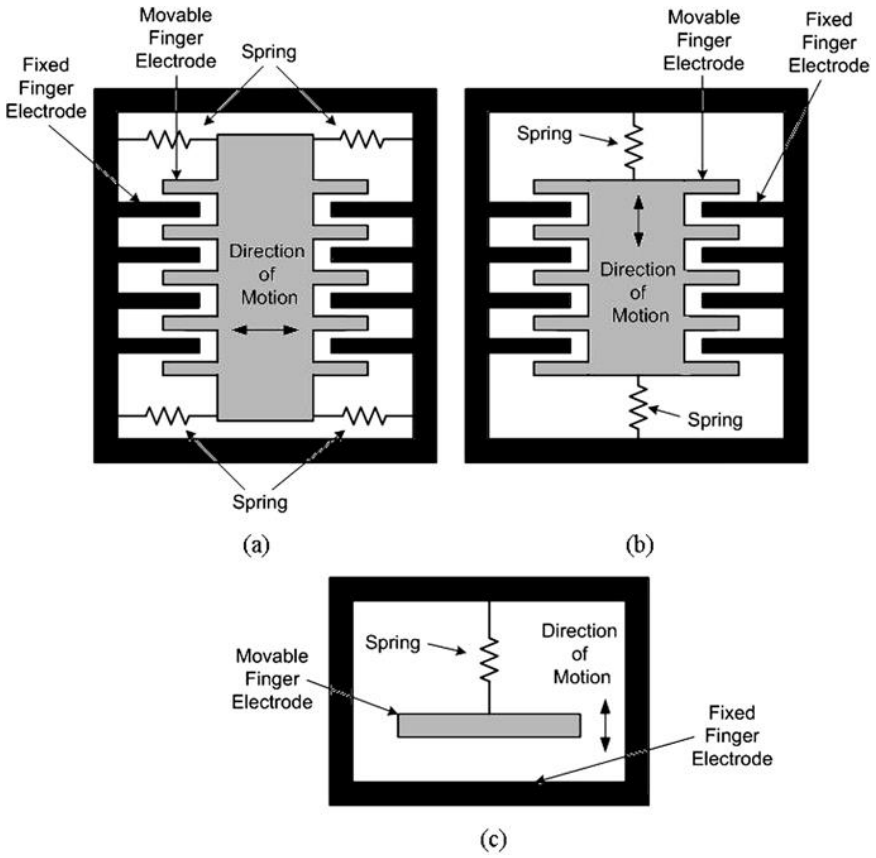

Figure 37: Electrostatic generators: (a) in-plane overlap; (b) in-plane gap closing; and (c) out-of-plane gap closing [11]

"These three types can be operated either in charge-constrained or voltage constrained cycles. Generally, generators working in voltage-constrained cycles provide more energy than generators in charge-constrained cycles. However, by incorporating a capacitor in parallel with the energy harvesting capacitor, the energy from the charge-constrained system can approach that of the voltage-constrained system as the parallel capacitance approaches infinity. This parallel capacitor effectively constrains the voltage on the energy harvesting capacitor".[21] [11]

4.3.4 Electromagnetic Generators

The last kind of studied transducer is the Electromagnetic Generator (EM); this type of generator exploits Faraday's electromagnetic induction. The homonymous law says that an electrical current will be induced in any closed circuit when the magnetic flux

through a surface bounded by the conductor changes. "This applies whether the field itself changes in strength or the conductor is moved through it. In an electromagnetic generator, permanent magnets are used to produce strong magnetic field and a coil is used as the conductor. Either the permanent magnet or the coil is fixed to the frame while the other is attached to the inertial mass."[11]

"The induced voltage, also known as electromotive force (e.m.f), across the coil is proportional to the strength of the magnetic field, the velocity of the relative motion and the number of turns of the coil. An electromagnetic generator is characterized by high output current level at the expense of low voltages. figure 38 shows two commonly seen examples of electromagnetic generators."[11]

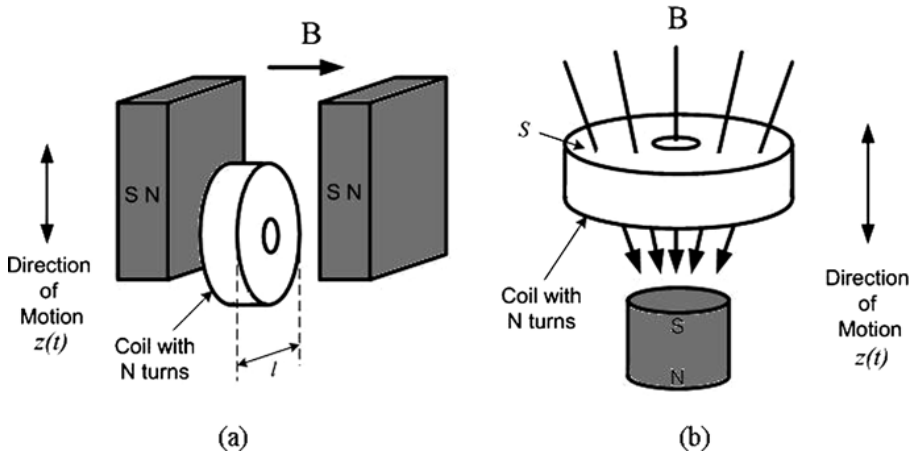

Figure 38: Electromagnetic generators [11]

Taking in account the figure, for the case (a) the magnetic field **B** is uniform. The magnetic field is interdicted by the coil, and therefore varies with the relative movement of the coil with the magnets. In this case, the electromotive force is given by

$$e.m.f. = -N \cdot l \cdot B \cdot \frac{dz}{dt} \tag{4.21}$$

where N is the number of turns of the coil, l is the effective length of the coil, B is the flux density going through the coil and *dz/dt* is the relative velocity between the magnets

and the coil.
Otherwise, for the case (b), the magnetic field (B) varies with the distance from the magnet and so, the induced electromotive force is

$$e.m.f. = -N \cdot S \cdot \frac{dB}{dz} \cdot \frac{dz}{dt} \tag{4.22}$$

where S is the effective area of the coil and dB/dz is the gradient of the magnetic flux density along the direction of relative motion between magnets and the coil.
We can see from the equations that in both cases the emf is function of the relative movement velocity and therefore expressions can be expressed by

$$e.m.f. = k \cdot \frac{dz}{dt} \tag{4.23}$$

where κ is the electromagnetic coupling factor which equals $-N \cdot l \cdot B$ and $-N \cdot S \cdot \frac{dB}{dz}$ in both cases, respectively. It represents the change in coupled flux per unit displacement.

4.3.5 Comparison of transducers

We have previously studied the various kind of transducers, by analysing what laws they exploit, how they work and therefore we can deduct from that their advantages and disadvantages which for ease of reading we have summarized in the figure 39 below.

Type	Advantages	Disadvantages
Electromagnetic	• No external voltage source • No mechanical constraints needed • High output current	• Difficult to integrate with MEMS fabrication process • Poor performance in micro-scale • Low output voltage
Piezoelectric	• Simple structure • No external voltage source • Compatible with MEMS • High output voltage • No mechanical constraints needed	• Thin films have poor coupling • Poor mechanical properties • High output impedance • Charge leakage • Low output current
Electrostatic	• Easy to integrate with MEMS fabrication process • High output voltage	• Mechanical constraints needed • External voltage source or pre-charged electret needed • High output impedance • Low output current
Magnetostrictive	• Ultra-high coupling coefficient • High flexibility	• Non-linear effect • May need bias magnets • Difficult to integrate with MEMS fabrication process

Figure 39: Comparison of different transduction mechanism of kinetic energy harvesters [11]

As we can well note, the electromagnetic transducer is the one with the most suitable characteristics for our application. In fact, analysing the advantages described, we can see how they fully reflect the characteristics we are looking for in a recovery shock absorber, while, on the other hand, the disadvantages are not a problem as they are characteristics that are not important for them.

After analysing the various types of transducer, we focus on the two main kinetic energy recovery systems, namely Energy Harvesting Brakes and Energy Harvesting Dampers.

Summing up, the energy recovery process is of the type catching and storing.

4.4 Energy Harvesting Brakes

4.4.1 Introduction

The braking system in a vehicle is certainly one of the most important component, it must meet two fundamental requirements: the first, in emergency braking, it must bring vehicle in rest in shortest possible distance (i.e. able to supply sufficient braking torque on all the wheels); the second, it must keep control over vehicle's direction (i.e. braking force to be distributed on all the wheels equally).

In electric vehicles (EV), in addition to the functions mentioned above, they have the ability to recover significant amounts of braking energy, this can happen controlling the electric motors as generators converting kinetic or potential energy of vehicle mass into electric ones.

Analysing losses in a vehicle, a significant amount of energy is consumed by braking. This is an inevitable loss of energy, given the construction of the braking system, in fact, the brake pads impose pressure on the wheel disc to reduce, or make it zero, the speed. "While the vehicle slows down, the kinetic energy is dissipated as heat due to friction. The amount of this transformed energy due to braking depends on how frequently braking is applied, how hard it is done and on the duration of braking."[17]

4.4.1 Example

To get an idea we have considered a passenger car of 1500kg that brakes from 100km/h to zero, it consumes about 0.16kWh of energy. When vehicles are driving with a stop-and-go pattern in urban areas, a significant amount of energy is consumed by frequent braking, which results in high fuel consumption. Figure 40 shows the total traction energy on driven wheels, energies consumed by drags (rolling resistance and aerodynamic drag) and braking of a 1500 kg passenger car. Figures 40 and 41 indicate that the braking energy in typical urban areas may reach up to more than 25% of the total traction energy. In large cities, such as New York, it may reach up to 70%. It is

concluded that effective regenerative braking can significantly improve the fuel economy of EVs and HEVs.[22] [23]

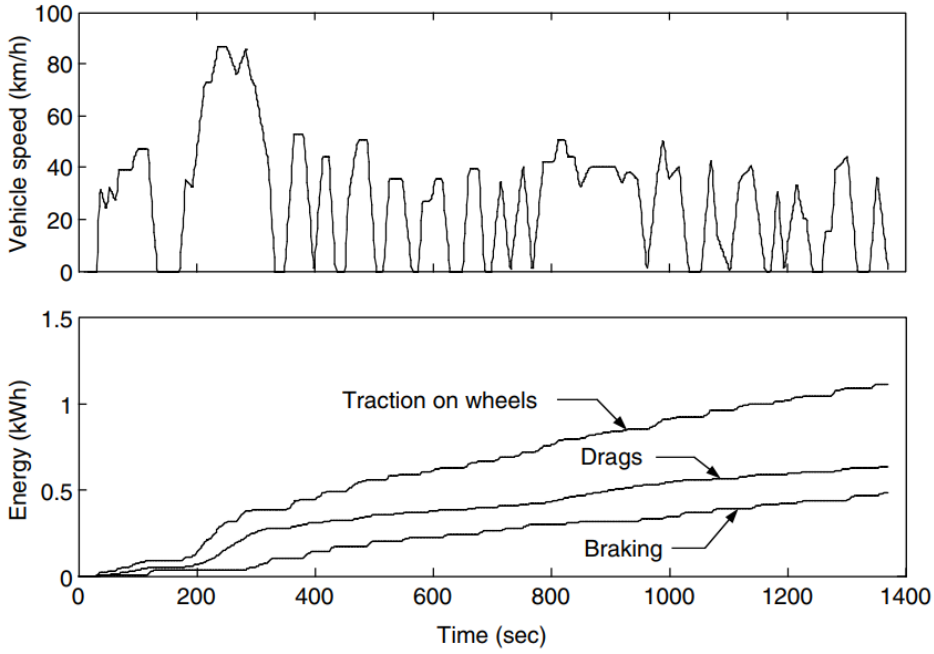

Figure 40: Total traction energy and energies consumed by drags and braking in an FTP 75 urban driving cycle [23]

Maximum Speed, Average Speed, Total Traction Energy, and Energies Consumed by Drags and Braking per 100 km Traveling Distance in Different Drive Cycles

	FTP 75 Urban	FTP 75 Highway	US06	ECE-1	New York City
Maximum speed (km/h)	86.4	97.7	128.5	120	44.6
Average speed (km/h)	27.9	79.3	77.5	49.9	12.2
Total traction energy[a] (kWh)	10.47	10.45	17.03	11.79	15.51
Total energy consumed by drags[a] (kWh)	5.95	9.47	11.73	8.74	4.69
Total energy consumed by braking[a] (kWh)	4.52	0.98	5.30	3.05	10.82
Percentage of braking energy to total traction energy (%)	43.17	9.38	31.12	25.87	69.76

[a]Measured on driven wheels.

Figure 41: Maximum Speed, Average Speed, Total Traction Energy, and Energies Consumed by Drags and Braking per 100 km Traveling Distance in Different Drive Cycles [23]

The amount of energy recovered by regenerative braking generally depends on the sort of the storage unit, the efficiency of the powertrain, the driving situation, and the inertia of the vehicle.[24]

4.4.2 Overview of technology

"When regenerative braking is applied, the kinetic energy of the vehicle is transferred by the powertrain to an energy storage unit[25]. From past to present, the most– known braking systems, which provide energy regeneration, have utilized springs, flywheels, electrochemical batteries, and hydraulic accumulators as storage units[24]. Studies on regenerative braking started at the end of the 1800s. The first applications were installations of spring-type regenerative braking systems on the front wheels of bikes and horse-drawn cabs. Systems in which springs are employed as energy storage units are generally run directly by human power, for example bicycles, wheelchairs, etc. The characteristics of a torsion spring used as an energy storage element are determined by the weight and speed capacity of the vehicle[26]. In the 1930s, the regenerative braking technology took part in the Baku–Tbilisi–Batumi railway line[27]. In the 1950s, the Swiss Oerlikon company developed a gyro bus, which uses flywheels as an energy storage unit[28]. In the systems that utilize flywheels as energy storage units, the kinetic energy of the slowing vehicle is transformed into rotational motion energy and is stored by the flywheel. The flywheel is connected to the propeller shaft via a gearbox. An electric generator is employed so that the energy stored in the flywheel can be used in the vehicle's movement. When the vehicle needs propulsion or acceleration, the energy stored in the flywheel is transferred to the drive shaft as torque. The energy stored in the flywheel system is directly related to the weight of the flywheel and the number of revolutions of the flywheel[24 29]. Unlike the systems using the battery as an energy storage unit, the energy can be regenerated and stored in the flywheel even for short distances and short braking durations[30]. In the systems in which hydraulic accumulators are used as energy storage units, the energy recovered by braking is stored within a pressurized working fluid in a spherical or cylindrical vessel. The working fluid is usually nitrogen gas. When braking is applied, the engine driven by the wheels behaves as a hydraulic

pump and compresses the working fluid in the accumulator. Hydraulic accumulator systems are lighter, smaller and cheaper than other systems[24].”[17]

Thanks to the development of hybrid/electric technology vehicles the regenerative braking systems have become common, suffice it to say that the first model marketed, the Toyota Prius, dates back to 1997. On the other hand, the development of shock absorbers is far behind, and therefore interesting from a development point of view.

4.5 Energy Harvesting Dampers

4.5.1 Introduction

Vibration in vehicles is an undesirable phenomenon. Besides the increase of fuel consumption, the failure of vehicle components, vibrations at the other structures and environment, deterioration of passengers’ comfort and driving safety are among the known harmful effects of vehicle vibrations[31]. Vehicle vibrations can occur when wheels pass over a structural fault or obstacle on the road and the vehicle accelerates or decelerates.[32]

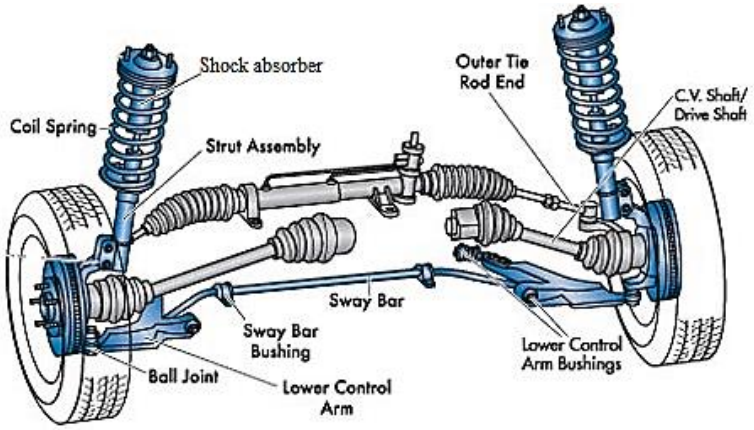

Figure 42: A typical road vehicle front suspension system[18]

Suspension system are one of the most important vehicle parts, they are designed to provide contact between vehicle’s tires and road and to isolate the frame from the road

disturbances, caused by vibrations. “The most important function of an ordinary vehicle suspension system is to provide road holding, drive control and travel comfort by damping the vertical and momentary movements (vibrations) transmitted from the wheels due to obstacles, structural obstacles, etc. during the wheel-road contact.”[17]
A suspension system is composed by a spring and a shock absorber, called also Damper. The latter are the heart of the systems, they are smoothing out the shock caused by sudden bump. The most common type of dampers used today is the hydraulic. In that kind the piston transfers the relative motion, which occurs in one direction (vibration), to viscous oil, which is the component that transform energy into heat, that will be lost in environment.[33]

In last years, thanks to the development of the fields of power electronics and magnetic materials these systems have become very interesting due to their low volume, weight, costs, and improving in efficiency and reliability. This, combined with the growing interest, as explained in Chapter 1, in fuel economy and environmental sensitivity have accelerated the development of the Energy Recovery Damper Systems. In that damper we have the conversion of mechanical energy into electromagnetic ones through an actuator, and the electromagnetic energy is stored by energy storage elements, which can reduce vibration and recover excess energy.[34] [35] [36] [37]

In general, spring stiffness is very important for the vibration energy harvester design since we would like to make the resonant frequency the same as the excitation frequency. However, the main excitation to vehicle suspension is road roughness, which is generally random and, often, can be modelled as white noise velocity input to the tires. [17]
Theoretically, the amount of vibration energy that could be recovered increases with vibration amplitude values, and the highest energy value could be obtained at the resonance frequency. [38]

Among possible choices of active ED implementation there are hydraulic and electromagnetic actuators. High reliability and dynamic performance, together with

lower volume, weight, and cost of electromagnetic actuators compared to their hydraulic competitors, justify the generalized use of electromagnetic actuators. Besides, it is verified that the hydraulic/pneumatic solutions are very expensive, heavy, and have high energy consumption, while the electromagnetic actuators have the advantage of suspension energy recovery.[39]

We have seen how the shock absorber has added energy recovery to its primary functions. Let us now analyse the fundamental component for this implementation, the actuator/generator, comparing the various types and justifying those we have chosen. Finally, we are going to show some technologies already present.

4.5.2 Linear vs Rotational motion machines

The first choice a designer makes when dealing with recovery dampers is certainly the linear or rotary design. The linear-type shock absorbers utilize the relative motion between magnetic field and coils to directly generate power based on Faraday's law of electromagnetic induction. The rotary shock absorbers transfer linear motion of suspension vibration to rotary motion to drive permanent magnetic dc generators. Usually, rotary shock absorbers are capable of generating more power and getting a larger damping coefficient for the given space[38] but they need a gearbox and/or complex mechanism -usually with poor performances especially at high frequency to convert the rotational motion into linear ones.
We can therefore deduce that, considering the simplest mechanical system due to the absence of the linear-to-rotary conversion system, the use of a linear actuator/generator is preferable. This leads us to good results in terms of accuracy and reliability.
"Here is a list of the fundamental benefits, arising from the use of direct thrust linear motors:
▹ Simple mechanical design with the minimum number of moving parts
▹ Direct thrust motors highly eliminate the backlash and wear
▹ Fast response-time (<10 ms)
▹ High acceleration with high motor force/weight ratio" [40]

The underlying principles are the same for both groups; they differ only in the construction and operation details. As already mentioned, we have chosen the linear ones, so let's go into them in more detail.

4.6 Linear machine design

4.6.1 Introduction

The first step in choosing the linear machine concerns with the type of current and then the type of motor to be used. The machines can be alternating current (AC) or direct current (DC). Due to the oscillating nature of the movement of a shock-absorber, alternating current machines are certainly the most correct choice.
Going now to analyse the various types of linear AC motors we notice how they are classified in based on how the energy conversion process takes place: synchronous, induction, and permanent magnet machines. [41]
The first two types, synchronous and induction, have windings in both the mover and the stator. The difference is that in synchronous the energy conversion process takes place at a fixed speed, called synchronous speed[42], and the transducer is powered by direct current (DC); while, on the other hand, in the induction one there is a moving magnetic field generated by an alternating excitation current (AC).
In the third type, the permanent magnet machine, the working magnetic field is created by the latter which can be mounted either on the stator or on the translator of the generator. The magnetic flux is modified by varying the magnetic field through the coils, by changing the magnetic permeability of the flux path for the magnetic field, or by moving the magnet with respect to the coil.
By analysing the three types of AC linear machines a permanent magnet tubular device is favoured as an electromagnetic damper for the construction of dampers.
In fact, both synchronous and induction machines need a kind of external excitation to convert the kinetic energy imposed at mover into electrical energy while permanent magnet machines are self-excited.

4.6.2 Linear Machine arrangement

The second step concerns with the analysis of the main components of a linear machine: the mover, or motive element and the stator, or static element.

These two basic elements can be arranged in a planar or tubular configuration, as we can see in figure 43.

The latter is certainly preferable for our use both from a mechanical resistance point of view, in fact all the components are inserted in a structure similar to the classic shock-absorber (piston-like structure); and from an electromagnetic point of view, in fact this configuration has a lower loss flow and has a higher induced emf (in the generator mode) and a higher thrust force (in the actuator mode).

Besides, since the PMs in the mover are completely encircled by the stator coils, the design is extremely efficient. They have also high duty cycle capability because of their intrinsic thermal efficiency and all-round heat dissipation.

Finally, for similar dimensions and weights, the force density achievable by tubular machines is greater than that of planar machines [25,26].

These advantages are given by the axial longitudinal symmetry of the device.

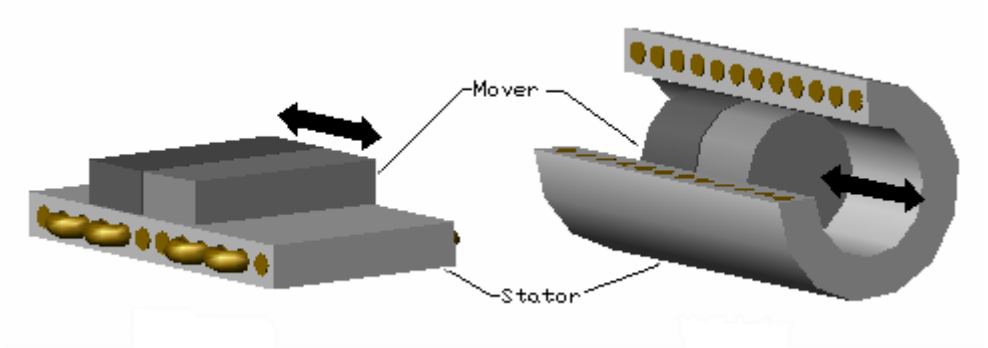

Figure 43: Basic Geometric Arrangements of Linear Electric Machines. Left: Planar, Right: Tubular

4.6.3 Linear Machine configurations

The third and last step concerns the arrangement of magnets and coils.

In both types, the mover (armour) can be either air- or iron-cored, where it could be either slotted or slotless. The choice of the correct motor topology is a compromise between different design requirements.

In general we can distinguish three configurations: (a) moving coil, (b) moving iron (c) moving magnet.

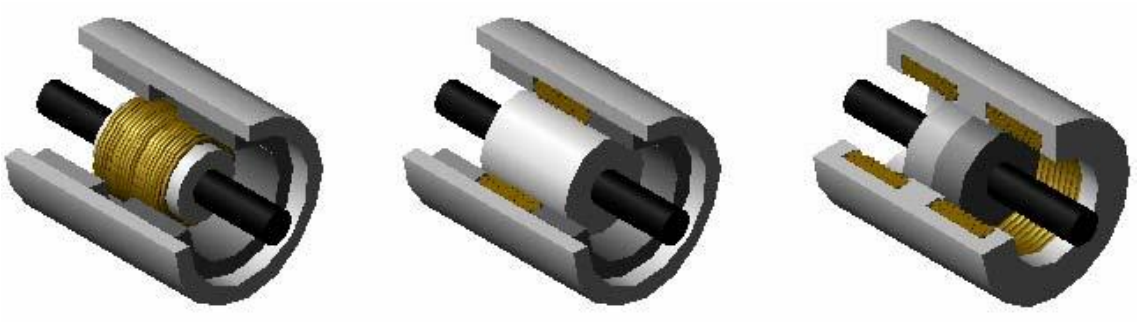

Figure 44: Permanent-Magnet Linear Machine Configurations.
From left to right: Moving Coil, Moving Iron, Moving Magnet

In the first one (a), the magnets are stationary in the armature and the coils are positioned on the armature (mover), brushes are needed to extract the electric energy induced in the coils moving through the magnetic field.
In the second type (b), the moving iron one, we have both the coils and the magnets placed on the mover. This configuration is robust and is the easiest to implement, but has a higher moving mass and a lower force per unit volume than the other two configurations[43].
The last configuration (c), the moving magnet one, has the mover which contains the permanent magnets while the armature (stator) houses the coils. Its operation is similar to that of the moving coil but with the roles of the stator and mover reversed. No electrical connection to the mover is necessary.
Grooved armatures usually have a higher force density than those without a groove, but can have a cogging force of the tooth ripple[44] as well as a variation of the coil inductance depending on the relative position of the armature and the mover.[44]

4.6.4 PM Magnetisation

After analysing the various stator/mover configurations we conclude with the magnetisation direction of the PM, the choice is dictated by various parameters.
The first is the damping coefficient C_{Xi} (which we will calculate in detail in the following

chapter), which, taking into consideration figure 45 and, therefore, the analysis of (Ebrahimi et Behrad, 2010)[45] we deduce as the best configuration is the one with the highest value of the coefficient itself.

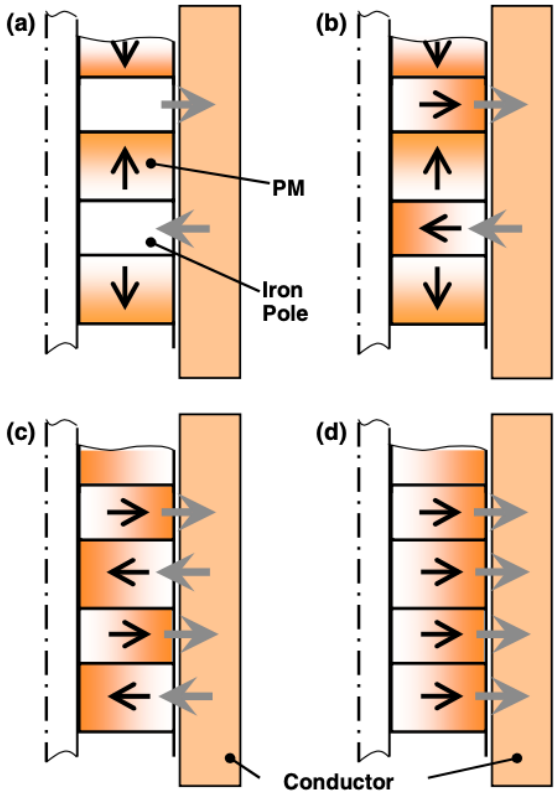

Figure 45: Different PM configurations in the mover. (a) Axially, (b) axially and radially,(c) radially (inward and outward), and (d) radially (outward) magnetized PMs in the mover [45]

Among the four configurations presented, (b) increases the damping coefficient up to 66%, compared to (a) and three times as much, compared to (c). The configuration (d) determines the lowest radial flux density, and therefore the lowest damping coefficient. We therefore deduce that the optimal configuration is that of figure 45b, and therefore that with radial PMs.

However, two other factors must also be taken into account, the force-volume ratio and the overall cost/performance ratio. In fact, if at first we might think that the radial solution is the best, if we consider these two other factors, we note that axially magnetised PMs in the mover determine a higher force-volume ratio (compared to

radially magnetised PMs) and furthermore, analysing the magnets market, we note that the radial type is rare and therefore our choice falls on type (a); which presents a good compromise between performance and cost.

4.6.5 Slotted and Slotless

As we have seen there are various configurations for tubular linear PM, with internal or external magnet positioning, with different magnet magnetization, both could be either moving magnet or moving coil. In all these topologies, the mover (armature) could be either slotted or slotless.

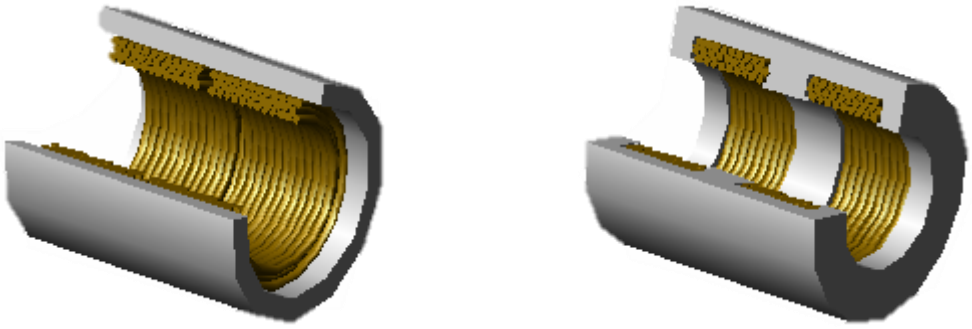

Figure 46: Tubular Machine Slot-less (left) and Slotted (right) Stator Illustrations.

Slotted reinforcement usually has a higher force density than slotless ones, but can have a tooth ripple cogging force[46] as well as a variation in coil inductance depending on the relative position of the armature and the mover[44].

4.6.6 Final consideration

We have analysed all existing types and configurations for linear motors. The final choice is dictated by various requirements and falls in the tubular core slotless with a moving magnet design in which the ring PMs are axially magnetized and alternated with the Iron Poles, threaded in the shaft, which allow a concentration of the flows and a mechanical locking of themselves and therefore also of the magnets.

4.7 ECD Overview

4.7.1 Introduction

Focusing specifically on systems that exploit the Eddy current phenomenon, we see how their application for damping purpose has been investigated for many years. One of the first was Sodano[47] who introduced a system to suppress beam's vibration. In this solution there is a fixed permanent magnet placed perpendicular to the movement of the beam and a conductive plate at the end of the beam. Sodano[48] himself later conceptually improved his model by adopting a theoretical approach, specifically applying an image method to meet the conditions around the conducting plate.
Elbuken et al[49,50] proposed another damping system in which a conductive plate is placed under the levitating object to suppress vibrations and thus ensure stability.
Graves et al[51] conducted a theoretical study comparing motional emf with transformer ones. Transformer emf devices are based on the generation of emf in a stationary circuit, in which the emf is generated by a time-varying magnetic field linking the circuit. Motional emf devices are based on the generation of emf due to a moving conductor within a stationary magnetic field. Both of these designs can be used as damping elements for applications such as semi-active and regenerative vehicle suspension systems. The findings herein are provided so as to evaluate the most efficient device for such applications. The analysis consists of comparing the damping coefficient of the electromagnetic devices for a given magnetic field and given volume of conducting material.
Finally, Ebrahimi et al[52] has developed a new damping system based on the Eddy current phenomenon.

4.8 Final consideration

Eddy current dampers are an alternative to the traditional vibration suppression devices, that kind of system utilize the relative motion between a permanent magnet and a conductor to create a resistive force that is proportional to the velocity of the conductor

itself. That innovative solution can be used both for damping purpose and for energy recover; this thanks to the very nature of object.
In the next Chapter we will introduce a deeply analysis of that kind of damper and the relative equation that regulate it's behaviour.

Chapter 5

Development of Eddy Current Damper

5.1 Introduction

After having widely introduced what are the characteristics that a linear energy recovery machine must have, we are going to analyse the application of the eddy current damping phenomenon in passive dampers (i.e. able to work only in damping mode). The configuration analysed converts vibrations into heat, of which we are going to analyse two models, one simpler that requires the presence of an additional spring and one purely ECD.

5.2 Eddy Current Spring-Damper Design

5.2.1 Introduction

To design our ECD we started from a simplified passive model (i.e. that works in damping conditions only) so that we could make an analytical analysis in a lighter and more understandable way. We then went to define its geometry and based on the electromagnetic theory we calculated the magnetic flux density, the magnetic force and finally the eddy current damping force, that is the most important factor to find to analyse the damping effect. Based on the data obtained from this model we can then design more realistic and high-performance dampers with the help of the finite element method, only after the analysis of passive shock absorbers can we dedicate to energy recovery models.

5.2.2 Qualitative model design

The way of work of the eddy currents, already mentioned, consists in the generation of these last in the conductor.
They are due either to the movement of the conductor in the static field or to the

variation of the magnetic field intensity, starting respectively the electromotive forces of movement and transformation (emfs). The eddy currents generated here in turn create their own magnetic field which generates a repulsive force proportional to the speed of the conductor, the magnet and the moving conductor therefore behave like a viscous damper.

In the first studies on this subject the magnetic spring effect[53,54] and the eddy current effect[47,48,55] were analysed, only later was the correlation between these two effects also studied [52].

figure 47 is a diagram of the system that was proposed, consisting of two permanent magnets, whose similar poles are in proximity, and a conductive aluminium plate, which can operate with both spring and variable damping effect.

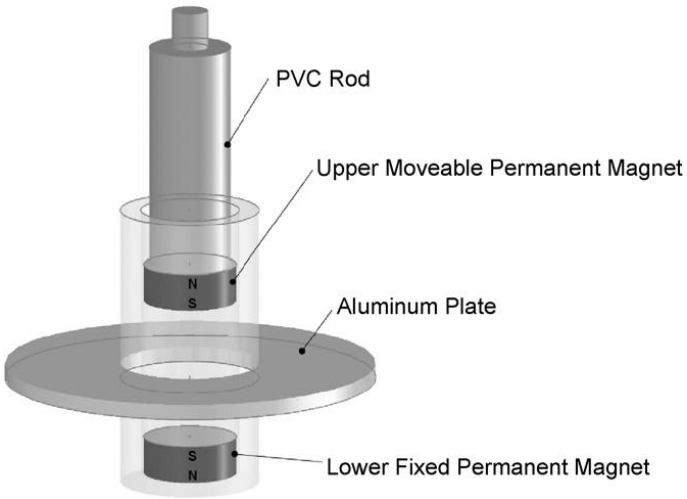

Figure 47: Schematic view of the proposed eddy current spring–damper

"The lower permanent magnet and the aluminium plate are fixed, while the upper magnet has an alternative motion. The use of a conductive ring plate simplifies manufacture, and its thickness does not limit the air gap of the magnets. The relative movement of the magnets causes the conductive plate to undergo a magnetic field that varies over time to generate an eddy current from the transformer. Since there is a

relative movement between the magnets and the conducting plate, a mobile eddy current is also generated".[52]

5.2.2 Analytical model design

The first step of the analytical study consists in calculating the magnetic flux density. Considering a single cylindrical permanent magnet we use the current method. [56]
The method used, studied by Furlani[56], tells us that a cylindrical magnet can be replaced by an equivalent magnetic volume current density $J_m = \nabla \times M$ and an equivalent surface current density $j_m = M \times \hat{n}$ that circulates around the body of the cylinder, where, M is the magnetization vector and $\hat{n}$ the unit surface normal. [16_2 design Ebrahimi]. Assuming a uniform magnetization and the cylindrical magnet polarized along its longitudinal direction with unit vector z (i.e. $M = M\hat{z}$), the surface and volume current densities are:

$$J_m = M\hat{\varphi}$$

$$J_m = 0 \tag{5.1}$$

where φ is the tangential unit vector. From Craik [17_2 ebrahimi] we can derive the flux density components along (r, z) for a cylindrical current sheet:

$$B_r = \frac{\mu_0 I}{2\pi L}\int_{-L/2}^{L/2} \frac{(z-z')}{r[(R+r)^2+(z-z')^2]^{1/2}}\left[-K(k) + \frac{R^2+r^2+(z-z')^2}{(R-r)^2+(z-z')^2}\right]dz'$$

$$B_z = \frac{\mu_0 I}{2\pi L}\int_{-L/2}^{L/2} \frac{1}{r[(R+r)^2+(z-z')^2]^{1/2}}\left[-K(k) + \frac{R^2-r^2-(z-z')^2}{(R-r)^2+(z-z')^2}\right]dz' \tag{5.2}$$

where $K(k)$ and $E(k)$ are the complete elliptic integrals of the first and second type, respectively, and are defined as:

$$K(k) = \int_0^{\pi/2} \frac{d\theta}{\sqrt{1 - k^2 \sin^2 \theta}} \tag{5.3}$$

and

$$E(k) = \int_0^{\pi/2} \sqrt{1 - k^2 \sin^2 \theta}\, d\theta \tag{5.4}$$

where

$$k^2 = 4Rr[(R + r^2) + (z - z')^2]^{-1}$$

Where the parameter *R* is the radius, while L is the length, both regards cylindrical permanent magnet; $I = ML$ is the equivalent current of the permanent magnet[57]. From Sodano[47], due Eq.(2) has not an analytical solution, we are going to use a numerical approach to solve the integrals.

The second step of the analytical analysis concerns the calculation of the repulsion force between the two adjacent permanent magnets. Considering the magnets as two single current carrying loops, and two solenoids, as in figure 48, we can obtain the force sought.

Then, applying Ampere's law, we can calculate the force to which a single current-bearing loop is subjected in the presence of another one of the same.

The above law establishes that when two current-carrying elements $I_1 dL_1$ and $I_2 dL_2$ interact each other, the elemental magnetic force, exerted by element 1 on element 2, is:

$$dF_{21} = \frac{\mu_0 I_2 dL_2}{4\pi} \times [\frac{I_1 dL_1 \times R_{21}}{R_{21}^3}] \tag{5.5}$$

where R_{21}, as illustrated below, is the distance vector between two elements; $R_1$and R_2 are the radii of loop one and two, respectively. We can now compute the magnetic force:

$$F_{21} = \frac{\mu_0}{4\pi} \int_{c2} I_2 dL_2 \times \int_{c1} \frac{I_1 dL_1 \times R_{21}}{R_{21}^3} \tag{5.6}$$

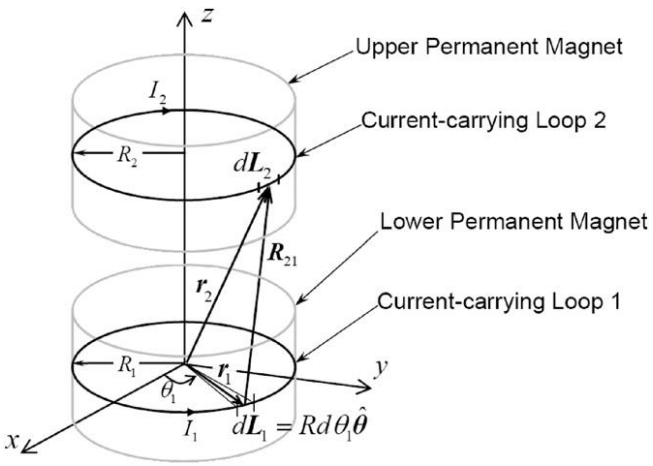

Figure 48: Schematic of two current-carrying loops, illustrating the variables used in Eq. [58]

Analysing the Eq.(5.6) we can see that the right integral is the magnetic flux density, in the area of the element 2, produced by the current-carrying loop 1. We can then calculate, when a current-carrying loop is placed in an external magnetic field B, the magnetic force as:

$$F = \int_c I\, dL \times B \tag{5.7}$$

If we assume $R_1 = R_2 = R$, we can find $F_z(z_d)$ that is the vertical component of the interacting forces between two current-carrying loops with opposite sign, and is expressed as:

$$F_z(z_d) = \frac{\mu_0 I_1 I_2 R^2}{4\pi} \int_0^{2\pi} \int_0^{2\pi} \frac{-z_d \cos(\theta_2 - \theta_1)\, d\theta_1 d\theta_2}{(2R^2 - 2R^2 cos(\theta_2 - \theta_1) + z_d^2)^{3/2}} \tag{5.8}$$

where z_d is the distance between the two loops.

Using again the current method, and integrating the Eq.(5.8), we can therefore find the vertical component of the interacting forces along the magnets 'length as:

$$F_z = \frac{\mu_0 I_1 I_2 R^2}{4\pi L^2} \int_{g/2}^{g/2+L} \int_{-L-g/2}^{-g/2} \int_0^{2\pi} \int_0^{2\pi} \frac{-[z_d - z' - z'']\, cos(\theta_2 - \theta_1)\, d\theta_1 d\theta_2 dz' dz''}{(2R^2 - 2R^2 cos(\theta_2 - \theta_1) + [z_d - z' - z'']^2)^{3/2}} \tag{5.9}$$

5.2.4 Eddy Current geometry dependency

To get a qualitative idea of the influence of geometry in eddy currents we can analyse figure 49.

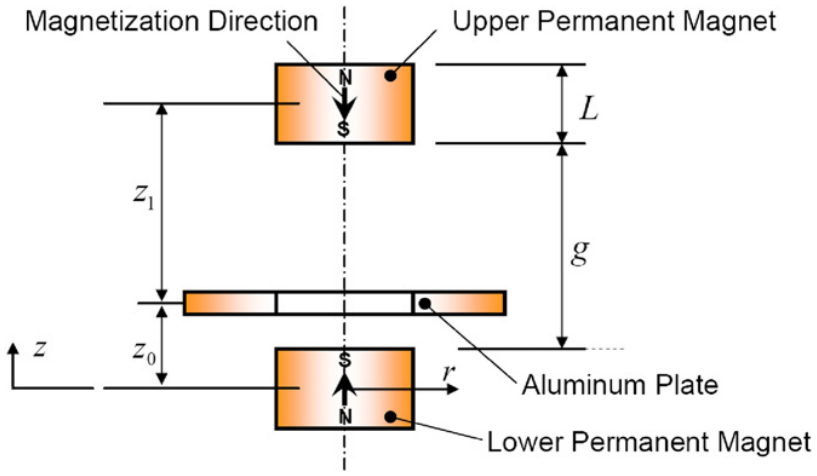

Figure 49: Geometric definition of the eddy current spring–damper

In it the aluminium plate is fixed while the upper permanent magnet moves, it is the latter that causes the generation of currents inside the plate itself, generating a magnetic field that varies over time.

5.2.5 Eddy current damping force

In general, however, we know that the total emf can be caused both by the condition just

described and by the relative motion of the conducting plate. These two contributions must be studied together and are the so-called "emf transformer", derived from Maxwell's third equation (Faraday's Law), and the "motional emf", derived from Lorentz's law of force. Thanks to these two contributions we have:

$$V = V_{trans} + V_{motion} = -\int_s \frac{\delta \boldsymbol{B}}{\delta t} \cdot d\boldsymbol{s} + \int_s (v \times \boldsymbol{B}) \cdot d\boldsymbol{l} \tag{5.10}$$

Now we can notice that the relative motion between the conductor and the magnets (that cause motional emf), is exactly the plate velocity (v). Due that velocity (v) has only vertical component, the vertical component of the magnetic flux density does not contribute to the generation of the motional eddy current (i.e., $\boldsymbol{v} \times \boldsymbol{B}_z = 0$). So, the motional emf depends only on the radial component of the magnetic flux density; therefore the current density J is:

$$\boldsymbol{J} = \sigma(v \times \boldsymbol{B}) \tag{5.11}$$

Finally, considering[48], we can find the damping force due the motional emf:

$$\boldsymbol{F} = \int_{\Gamma} \boldsymbol{J} \times \boldsymbol{B} d\Gamma = -\widehat{\boldsymbol{k}} \sigma \delta v \int_0^{2\pi} \int_{r_{in}}^{r_{out}} r B_r^2(r, z_0) dr d\theta \tag{5.12}$$

where Γ is the conductor volume. Analysing again figure 49 we notice that the total radial component of the magnetic flux density is the sum of the magnetic flux density, generated by the two permanent magnets at the mid-plane of the conducting plate such that:

$$B_{r,total} = B_r(z_0) + B_r(z_1) \tag{5.13}$$

where

$$z_1 = \begin{cases} L + g - z_0 \ \ if \ \ z_o < L + g \\ -L - g + z_0 \ \ if \ z_0 > L + g \end{cases}$$

The equations found, in particular the Eq. (5.12), is valid only assuming the infinite conductive plate, therefore the boundary conditions are not considered. This, however, since only a simplified analysis is now necessary, is not a problem we will take into account.

5.3 Eddy Current Damper Design

5.3.1 Introduction

In the previous paragraph we have seen, starting from a simple model, what are the factors at stake for the realization of a good passive ECD. We have therefore noticed that the magnetic flux density is the first parameter to be optimized, in particular we should modify the model geometrically so as to obtain the maximum intensity of the above. This can be achieved by modifying the geometry of the magnets and conductors. This damper model, like the previous one, has a passive operation.[59]However, the analysis of these models is necessary to fully understand our project.

5.2.2 Qualitative model design

The new model is closer to the classic idea of shock absorber; it consists of an external tube that acts as a conductor (static part), and of an internal part where are located permanent magnets alternating with iron poles. The latter are screwed to a shaft (element that allows motion), that inner part is in fact the slider ones. As already seen before, it is in the conductor that the eddy currents, that generate the damping, are made. They are in fact generated by the relative movement of the magnets with respect to the conductor (i.e. relative motion of the slider wrt stator), and therefore we can speak of emf motional. We also know that the repulsive force produced by eddy

currents is proportional to the speed of the conductor, so this system behaves like a viscous damper[59]. Below figure 50 that shows the model that consists of a tubular design, which has less leakage flux than a flat design, and is much better for using magnetic flux, leading to more eddy current generation.

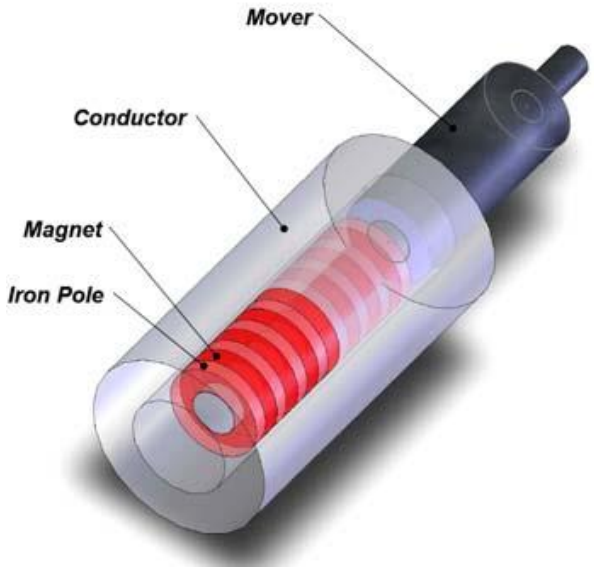

Figure 50: Schematic view of the proposed ECD

5.3.2 Analytical model design

Let's now consider figure 51 to analyse the model analytically, to do this the schematic configuration is represented.

The arrows in bold in the PM express the direction of magnetization (fixed), in fact, the magnetic field does not change as a function of time and therefore only the emf motional exists as a source of eddy currents. PMs are radially magnetized so as to obtain a higher specific force capacity (compared to radially magnetized PMs)[44]

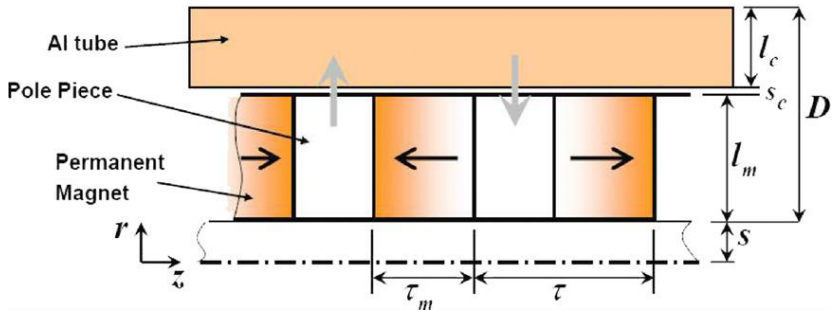

Figure 51: Configuration of the proposed ECD

As already seen for the first model, the physical phenomena are identical, so we can calculate the total induced emf, that is equal to the motional emf due magnetic field is constant

$$E = \cancel{E_{trans}} + E_{motional} = \int_c (v \times \boldsymbol{B}) \cdot dl \tag{5.13}$$

With the previous assumptions the induced current density *J* in the conducting sheet is

$$J = \sigma(v \times \boldsymbol{B}) \tag{5.14}$$

where σ is the conductivity. The magnetic field generated by the induced current density opposes the external one causing a damping force in the z direction. Therefore, we can derive from[47] the simplified formula of the damping force, which is

$$F = \int_\Gamma J \times B d\Gamma = -\hat{k}\sigma(\tau - \tau_m)v_z \times \int_0^{2\pi} \int_{r_{in}}^{r_{out}} r B_r^2(r, z_0) dr d\theta \tag{5.15}$$

where Γ is conductor's volume, r_{in} is inside radius, r_{out} is outside radius. τ and τ_m are pole pitch and the magnet's thickness, respectively. In conclusion, the equivalent constant damping factor is

$$C = \sigma \int_{\Gamma} B_r^2 d\Gamma \tag{5.16}$$

If we go deeply inside the model configuration, we can outline the PMs like figure 52.

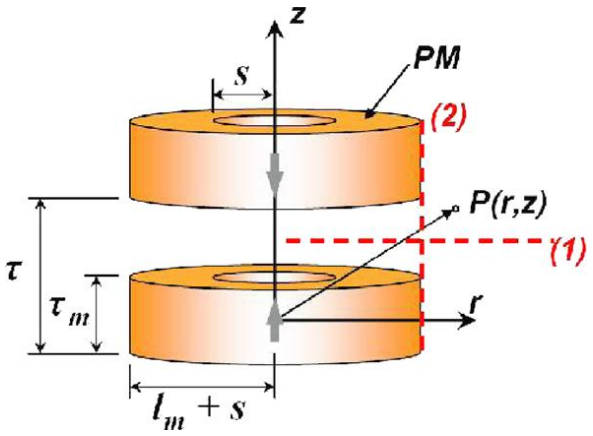

Figure 52: Schematic view of two PMs with like poles in close proximity

For a system like this we can therefore, thanks to Craik[57], calculates the magnetic flux density of a magnet with a reasonable complexity, as

$$\begin{aligned} B_r(r,z)|_{R,\tau_m} = \frac{\mu_0 I}{2\pi\tau_m} \int_{-\tau_m/2}^{\tau_m/2} \frac{(z-z')}{[(R+r)^2+(z-z')^2]^{1/2}} \\ \times \left[-K(k) + \frac{R^2+r^2+(z-z')^2}{(R-r)^2+(z-z')^2} E(k)\right] dz' \end{aligned} \tag{5.17}$$

where $K(k)$ and $E(k)$ are the complete elliptic integrals of the first and second kind, respectively, and are defined as

$$K(k) = \int_0^{2\pi} \frac{d\theta}{\sqrt{1-k^2\sin^2\theta}} \tag{5.18}$$

$$E(k) = \int_0^{2\pi} \sqrt{1 - k^2\, sin^2\, \theta}\, d\theta \tag{5.19}$$

where $k^2 = 4Rr[(R + r)^2 + (z - z')^2]^{-1}$.

"$I = M\tau_m$ is the equivalent current of the PM[56]. For the PMs, the axial magnetic fluxes, along dashed line 1 in figure 52, cancel each other, whereas the two radial fields are combined to produce a radial magnetic flux that is exactly twice as high as the one produced by a single magnet. Therefore, the total radial component of the magnetic flux density, B_r along dashed line 1 is given by"[59]

$$B_r = 2(B_r(r,z)|_{l_m+s,\tau_m} - B_r(r,z)|_{s,\tau_m} \tag{5.20}$$

From Sodano[47] we know that Eq. (5.17) does not have any analytical solution, so a numerical approach, for solving integrals, must be adopted.

We have therefore obtained all the necessary parameters to study the model according to our purpose. Also, in this model the boundary conditions and the particular condition like the Skin Effect, are not considered.

5.4 Eddy Current Regenerative Damper

5.4.1 Introduction

Take into account the model of figure 50 we have substituted the conductor with the coils to obtain the regeneration. The new model is like figure 53 above

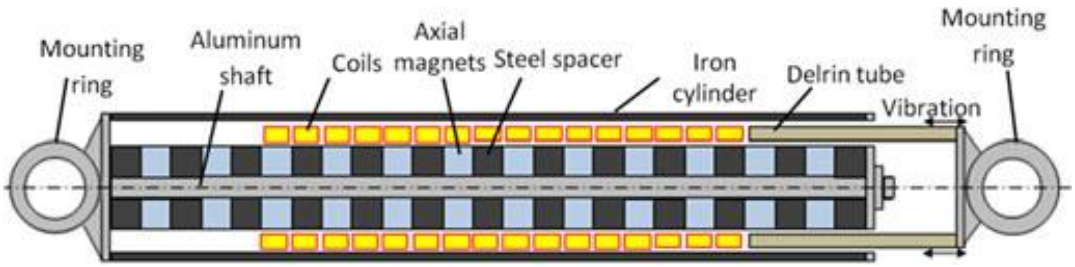

Figure 53: Diagram of the linear regenerative electromagnetic shock absorber.[60]

As we already said in Chapter 4, the mechanism converts the kinetic energy of suspension vibration (i.e., vibration between wheel and sprung mass) into electrical power which can be used by our vehicle.

The new eddy current damper have the slider like the previous one (i.e, composed by shaft, PMs and iron poles) and the stator composed by coils and a concentric outer cylinder made of iron that follow Jiles-Atherton hysteresis loop that works also like a casing.

5.4.2 Equivalent circuit

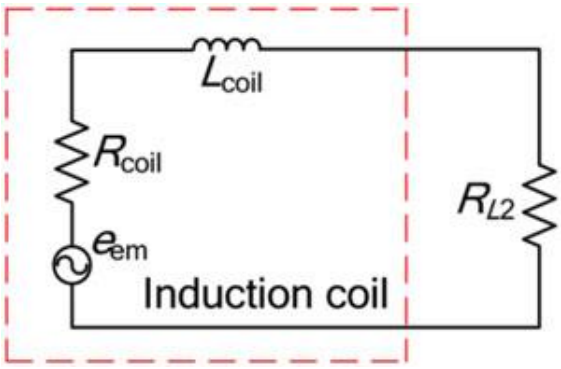

Figure 54: Equivalent circuit model of the energy harvester.[61]

The analysis of the equivalent circuit of an energy harvester allows us to refer the model to a theoretical circuit that retains all of the electrical characteristics of the system but with simple equations to analyse.

In particular we can see in the left part the coil while in the right (R_{L2}) the load resistance. From this figure is very clear that the voltage across the latter is equal to the coil ones (i.e., the power in output of coil is equal to the one dissipated by the resistance).

Therefore, to verify the correctness of the model, we have calculated analytically (as explained in the next paragraph) the power output from the coils and then compare it with the one dissipated by the external resistance.

5.4.3 Analytical model design

Based on the previous equations and the requirement of energy harvester we made a simplified analysis analytically that is just for guide ourselves into model physics. Subsequently the complete analysis was made with FEM method using COMSOL Multiphysics software.

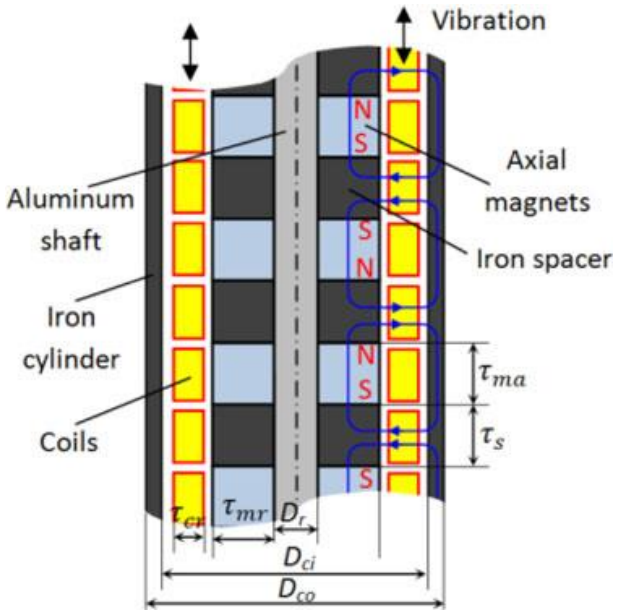

Figure 55: Linear regenerative electromagnetic shock absorber dimensions and parameters[60]

Our objective is to maximize the electrical power output, and so, knowing that

$$P = VI \tag{5.21}$$

and assuming an short-circuit system with a R_{load} to catch it.
So, we can start to compute the he $e.m.f.$ voltage (reference in Chapter 4) generated by a conductor of length l (m) moving in a constant magnetic field B_r, at constant velocity v, is given by

$$V = B_r v \quad l \tag{5.22}$$

The maximum current I generated by the device with short circuit is given by

$$I = \frac{V}{R} = \sigma B_r v_z A_w \tag{5.23}$$

where σ is the electrical conductivity of the conductor, B_r is the average magnetic flux density in the radial direction, v_z is the relative velocity of the conductor moving in the magnetic field in the axial direction and A_w is the cross-sectional area of the conductor itself. The peak power is calculated by combining the three previous equation as

$$P = VI = B_r^2 v_z^2 \sigma l A_w \tag{5.24}$$

The equation shows the importance of increasing the radial magnetic flux B_r, due the conductor velocity is given by the external excitation and due the square value of B_r. Finally, we replace the conductor with the coil introducing and we model the energy harvester to reach the maximum magnetic flux density.

Therefore, we have calculated the peak voltage of one coil with N turns, as

$$V = \pi N B_r v_z D_c \tag{5.25}$$

and the peak power, taking into account eq.(5.23), will be

$$P = \pi N \sigma B_r^2 v_z^2 D_c A_w \tag{5.26}$$

where D_c and A_W are, respectively, the average diameter of coil and the cross-sectional area of the coil wire.[60] And $N = F \cdot \frac{A_C}{A_W}$, is composed by: F=Filling factor, A_C and A_W cross-sectional coil area of coil and wire.

The peak output power is proportional to the square of the magnetic flux density B_r and the effective volume of the coil (i.e. $D_c A_c$). Therefore, we can increase the power generated or by increasing the magnetic flux density or increasing the size of the coil. In other words, to increase the power we must optimize the geometry of the magnets (i.e. increase B_r) and/or the geometry of the coils; we have done both studies to reach the best solution possible.

5.5 Final considerations

In this chapter we have introduced two models of passive ECD, which are therefore not able to recover energy, and a regenerative one. This type of study, even if not directly functional to ours, is necessary because the primary function of a shock absorber is to suppress vibrations and the right relationship between comfort/handling. First of all, it is necessary to make the ECD feasible for classic use and then analyse it for regenerative purpose.

Moreover, it must also be said that it was necessary to explain the Ebrahimi models in relative detail as they are our starting point.

As just said, starting from Ebrahimi's models and from the knowledge obtained through the latter's study we have modelled a damper that has an energy harvesting capability.

The model consists of two parts: a slider and a stator. In the latter there are the windings that “receive” the magnetic field and convert it into current, whole surrounded by a casing cylinder. On the other hand, in the former there are Permanent Magnets (PMs) alternated by Iron Poles and a rod that permits the move of the system. That model will be analysed deeper in Chapter 6.

Chapter 6

Project Development and Results

6.1 Introduction

Starting from the knowledge of Chapter 4 and 5 and we have built an Electromagnetic Energy Harvester Damper. This system converts the vibration of the vehicle body into electrical energy, where the motional electromotive force (emf) is induced in coils due to the relative motion of stator and slider.

6.2 Project

6.2.1 Introduction

The model geometry, following the Finite Element modelling rules, must be the easiest possible; in fact, every singularity (ex. chamfers) can make the model not convergent. For that reason, we have been worked in 2D-axialsymmetric. That dimension is sufficient for have a robust solution thanks to the tubular shape of our model.
In the implementation all the parts were introduced with simple elements (=rectangle) with all the dimensions parametrized to have more flexibility in the tuning that has been done later to obtain the optimum of the model. figure 56 shows our model geometry.

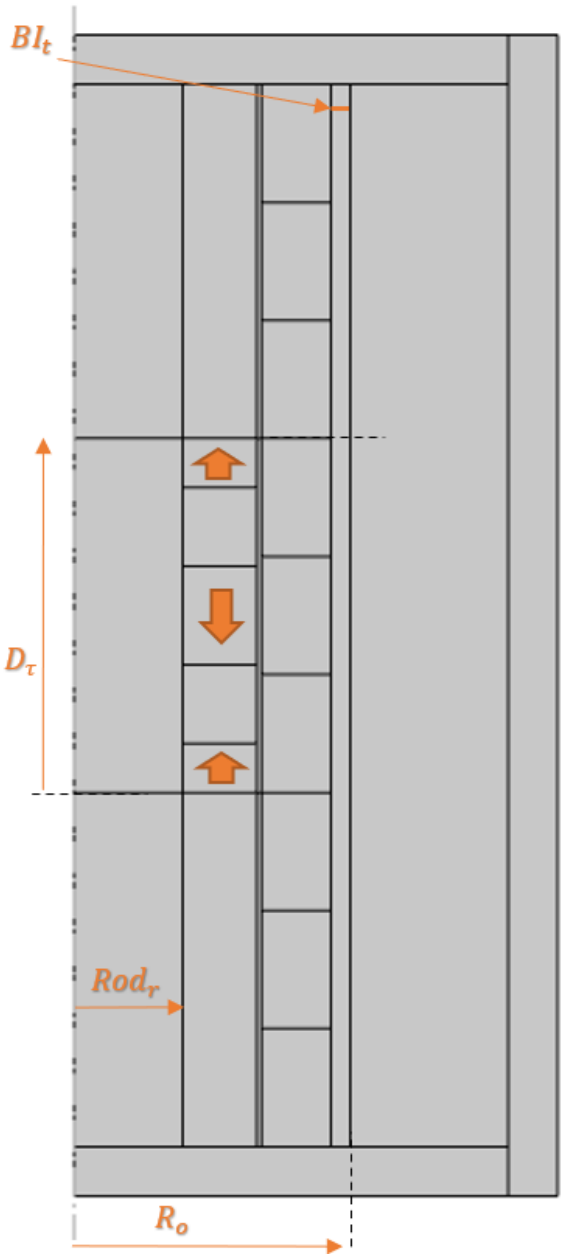

Parameter (radial)	Symbol
Rod radius	Rod_r
External radius	R_o
Coil Internal radius	C_{r_i}
Coil External radius	C_{r_o}
Air Gap	A_g
Back-Iron thickness	BI_t

Parameter (axial)	Symbol
Pole Pitch	τ
Double Pole Pitch	D_τ
Magnet Height	τ_m
Iron Pole Height	IP_h
Coil Height	C_h
PM North	⇧
PM South	⇩

Figure 56: Initial model geometry

The first model, the one showed in figure 56, has been dimensioned starting from some restrictions imposed and assumptions dictated by the bibliographic study.

In detail, we have the external radius (R_O) of the tube, the rod radius (Rod_r) and the back-iron width imposed by the shock absorber already present in the laboratory. Moreover, also the height (D_τ = Double Pole Pitch) is imposed by the dimensions of the suspension housing of our vehicle.

6.2.2 Starting sizes

Starting the analysis with radial dimensions we can said that external radius R_O, rod radius (Rod_r) and back-iron thickness (BI_t) are imposed.
As for the dimensions dictated by the bibliography, we started by choosing the radial ones; in particular $A_g = 0.5\ mm$ dictated by manufacturing restrictions.[59]

So, the last two radial dimensions to set are the magnet width and the coil width.

We are now going to focus on axial dimensions.
We have a pole pitch (τ) imposed by geometrical constraint, but being the minimum model of two poles its total height will be $D_\tau = 2 \cdot \tau$.
Pole pitch (τ) relates the two main axial dimension, the magnet height (M_h) and the iron pole height (IP_h); so, we just needed to find τ to complete the analysis.

Firstly, we must specify that we have worked with the model reduced to its minimum in order (as we can see in figure 56) to reduce the COMSOL Multiphysics software calculation time, which is necessary because the analysis in multiphysics has many variables and if not done on a simplified model it leads to a geometric complication and a timing of study not congruent with that of the development of a prototype.

Said that, looking again figure 56, the minimum of our model is composed by two PMs (one magnetized N and the other S) and therefore by two Iron Poles in the mover side, while it is composed by three groups of Coil in the stator side. This configuration allows us to take into account the complete physics, both for mover side (i.e., we have all the various configurations of magnets possible) and stator side (i.e., the groups of upper and lower Coils model well the necessary working area).

As already mentioned in chapter 4, we chose axial magnetization because it gives good results and does not present a lot difficulties in finding magnets on the market as it is instead for the axial ones.

Speaking of quantities, we went to impose initially a ratio $\tau_m/\tau = 0.55$ because it was observed to be the maximum flow configuration to reach the maximum damping factor.[59] This is not our goal, quite the opposite. But it is very interesting to see how the size of the components affects the behaviour of the output. For this reason, we started from the opposite condition, to have the widest possible spectrum of variation.

We can then, choosing a 3-phase system, imposing the three coils height equal, say that they are $C_h = D_\tau/3$.

The last sizes are rod height (Rod_h) and back-iron height (St_h) which are placed equal to the maximum height dictated by the other components (i.e., $Rod_h = St_h = D_{PP}$).

6.2.3 Working condition

The choice of the input function and, therefore, of the working frequency was dictated by the analysis of the operating condition of our shock absorber.
We know that a shock absorber in general has a response curve of the type in figure 57:

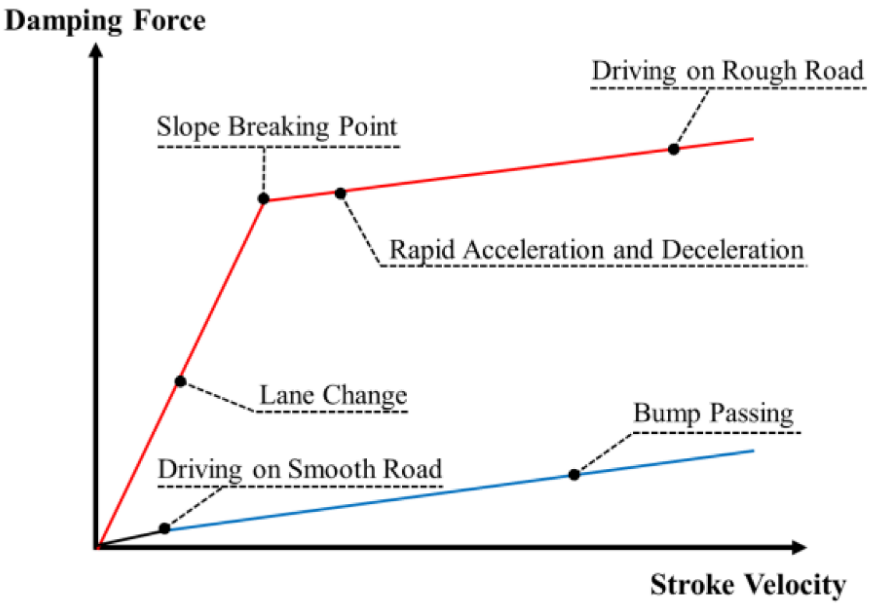

Figure 57: Optimal damping characteristics of the passive damper

From the figure 57 we can see that there are two main phases, the first, the low-speed phase (i.e., low frequency) in which the damping force increases in a linear way. In this case the shock absorber works in "passive" mode (i.e. damper aims are comfort and handling). Instead, when we are at high speed (i.e. high frequency) there is no increase in force and therefore there is no need to "damp"(i.e. the shock absorber, designed for the purpose of reducing vibrations to improve handling and comfort, does not work at this stage), in this situation the shock absorber works in an "hybrid" mode by converting vibrations into electricity (i.e. kinetic energy into electrical energy).

We can therefore conclude that our system will only work under conditions of high frequency, and therefore of low damping coefficient, due the road unevenness can be overcome with a low damping coefficient. So, all the vibrations that will be generated by the small asphalt roughness will be, at most, recovered.

To become familiar with some data we can see the figure 58

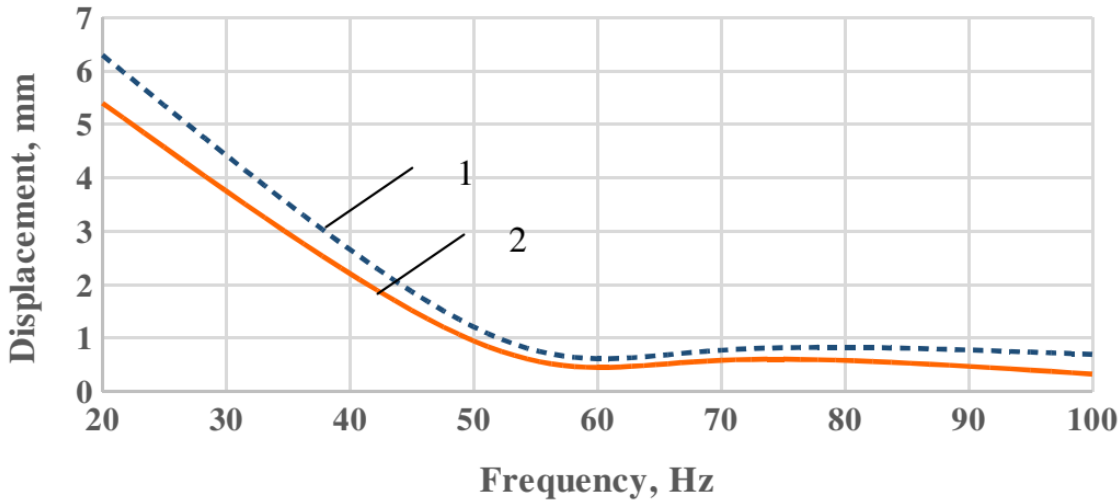

Figure 58: Displacements as function of frequency: 1 – relative displacement of shock absorber between the two mounting points, 2 – relative displacement between the piston rod and cylinder tube [62]

We can notice that in the frequency above 50 Hz the valve system in the shock absorber piston is not active. We can conclude that, seeing the very small displacement also for lower frequency, in the range up to 20 Hz the shock absorber as a fundamental role in damping the oscillations generated by the road unevenness.

Instead, high-frequency vibrations do not activate the shock absorber damping properties. The amplitudes are not big enough to create the necessary pressure drop between the two chambers above and under the piston and to provide viscous damping. This is the area of working of our system, from 20 Hz until 80 Hz.
We must remember that, as we can see in figure 58 above, the range frequency for a shock absorber, of any kind, is in the range 1 - 80 Hz. [62]

6.2.4 Input

Taking into account the assertions, above explained, about the Finite Element modelling rules of the Geometry paragraph and the ones of the working condition, we used a sinusoidal input function to have an input with constant and well-defined variation over time. This input function represents quite well what are the slight roughness of a common road.

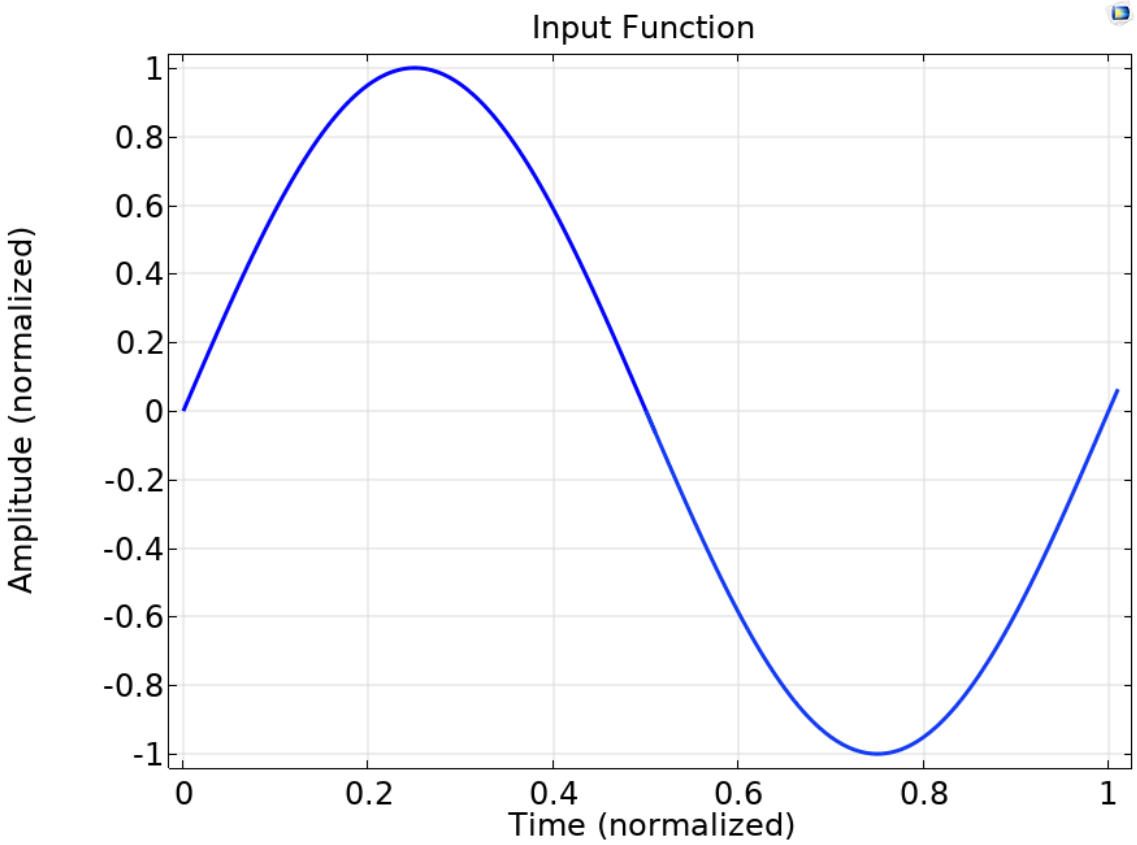

Figure 59: Input function of the system

So, talking about our modelling, we set initially a low frequency to made model converge. Only later, when the model is well placed, we raised to the desired one. In particular, we made some sweep analysis with changes in frequency (from 20 Hz to 80 Hz) to see how the system responds.
We will see in the final power optimization that analysis.

6.2.5 Kind of Studies

The analysis, as already seen in Chapters 4-5 and Appendix B, was based on the principles of electromagnetism. In particular, we went to study the magnetic field flux (B), the current density (J), the induced voltage (V) and output power (W).

We then modelled our system to obtain the maximum output power.

The physical modelling is completed by inserting an electrical circuit that allows us to evaluate the output power of the system (i.e., the power dissipated by the resistors connected to each coil).
These load resistances are modelled starting from the resistance of the coil and evaluating the relationship between load and coil resistance.

6.7 Results

6.7.1 Introduction

Starting from the analytical analysis already did in the chapter 5 we have built the models and compared the results with the first one to see if it is well posed.
Therefore, we made various simulation to optimize the model geometry, to see how much power produces with different excitations and, finally, we have made it feasible for magnetic materials properties.
We must also said that, in order to save computational time we made a quick analysis of the period to study. Easily we can say that, due the slider (i.e., central magnet) and the central coil are perfectly aligned at t=T/2, in order to analyse our system we should

always refer to that time. This simulation time is sufficient to see the general trend, therefore, we will only simulate in the complete period once the model optimisation phase has been completed.

6.7.2 Single Coil optimization

The first step for model sizing concerns the conductor. In fact, knowledge of the dimensions of the conductor, and therefore of the coils, is necessary for the modelling of the latter.
The height of the coil is imposed by geometrical constraint, in fact, due we have chosen three-phase coils we have: $C_h = D_\tau/3$. Therefore, we must find only the C_{r_i} that optimize the induced voltage. In general, as we said that our final model is 3-phase, the model used for the parameter optimization is a 1-phase model. This is just to save time in simulation.

To model the coil width we have performed a firstly sweep parametric analysis with coil internal radius (C_{r_i}) that varies from starting size value the minimum dictated by manufacturing restrictions. The first analysis is shown in figure 60

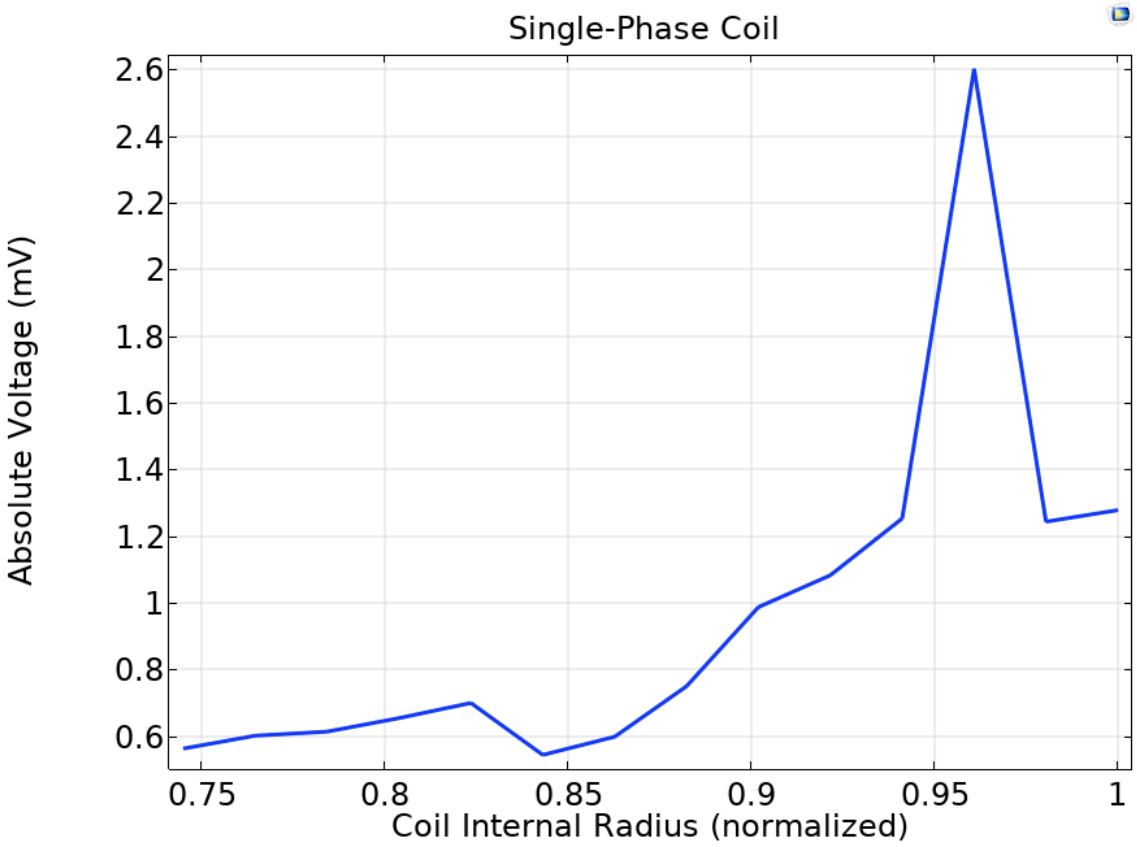

Figure 60: How Voltage Induced changes with Coil Internal radius, 0.5mm resolution

We notice that we have a peak that represent the optimum value, this is in interval $0.95 < C_{r_i}(norm) < 1$. So, it's necessary to make another sweep simulation with higher resolution around this values. The output is shown in figure 61

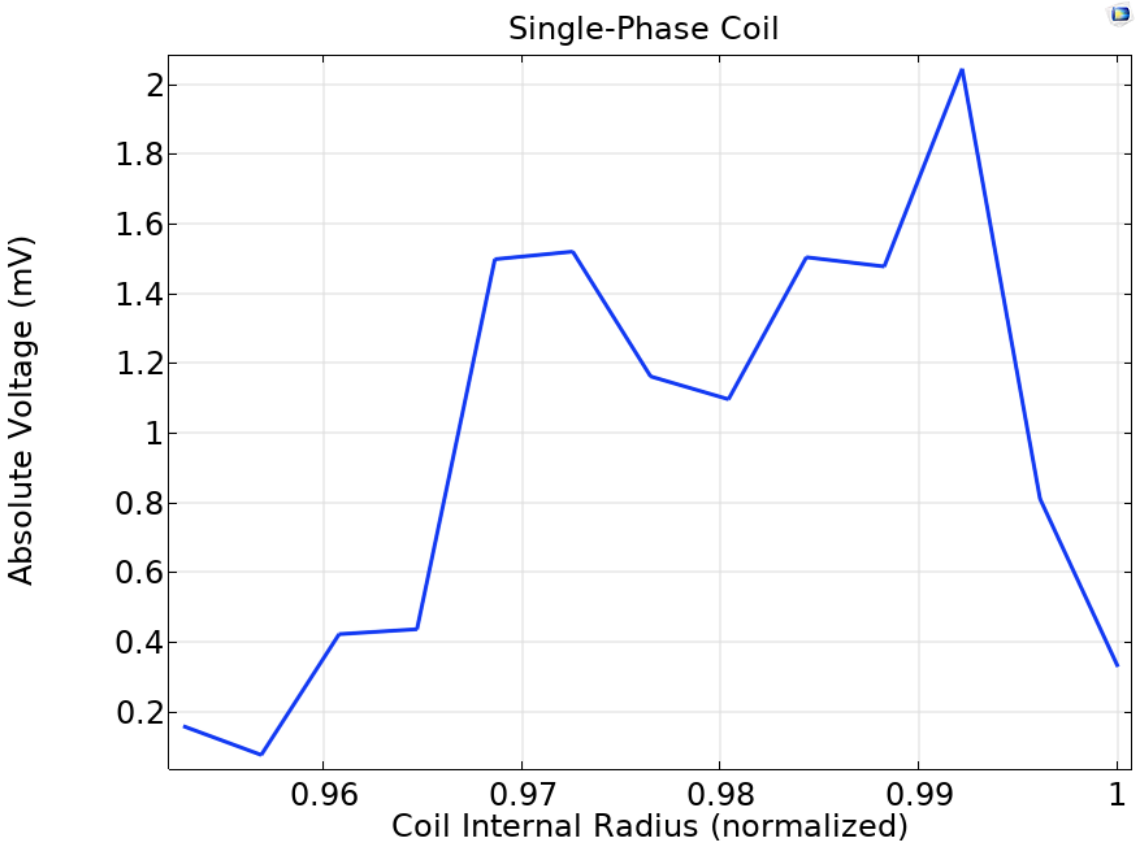

Figure 61: How Voltage Induced changes with Coil Internal Radius, 0.1mm resolution

As we can see the optimal value is for $C_{r_i}(norm) \approx 0.99$.

6.7.3 Magnet height optimization

Another geometrical parameter to optimize is the magnet height, and therefore, the iron pole height. In fact if we increase magnets height, we decrease the height of iron poles. That refers to the fact that the total height of the model is the Double Pole Pitch that is

$$D_\tau = 2 \cdot \tau = 2 \cdot (M_h + IP_h) \tag{6.1}$$

For this reason we have used the ratio τ_m/τ, that stays for the pole pitch (τ) over the magnet's thickness (τ_m), and is used to describe easily the relative variation of the two. Working again as for the others parameters, we have did a sweep analysis starting from

the minimum height of magnet taking into account the maximum one allowable by imposed dimension restrictions.

The sweep, starting from the configuration described above, increases the height of the magnet by the entire allowable range, and give us the output in figure 62

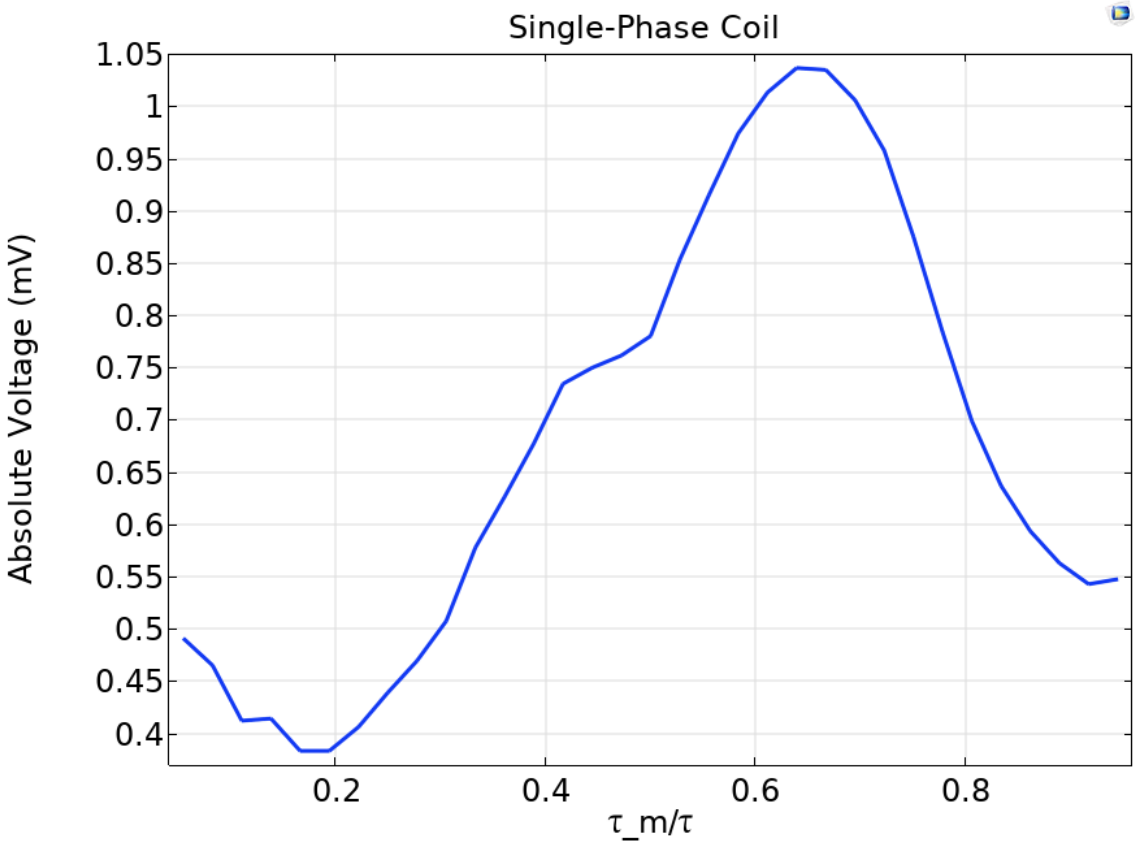

Figure 62: How Voltage Induced changes with tau_m/tau, resolution of 0.5 mm

We notice that we have a peak that represent the optimum value, this is in interval $0.6 < \tau_m/\tau < 0.8$. So, it's necessary to make another sweep simulation with higher resolution around that values.

The output is shown in figure 63

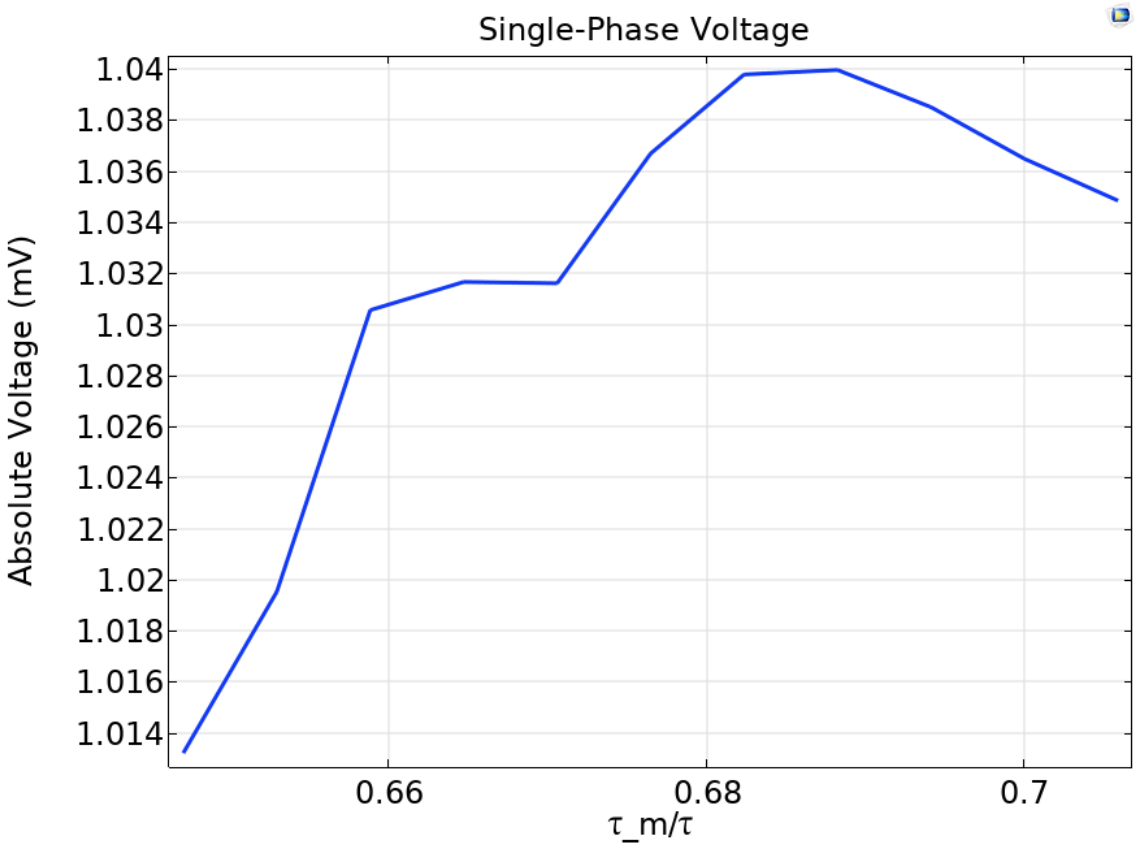

Figure 63: How Voltage Induced changes with tau$_m$/tau, resolution of 0.1mm

We can therefore deduce that the optimum height (i.e., the one that maximises the induced voltage, and so the power output) is $\tau_m/\tau = 0.69$

6.7.4 Multi-turn coil optimization

Knowing the general dimensions we can going to look for the parameters of the single coil.

We start with the number of ideally turns of a single coil with equation

$$N = F\frac{A_C}{A_W} = F\frac{4A_C}{\pi\phi^2} \tag{6.2}$$

where F=Fill factor (i.e. ratio of the area of electrical conductors to the provided winding space), A_w and ϕ are the diameter and the cross-sectional area of the wire.
So, the parameter that we need is the wire diameter of the coil (ϕ). We know that the coil wires are of standard sizes, that is the American wire gauge (AWG), also known as the Brown & Sharpe wire gauge. AWG is a logarithmic stepped standardized wire gauge system used since 1857, predominantly in North America, for the diameters of round, solid, nonferrous, electrically conducting wire.[63]
We choose the AWG from Zuo[38], that is AWG=30 (i.e., wire diameter = 0.254 mm). Chosen diameter of the wire and considering a fill-factor (F) = 0.9 (i.e. note that usually high fill-factor is greater than 0.5, which means that the test piece takes up one half or more of the area of the coil) we can calculate the number of ideally turns as:

$$N = F\frac{4A_C}{\pi\phi^2} \approx 274 \tag{6.3}$$

Finally we have calculated the resistance applying the equation

$$R_C = \rho\frac{L}{A} = \rho\frac{\pi\frac{\left(C_{r_i} + C_{r_o}\right)}{2}}{A_C} = 86.055 \cdot 10^{-6}\ \Omega \tag{6.4}$$

where C_{r_i} and C_{r_o}, A_C are, respectively, the outer and inner radius and the cross-sectional areas of coils.[38]
With that value we can later on optimize the load resistance (R_L) to obtain the maximum power output available.

6.7.5 Load resistance

Finally let's go to model the load resistance (R_{Load}), fundamental element to optimize due the power dissipated by this equals to the electrical power output of the system.

So, we have compared the load resistance with the coil ones.

Saying that $r = \frac{R_{Load}}{R_{Coil}}$ we went to analyse three different situations in:

$$r = 0.5$$

$$r = 1$$

$$r = 2$$

The Figure 64 shows the different power output values

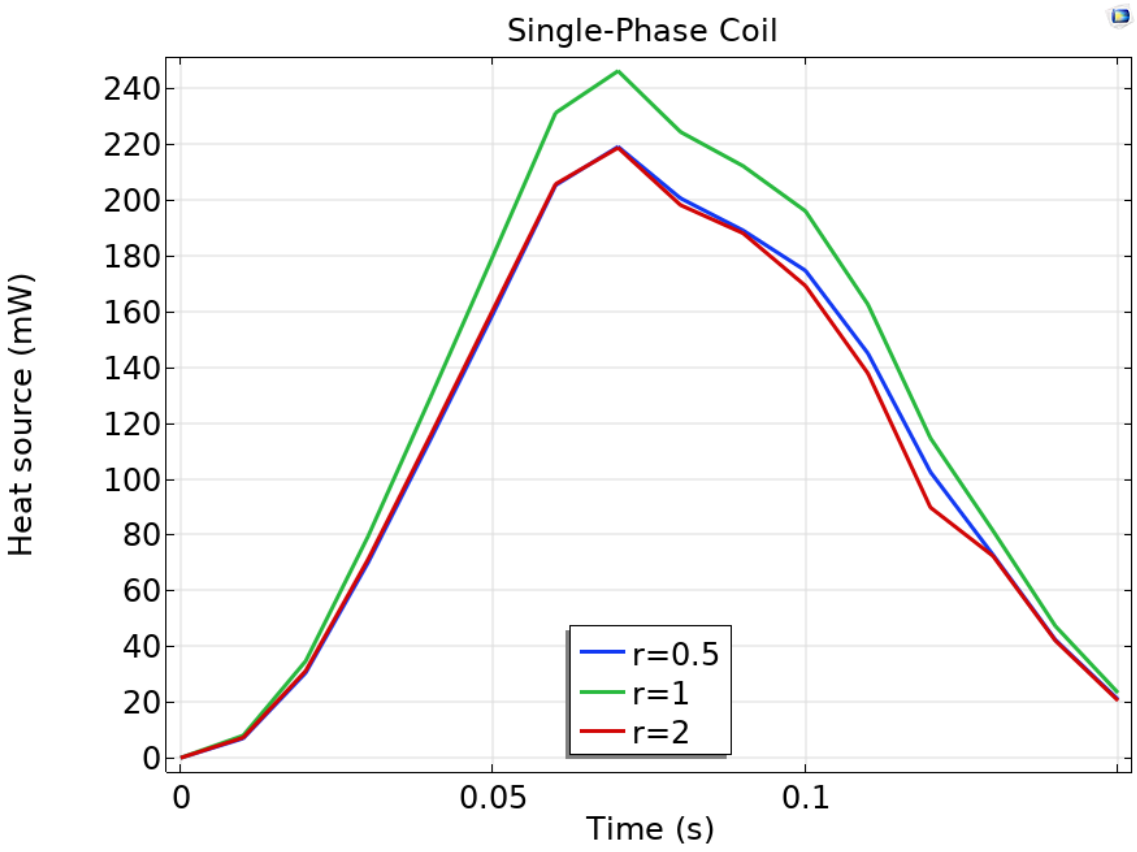

Figure 64: How power out change with load resistance

We can therefore deduce that the maximum power output occurs when we use

$$r = 1 \rightarrow R_{load} = R_{coil}$$

6.8 Optimized model simulation

6.8.1 Introduction

We have now optimised all the fundamental dimensions to build our Eddy Current Regenerative Damper.

We can then go to simulate the three-phase model with $f = 1\ Hz$ and analyse the results. The figures below show voltage induced and electrical power output respectively.

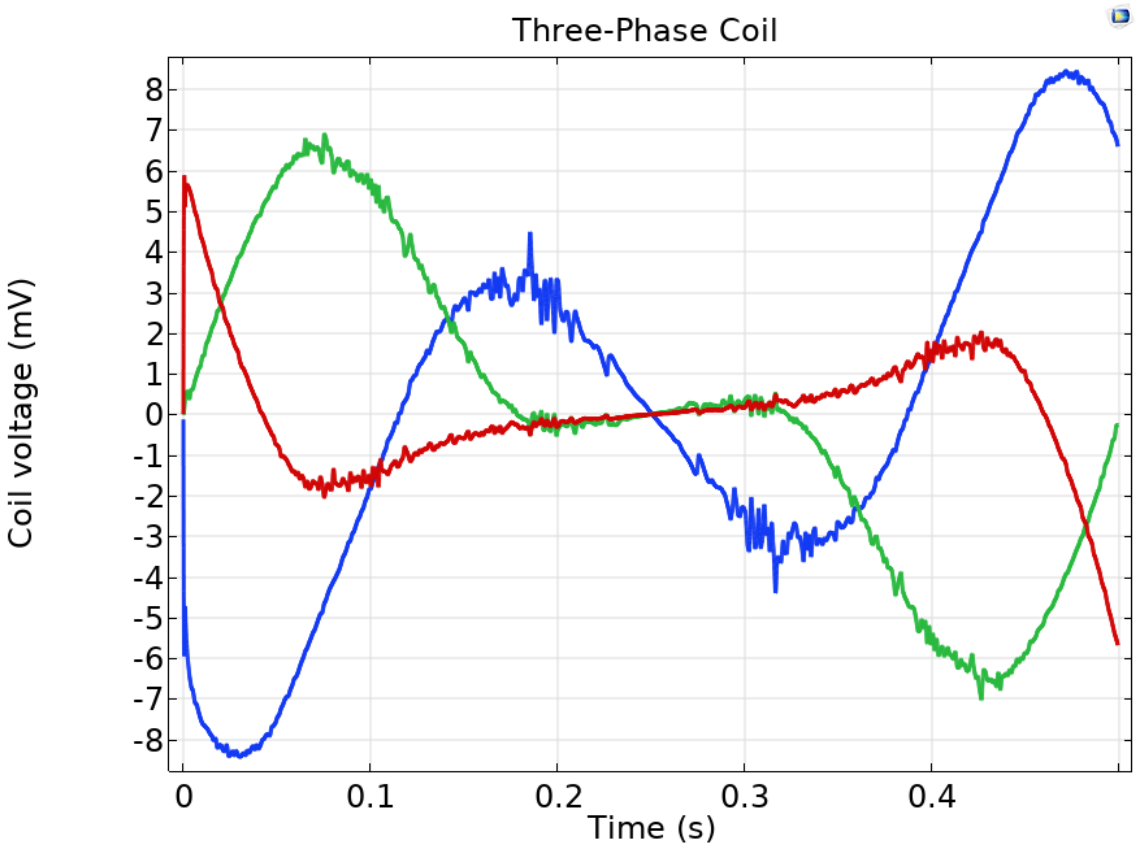

Figure 65: Three-phase coil voltage at 1Hz

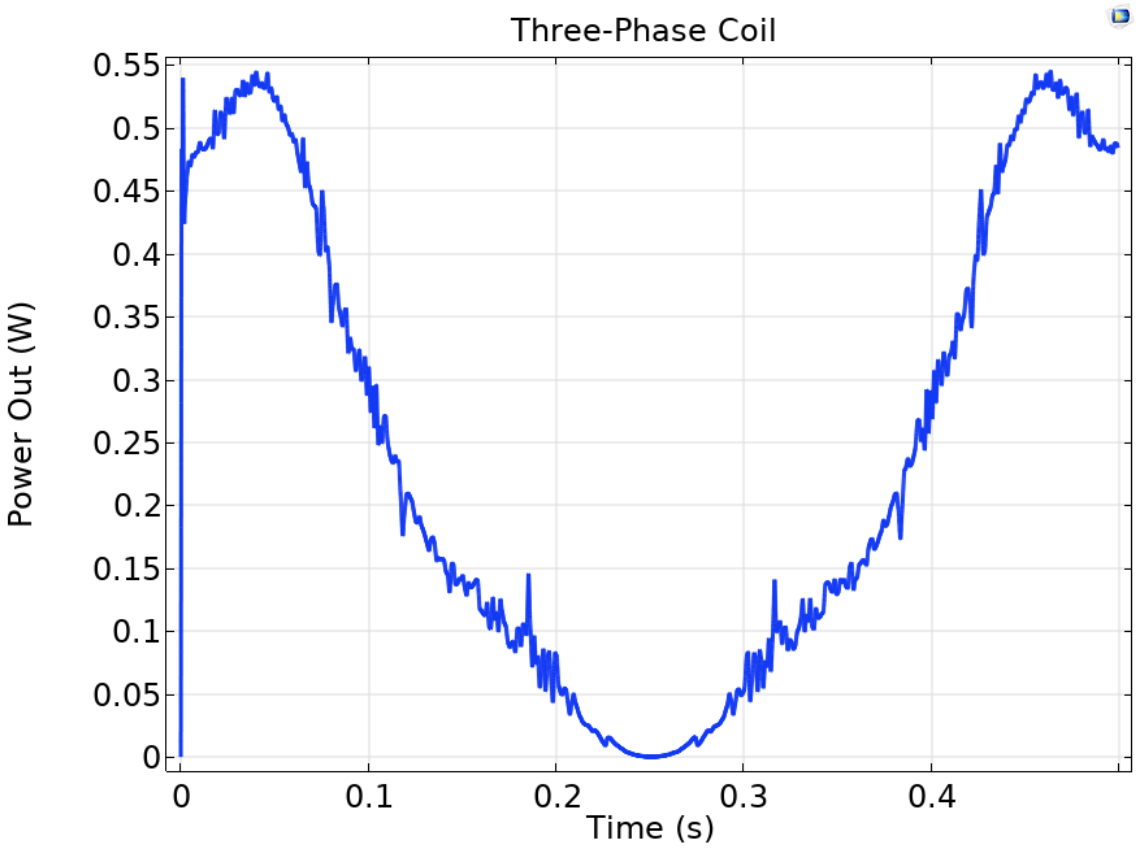

Figure 66: Three-phase coil power at 1Hz

The model is well posed and so we can made the frequency analysis.

6.8.2 Frequency analysis

Taking in consideration what we already said in the working conditions paragraph we have made a sweep analysis of $20\ Hz < f < 80\ Hz$ interval.

The figure 67 below shows the power outputs

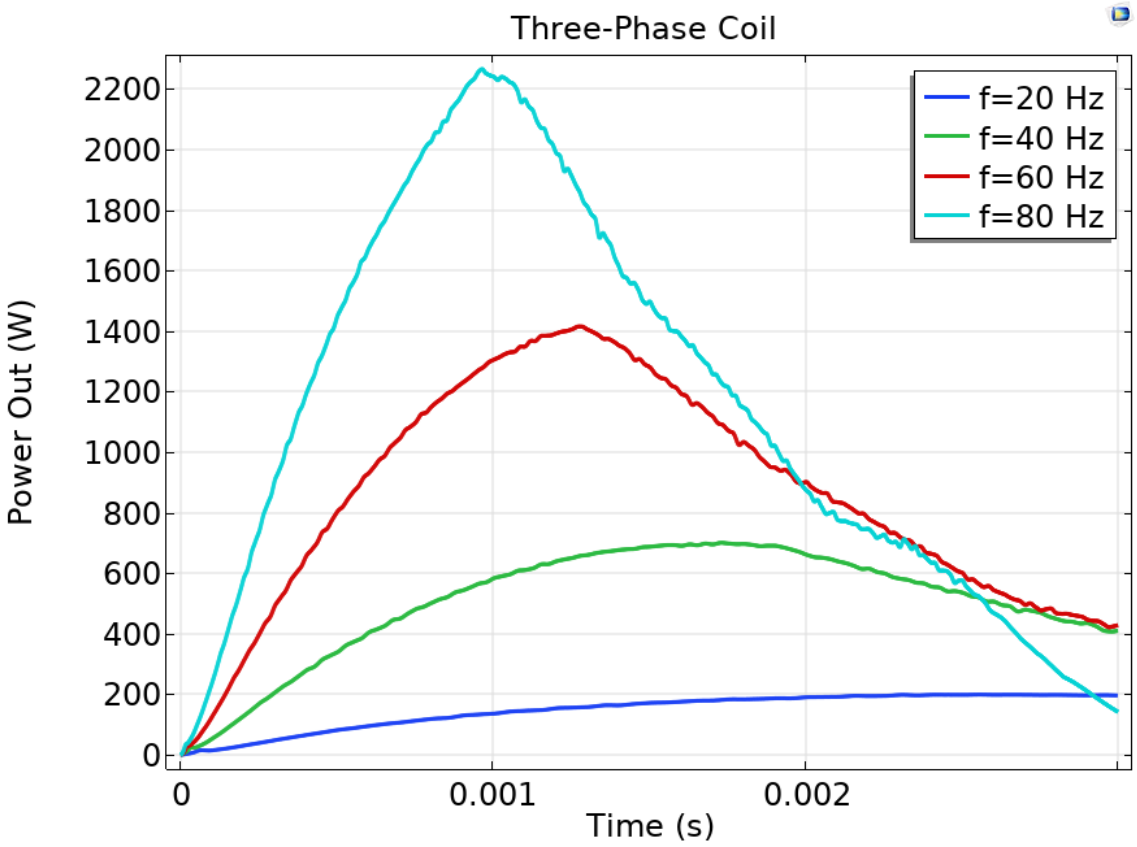

Figure 67: Three-phase power output for different frequencies

However, the one obtained is not the final model. In fact, we must make the model feasible also from the point of view of the materials used.

6.8.2 Material feasibility

Referring to materials chapter (i.e., Chapter 3) we know that all magnetic materials (soft and hard) experience the saturation when a strong magnetic flux density is applied. From the ARMCO datasheet (explained deeply in chapter 3) we know that the B_r which our iron poles saturate is $B_r = 2.15T$.

So, to make the system feasible, we need to see where the iron poles goes on saturation. The result is shown in figure 68

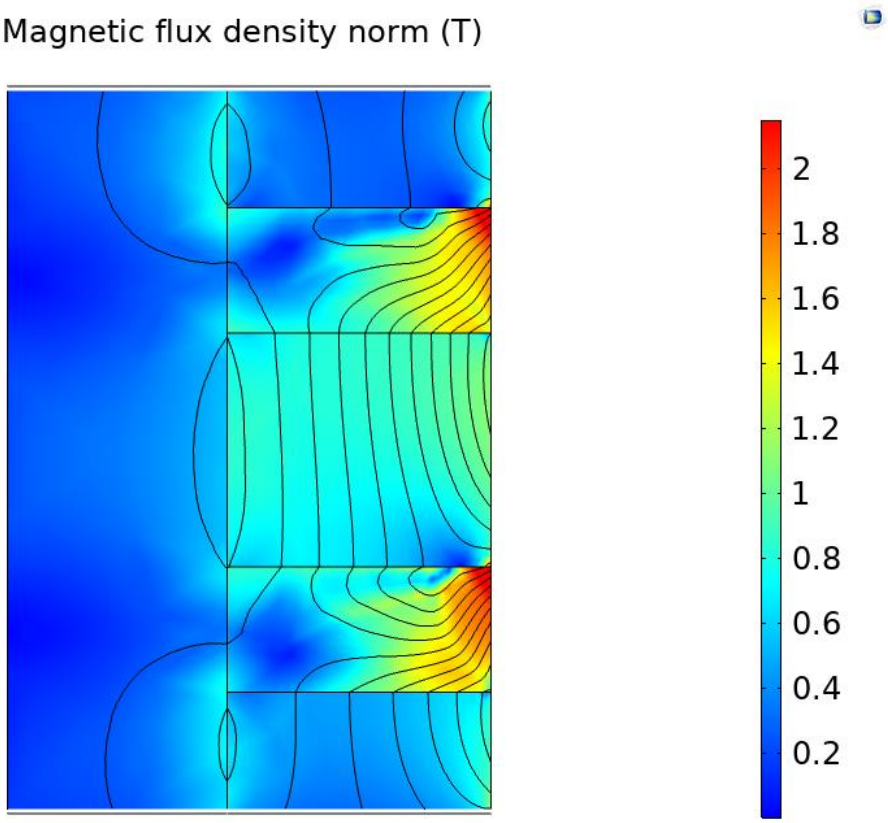

Figure 68: Magnetic flux density with optimized geometry model

As we can see only the corner of the iron poles is in saturation so we could choose higher iron poles to stay in safety conditions (i.e., we must reduce the magnets height). Starting again a new sweep simulation we are going to choose the one that will give us maximum electrical output power without saturating the iron poles. The figure is

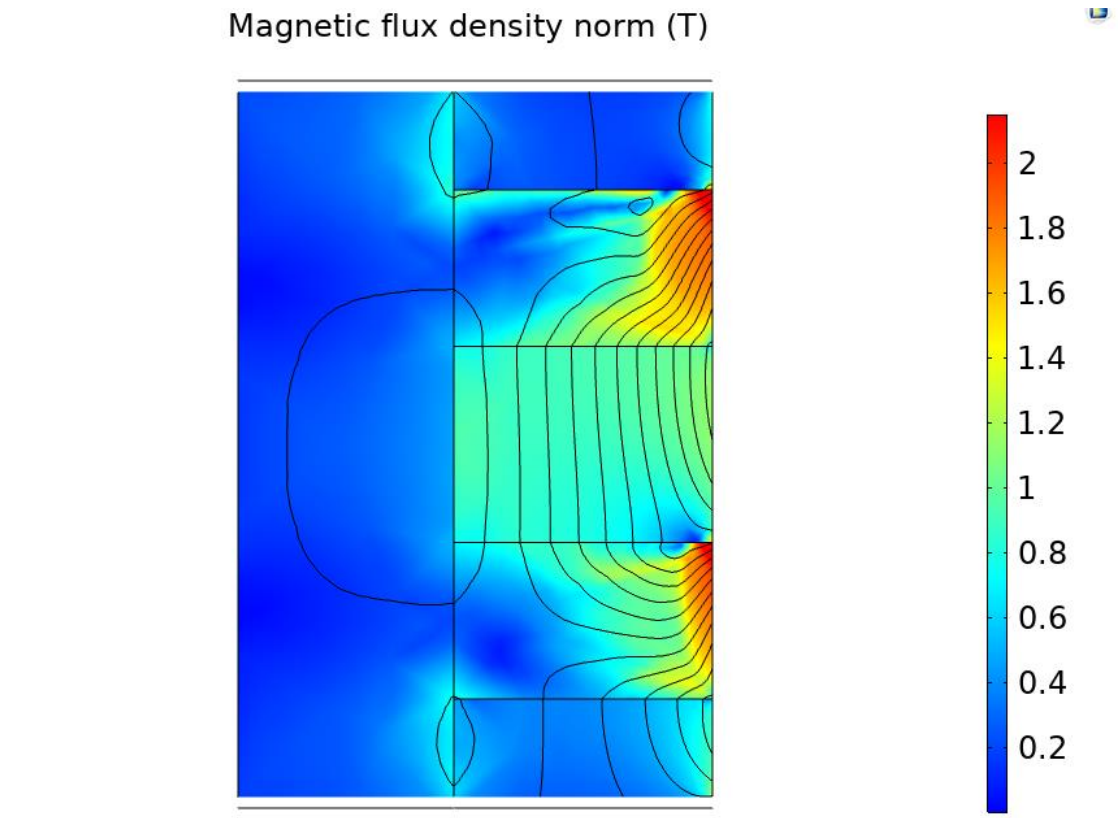

Figure 69: Magnetic flux density with optimized geometry model and material feasibility

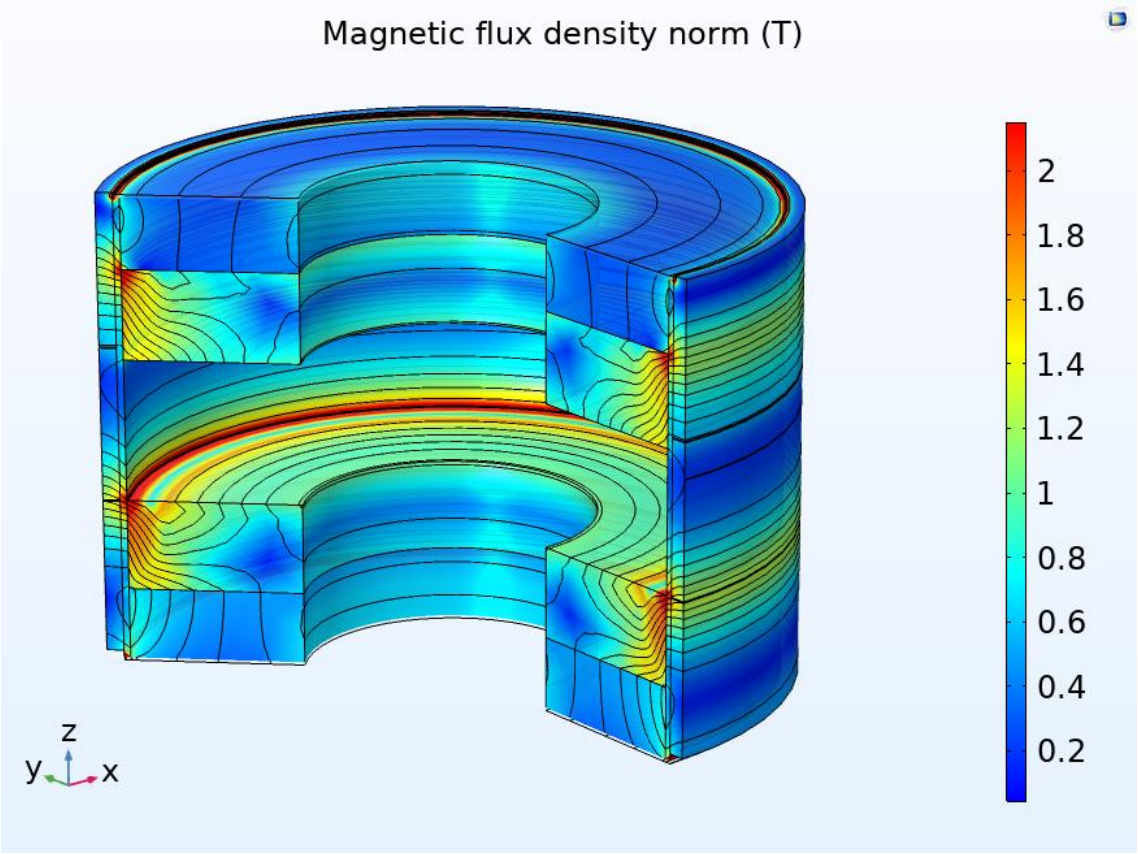

Figure 70: Magnetic flux density with optimized geometry model and material feasibility

Now, as we can see, the saturation areas (i.e., the bright red ones) is limited only in the corner in a very small area.

We can therefore say that the model is feasible also from the material point of view.

The final power output is

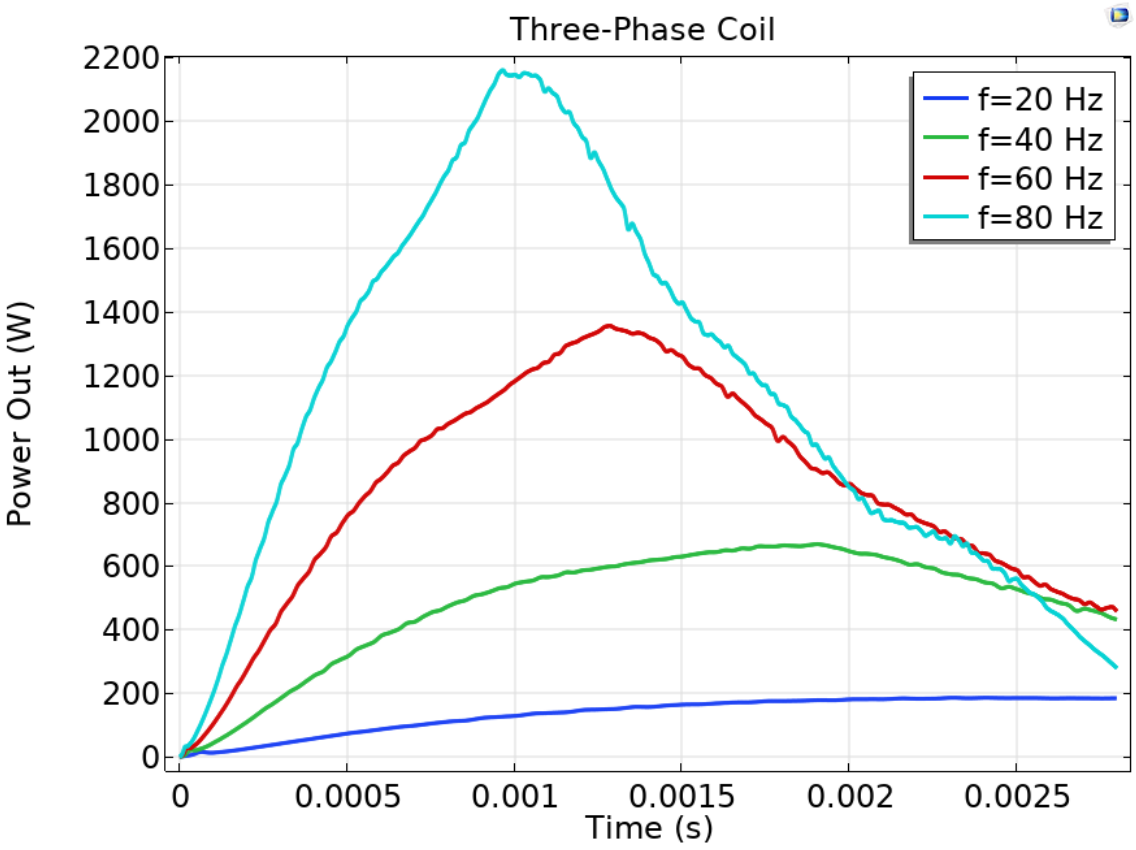

Figure 71: Three-phase power output for different frequencies

That, as we can see, is a little bit lower than the previous one but, anyway, gives very good output.

Chapter 7

Conclusions

During the development of this project I had to deal with topics and methodologies never seen before. This, especially at the beginning, has been a difficult challenge to overcome but it has led me to gain good knowledge in an area of great interest for me. In particular when we confronted ourselves with the first sketches we immediately understood that the development of the correct model design took a long time and many of these because the world of linear generators is very vast and complicated and all aspects, and the various types, had to be analysed carefully. Moreover, as we had geometrical, design and economic restrictions, the difficulty increased because we had to find the optimum even though we did not have the freedom to choose what, from an analytical point of view, made the most. These difficulties have emerged because at the state of the art, especially in our area, there are few studies carried out on this kind of generators. This, although from a design point of view is an additional difficulty, from an emotional point of view it is certainly a boost that has allowed us to work better.
I can, finally, say that I am very satisfied with my work and of the results obtained, also taking into account future developments, which we have already started to develop, that may be expanded in the next period.

7.1 Future Works

7.1.1 Air-gap

The air-gap is chosen from bibliography to respect construction restriction. That limitation regards anyway the lower bound, in fact, we can increase the Air-gap if we want.
As we can see from the figure XX the air-gap is in a very “saturation” area, maybe

Another aspects to analyse in the air-gap could be the insert of different kind of fluids instead air to improve the magnetic flux density.

7.1.2 Number of coil phases

Another aspect that can be optimized is the choice of the number of phases. We have used a three-phase generator but, as we can learn from Tang 2014[60], the power increase with the number of phase. So, it might be an interesting analysis to do. Below we can see some figures taken from Tang 2014 that shows that increment.

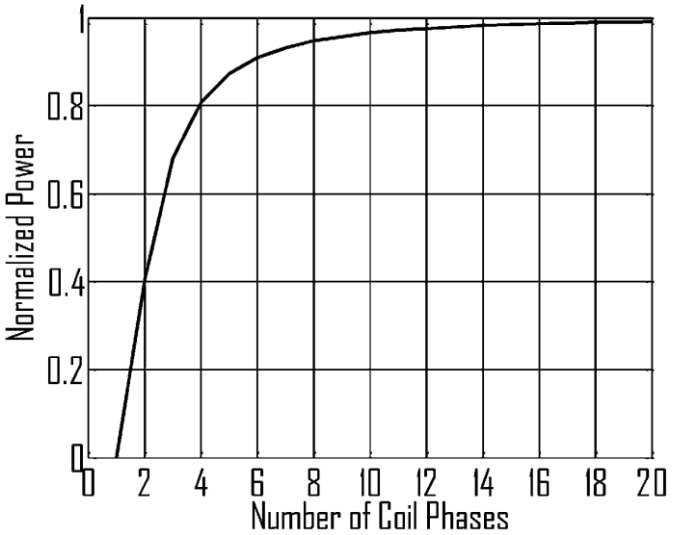

Figure 72: How power changes with Coil Phases[60]

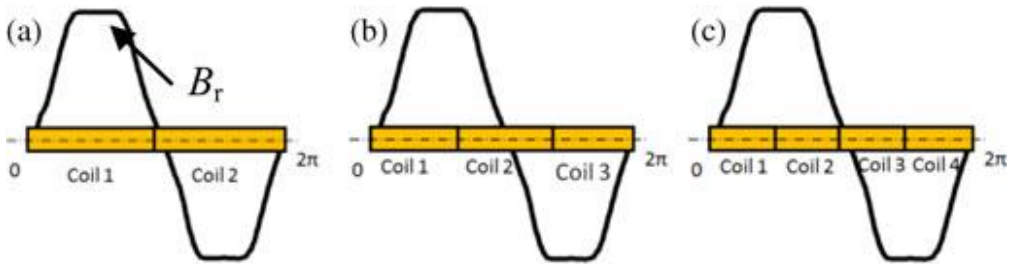

Figure 73: Coil design. (a) Two-phase coil. (b) Three-phase coil. (c) Four-phase coil[60]

7.1.3 Real size model

In our model, as we already said, we have worked with a minimal model (i.e., minimal configuration that contains all the fundamental components).
This because we need to make a lot of simulations and these must be carried out in the shortest possible time. Consider that the last model takes 5/6hr for each parameters changed in Lab PC.

A future work could be draw a new more realistic model (i.e., with dimension comparable to the produced one) and make some simulations to see if the simplified ones are feasible and how much power the whole system produce.
As we have seen, comparing the compact with a real ECD height, triple the model presented can give very good results.

7.1.4 Alternative design implementations

Another way to increment the power output of the might be to not only change the pole pitch, but also insert, in the same height, more or less number of poles. Taking again in consideration the equation for the power generation and the general behavior that we have seen we can say that to have max damping, you may need high number of magnets and iron poles with smaller height, and vice versa for power generation

7.1.5 Thermal analysis

Once we obtained a good electromagnetic model, we could also introduce the study of heat transfer. In this way we went to analyse the heat generated in the conductor by the eddy current (i.e., Joule Effect) and how it is dissipated by the other components of the system.
The thermal analysis is needed to study if the range of temperature are acceptable for the system and allows us to also make the electromagnetic study more faithful because we take into account the demagnetization due to the temperature variation. From the

equation we can notice that both B_r and H_c decrease as the magnet temperature increases, i.e.,

$$B_r = B_{r20}\left[1 + \frac{\alpha_B}{100}(\vartheta_{PM} - 20)\right] \tag{6.5}$$

$$H_c = H_{c20}\left[1 + \frac{\alpha_H}{100}(\vartheta_{PM} - 20)\right] \tag{6.6}$$

where ϑ_{PM} is the temperature of the PM, B_{r20} and H_{c20} are the remanent magnetic flux density and coercive force at 20°C, respectively, and $\alpha_B < 0$ and $\alpha_H < 0$ are temperature coefficients for B_r and H_c in %/°C, respectively.[12]

Appendix A

Air Pollution and Global Warming

A.1 Air Pollution

"At present, all vehicles rely on the combustion of hydrocarbon fuels to derive the energy necessary for their propulsion. Ideally, the combustion of a hydrocarbon yields only carbon dioxide and water, which do not harm the environment. Indeed, green plants "digest" carbon dioxide by photosynthesis. Carbon dioxide is a necessary ingredient in vegetal life. Animals do not suffer from breathing carbon dioxide unless its con- centration in air is such that oxygen is almost absent. Actually, the combustion of hydrocarbon fuel in combustion engines is never ideal. Besides carbon dioxide and water, the combustion products contain a certain amount of nitrogen oxides (NOx), carbon monoxides (CO), and unburned hydrocarbons (HC), all of which are toxic to human health."[23]

A.2 Global Warming

"Global warming is a result of the "greenhouse effect" induced by the presence of carbon dioxide and other gases, such as methane, in the atmosphere. These gases trap the Sun's infrared radiation reflected by the ground, thus retaining the energy in the atmosphere and increasing the temperature. An increased Earth temperature results in major ecological damages to its ecosystems and in many natural disasters that affect human populations. Among the ecological damages induced by global warming, the disappearance of some endangered species is a concern because it destabilizes the natural resources that feed some populations. There are also concerns about the migration of some species from warm seas to previously colder northern seas, where they can potentially destroy indigenous species and the economies that live off those

species. This may be happening in the Mediterranean Sea, where barracudas from the Red Sea have been observed. Natural disasters command our attention more than ecological disasters because of the amplitude of the damage they cause. Global warming is believed to have induced meteorological phenomena such as "El Niño," which disturbs the South-Pacific region and regularly causes tornadoes, inundations, and dryness. The melting of the polar icecaps, another major result of global warming, raises the sea level and can cause the permanent inundation of coastal regions, and sometimes of entire countries. Carbon dioxide is the result of the combustion of hydrocarbons and coal. Transportation accounts for a large share (32% from 1980 to 1999) of carbon dioxide emissions. The distribution of carbon dioxide emissions is shown in Figure 1.1. Figure 1.2 shows the trend in carbon dioxide emissions. The transportation sector is clearly now the major contributor of carbon dioxide emissions. It should be noted that developing countries are rapidly increasing their transportation sector, and these countries represent a very large share of the world's population. Further discussion is provided in the next subsection. The large amounts of carbon dioxide released in the atmosphere by human activities are believed to be largely responsible for the increase in global Earth temperature observed during recent decades (Figure 1.3). It is important to note that carbon dioxide is indeed digested by plants and sequestrated by the oceans in the form of carbonates. However, these natural assimilation processes are limited and cannot assimilate all of the emitted carbon dioxide, resulting in an accumulation of carbon dioxide in the atmosphere. In the last years, in a world where environmental protection and energy conservation are growing, the research and development activities related to transportation have emphasized the development of high efficiency, clean and safe transportation. The development of Electric Vehicle (EV) has therefore become of great interests, in fact, EVs can provide emission-free urban transportation, even considering emission from power plants we have a significantly reduction of air pollution due the utilization of different kinds of renewable energies."[23]

Appendix B

Review of Electromagnetism

B.1 Maxwell's Equations

Electromagnetic fields are governed by Maxwell's equations, where the main parameters are divided in fields and source terms.

The field: magnetic field intensity (*H)*, magnetic flux density (*B*), Electric field intensity (*E*) and Electric flux density (D) are the fields.

The source terms are: current density (*J*) and volume charge density ρ.

The Maxwell's equations are:

$$\nabla \times \boldsymbol{H} = \boldsymbol{J} + \frac{\partial \boldsymbol{D}}{\partial t} \tag{B.1}$$

$$\nabla \cdot \boldsymbol{B} = 0 \tag{B.2}$$

$$\nabla \times \boldsymbol{E} = -\frac{\partial \boldsymbol{B}}{\partial t} \tag{B.3}$$

$$\nabla \cdot \boldsymbol{D} = 0 \tag{B.4}$$

This system of equations, which are not all independent, represents a system of 12 unknown field components. For a complete theory of field equations, the additional constitutive equations must be added to Maxwell's equations as follows:

$$\boldsymbol{B} = \mu_0(\boldsymbol{H} + \boldsymbol{M}) \tag{B.5}$$

$$D = \varepsilon_0 \boldsymbol{E} + \boldsymbol{P} \tag{B.6}$$

and

$$\boldsymbol{J} = \sigma \boldsymbol{E} \tag{B.7}$$

where M is the magnetization, P is the polarization, μ_0, ε_0 and σ are the permeability, permittivity, and conductivity, respectively.

We can also express maxwell's equations in integral form taking the surface integral of the curl.

From the above equations we can apply the stokes theorem and the divergence theorem to find the result. This formulation represents the general form of the various laws from which maxwell has been derived.[40]

B.2 Potentials

"A vector potential and a scalar potential are vector fields, whose curl and negative gradient are a given vector field, respectively. Typically, it is more convenient to obtain the fields by using potential functions. Vector (A) and scalar potentials (φ) are used to convert Maxwell's four coupled, first order equations into two uncoupled second-order equations. The vector potential A is defined by"[40]
(B-2) as follows:

$$\nabla \cdot \boldsymbol{B} = 0 \rightarrow B = \nabla \times \boldsymbol{A} \tag{B.8}$$

The scalar potential φ is defined by (B-3) as

$$\nabla \times \left(\boldsymbol{E} + \frac{\partial \boldsymbol{A}}{\partial t} \right) = 0 \rightarrow \boldsymbol{E} + \frac{\partial \boldsymbol{A}}{\partial t} = -\nabla \varphi \tag{B.9}$$

If we substitute the found equations into the remaining two Maxwell equations (B-1, B-4), we found

$$\nabla^2 A - \mu\varepsilon \frac{\partial^2 A}{\partial t} = -\mu J \tag{B.10}$$

$$\nabla^2 \varphi - \mu\varepsilon \frac{\partial^2 \varphi}{\partial t^2} = -\frac{\rho}{\varepsilon} \tag{B.11}$$

By imposing the Lorenz gauge condition ($\nabla \cdot A = -\mu\varepsilon \frac{\delta \varphi}{\delta t}$), we can found the final equations as

$$\nabla^2 A - \mu\varepsilon \frac{\delta^2 \boldsymbol{A}}{\delta t^2} = -\mu \boldsymbol{J} \tag{B.12}$$

$$\nabla^2 \varphi - \mu\varepsilon \frac{\delta^2 \varphi}{\delta t^2} = -\frac{\rho}{\varepsilon} \tag{B.13}$$

Due Maxwell's equations regards the whole electromagnetic applications, which are categorized as high frequency, quasi-static, and static. Therefore, we must analyse only the one that governs the eddy current phenomena, that is the quasi-static.

In the quasi-static we approximate ignoring the displacement current term $\partial D / \partial t$ in (B-1). The potential equations are reduced to Poisson's equations,

$$\nabla^2 \boldsymbol{A} = -\mu \boldsymbol{J} \tag{B.14}$$

$$\nabla^2 \varphi = -\frac{\rho}{\varepsilon} \tag{B.15}$$

Finally, we could found the solution to the equation above using Green's function for operator ∇^2, as

$$A(x,t) = \frac{\mu_0}{4\pi} \int_{\Gamma} \frac{\boldsymbol{J}(x',t)}{|\boldsymbol{x} - \boldsymbol{x}'|} d\Gamma' \tag{B.16}$$

and

$$\varphi(x,t) = \frac{1}{4\pi\varepsilon_0} \int_{\Gamma} \frac{\rho(\boldsymbol{x}',t)}{|\boldsymbol{x} - \boldsymbol{x}'|} d\Gamma' \tag{B.17}$$

where $\boldsymbol{x}$ is the observation point, and $\boldsymbol{x'}$ is the source point.

"The static-field theory is also applied to a variety of applications such as permanent magnet structures, and direct current devices. In the static-field theory, both time-dependent terms are ignored ($\frac{\delta \boldsymbol{D}}{\delta t} = \frac{\delta \boldsymbol{B}}{\delta t} = 0$). The solutions of the potential equations are similar to those in the quasistatic case, unless the scalar and vector potentials are not time dependent."[40]

B.3 Magnetic Field Analysis

Once $\boldsymbol{A}$ is determined by calculating (B-16), the magnetic flux density $\boldsymbol{B}$ can be computed by using $\boldsymbol{B} = \nabla \times \boldsymbol{A}$, **that** applied for surface currents, give

$$B(x,t) = \frac{\mu}{4\pi}\int \frac{\boldsymbol{j}(\boldsymbol{x}',t)\times(\boldsymbol{x}-\boldsymbol{x}')}{|\boldsymbol{x}-\boldsymbol{x}'|^{\boldsymbol{3}}}ds' \tag{B.18}$$

where j (A/m) is the surface current density.

"There are a number of approaches for calculating the magnetic field of a permanent magnet. The simplest approach is the dipole moment model that is appropriate for the field calculation at long distances from the magnet, compared with the magnet diameter. The charge method and the current method model the magnet with a distribution of the charge and current, respectively."[40]

B.4 The Current Model (Magnetic Flux Calculation)

In the current model, the magnet is expressed as the distribution of the equivalent current, which is used as a source term in the magnetostatic field equations. By substituting (B-8) into (B-1), and imposing the Coulomb Gauge ($\nabla \boldsymbol{A} = 0$),

$$\nabla^2 \boldsymbol{A} = -\mu_0(\boldsymbol{J} + \nabla \times \boldsymbol{M}) \tag{B.19}$$

(B-19) causes the definition of the magnetic volume current density $\boldsymbol{J}_m = \nabla \times \boldsymbol{M}$. If the magnetization M is restricted to a volume Γ, and falls to zero outside of Γ, (B-18) is reduced to

$$\boldsymbol{B}(x) = \frac{\mu}{4\pi}\int \frac{\boldsymbol{J_m}(\boldsymbol{x}')\times(\boldsymbol{x}-\boldsymbol{x}')}{|\boldsymbol{x}-\boldsymbol{x}'|^{\boldsymbol{3}}}d\Gamma + \frac{\mu}{4\pi}\int \frac{\boldsymbol{j_m}(\boldsymbol{x}')\times(\boldsymbol{x}-\boldsymbol{x}')}{|\boldsymbol{x}-\boldsymbol{x}'|^{\boldsymbol{3}}}ds \tag{B.20}$$

Where J_m and j_m are equivalent volume and surface current densities and defined by:

$$\boldsymbol{J_m} = \nabla \times \boldsymbol{M} \left(\frac{A}{m^2}\right) \quad Volume\ current\ density \tag{B.21}$$

$$\boldsymbol{j_m} = \mathbf{M} \times \hat{\boldsymbol{n}} \left(\frac{A}{m}\right) \quad Surface\ current\ density \tag{B.22}$$

where $\hat{\boldsymbol{n}}$ is the outward unit normal to the surface.

By assuming that a cylindrical magnet is polarized along its z-axis with a uniform magnetization(*i.e.* $\boldsymbol{M} = M_s\hat{\boldsymbol{z}}$), as shown in figure B-1 , the volume and surface current densities are

$$\boldsymbol{J_m} = 0 \tag{B.23}$$

$$\boldsymbol{j_m} = \mathrm{M}\hat{\boldsymbol{\varphi}} \tag{B.24}$$

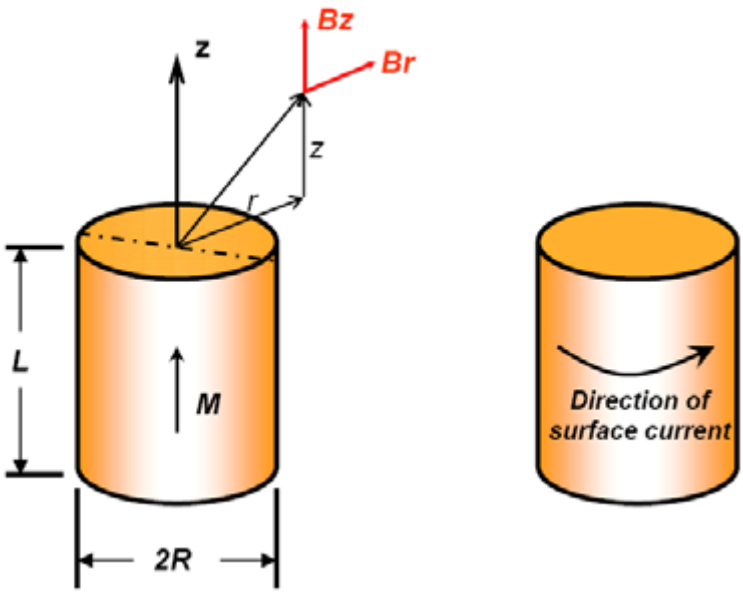

Figure B-74: Permanent magnet and its equivalent surface current density[40]

Appendix C
B-H curves in COMSOL

C.1 Introduction

The B-H curve is generally used to describe the nonlinear behavior of magnetization that a ferromagnetic material obtains in response to an applied magnetic field. In this blog post, we will show you how the B-H curve affects your magnetic analysis and how to improve it, using a demo application available as of version 5.5 of the COMSOL Multiphysics® software.

C.2 The B-H Curve, Permeability, and Differential Permeability

Magnetic soft iron steels are widely used as core materials in motors, transformers, and inductors. If they are placed in a region without magnetic fields, they will remain without a magnetic field; they do not have an "intrinsic" magnetization. The B-H curve is usually used to describe the magnetization properties of such materials by characterizing the permeability μ, which is defined as:

$$\mu = \frac{\mathbf{B}}{\mathbf{H}},$$

where $\mathbf{B}$ and $\mathbf{H}$ represent the magnetic flux density in tesla (T) and the magnetic field intensity in Ampère per meter (A/m), respectively.

COMSOL Multiphysics has more than 200 built-in materials with B-H curves. Specifically, the *Nonlinear Magnetic* material library covers most of the widely used nonlinear magnetic materials. COMSOL Multiphysics usually uses an interpolation function with a local table to define the B-H curve. You can also plug in your own B-H curves by adding the *B-H Curve* material property to a new magnetic material.

The B-H curve of a material can be measured in the laboratory by following standards and procedures. However, it is difficult to perform a direct measurement when $\mathbf{B}$ is above the saturation induction, which is referred to as the over fluxed region. Generally, it is difficult for test equipment to reach such a high level of stable $\mathbf{B}$; for instance, 1.8 T. Even if the test equipment can do so, the measured data will typically be inaccurate due to the test frame getting overheated. For this reason, the B-H curve data in the over fluxed region is usually obtained using extrapolation methods; for example, the simultaneous exponential extrapolation (SEE) method (Ref. 1).

From the numerical point of view, the slope of the B-H curve is of great importance, since the nonlinear iterative solver uses it to evaluate the local linearization of the nonlinear material behavior. Thus, it is more useful to consider the differential permeability or the incremental permeability, especially for nonlinear magnetic materials. The differential permeability is defined as:

$$\mu_D = \frac{d\mathbf{B}}{d\mathbf{H}},$$

For standard materials, μ_D is larger than 0, which implies that the B-H curve is monotonically increasing. For ferromagnetic materials, μ_D decreases to the permeability of vacuum μ_0 after magnetic saturation, as illustrated in the figure below.

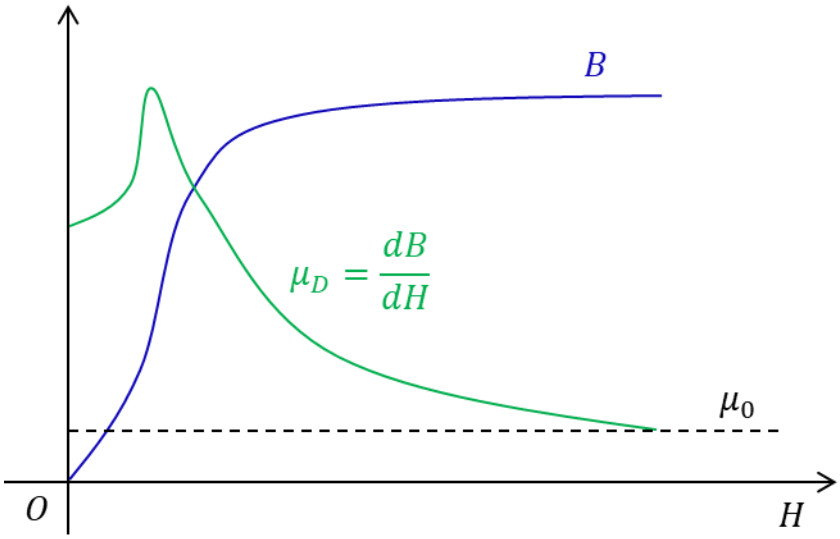

Figure 75: How the Extrapolation of the B-H Curve Affects the Simulation

In the *Settings* window of the *B-H Curve* interpolation function, you can click the *Plot* button to visualize the B-H curve. For a better visualization, the *Extrapolation* can be set to *Constant*. However, this setting is not recommended for the study, since otherwise, the B-H curve will have discontinuities at the start and end points of the B-H curve data.

To understand how the setting actually affects the simulation, let us take the E-Core Transformer tutorial model in the AC/DC Module Application Library as an example. It takes about two minutes when setting the B-H curve extrapolation to *Constant* and one minute when setting it to *Linear* for a time-dependent study from 0 to 0.05 s. The convergence plots of the two simulations explain the difference in computation time. As the figure below indicates, due to the discontinuities caused by the *Extrapolation* setting, it requires much smaller time steps to find a solution when the magnetization reaches saturation.

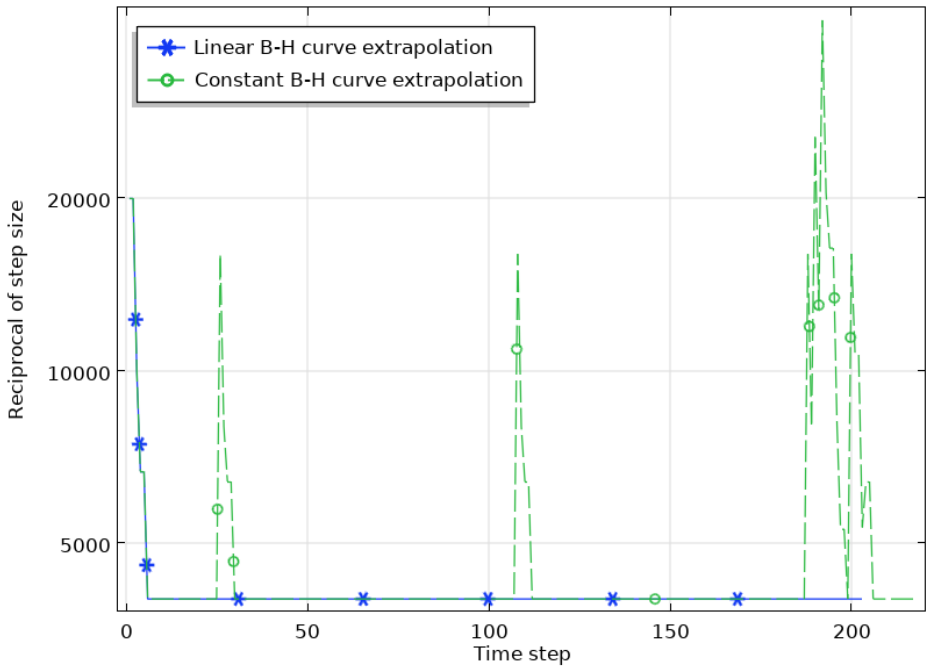

C.3 How the Smoothness of the B-H Curve Affects the Simulation

In addition to the issues of the extrapolation, the μ_D curve from measured B-H data may contain ripples that are generally unphysical. Such unphysical ripples cause numerical instabilities that result in longer computation times or even a lack of convergence. Take the E-Core Transformer model as an example again. The model uses the built-in *Soft Iron* material where the B-H curve is smooth. Now, we change the curve by modifying a few data points to make three new groups of B-H curves, as shown below. Let's run the time-dependent study in the model with these three B-H curves and all of the other settings the same. The simulation details are listed in the table below, and the convergence plots are shown in the figure below

Ringraziamenti

A conclusione di questo elaborato, desidero menzionare tutte le persone, senza le quali questo lavoro di tesi, ed in generale, il completamento della mia carriera universitaria, non sarebbe stato possibile.

Ringrazio il mio relatore Prof. Maizza Giovanni che in questo ultimo, difficile, anno di lavoro, ha saputo guidarmi, con suggerimenti pratici, nelle ricerche e nella progettazione del modello.

Ringrazio anche il mio co-relatore, e collega, Dr. Umid Jamolov, che ha contribuito con le sue idee e le sue intuizioni a portarmi a degli ottimi risultati finali.

Ringrazio di cuore Donatella, Silvano, Federica ed Erika per avermi sempre sostenuto, supportato, sopportato ed incoraggiato nei momenti più difficili aiutandomi a portare a termine questa, come tante altre, meravigliose esperienze.
Senza di loro questo risultato sicuramente non sarebbe stato possibile.

Ringrazio i miei amici più cari, con cui ho passato dei momenti bellissimi ed indimenticabili in questi anni di studi. Un grazie a Lorenzo, Paolo, Andrea, Giacomo, Luca e Riccardo.

Infine, vorrei dedicare questo traguardo a me stesso, che tra mille difficoltà ed esperienze diverse sono riuscito a portare a termine.
Che questo possa essere l'inizio di una lunga e brillante carriera professionale.

Stay Hungry, Stay Foolish!

Bibliography

1. Chan CC. 2 - The State of the Art of Electric Vehicles. *J Asian Electr Veh.* 2004;2(2):579-600. doi:10.4130/jaev.2.579

2. Abolhassani M, Acharya P, Asadi P, et al. Impact of hybrid electric vehicles on the world's petroleum consumption and supply. In: *SAE Technical Papers.* ; 2003. doi:10.4271/2003-01-2310

3. Hake JE. International energy outlook — 2000 with projection to 2020. Published online 2000.

4. Comsol. Detailed Explanation of the Finite Element Method. https://www.comsol.it/multiphysics/finite-element-method

5. Bastos JPA, Sadowski N. *Magnetic Materials and 3D Finite Element Modeling.*; 2013. doi:10.1201/b15558

6. BrainKart.com. Distinguish between ferromagnetic, paramagnetic and diamagnetic materials. http://www.brainkart.com/article/Distinguish-between-ferromagnetic,-paramagnetic-and-diamagnetic-materials_185/

7. Dall'Ora L. Analysis and Design of a Linear Tubular Electric Machine for Free - piston Stirling Micro - cogeneration Systems. Published online 2014:210.

8. Coolmagnetman. Twelve Fundamentals of Magnetism. https://www.coolmagnetman.com/magfund07.htm#:~:text=The B-H curve is the,a B of 1 mT

9. Tutorial E. Magnetic Hysteresis. https://www.electronics-tutorials.ws/electromagnetism/magnetic-hysteresis.html

10. NIMS. Types of Magnetic Material.

https://www.nims.go.jp/mmu/tutorials/soft&hard.html#:~:text=Since soft magnetic materials can,easily magnetized%2C permeability is high.&text=These materials are called hard,magnets and magnetic recording media.

11. Tom J. Kazmierski SB. *1 - Energy Harvesting Systems: Principles, Modeling and Applications*. Vol 53.; 2013.

12. Gieras JF, Piech ZJ, Tomczuk B. *Linear Synchronous Motors*.; 2018. doi:10.1201/b11105

13. Yu Y, Tauxe L, Moskowitz BM. Temperature dependence of magnetic hysteresis. *Geochemistry, Geophys Geosystems*. 2004;5(6). doi:10.1029/2003GC000685

14. Lederer D, Igarashi H, Kost A, Honma T. On the parameter identification and application of the Jiles-Atherton hysteresis model for numerical modelling of measured characteristics. *IEEE Trans Magn*. 1999;35(3 PART 1):1211-1214. doi:10.1109/20.767167

15. Jiles DC, Atherton DL. Theory of ferromagnetic hysteresis (invited). *J Appl Phys*. 1984;55(6):2115-2120. doi:10.1063/1.333582

16. Alliance LLC. NdFeB N-50. http://www.allianceorg.com/neodymium-magnets-n50.html

17. Aksu U, Halicioglu R. 0 - A review study on energy harvesting systems for vehicles. *Teh Glas*. 2018;12(4):251-259. doi:10.31803/tg-20180210153816

18. Lafarge B, Cagin S, Curea O, Perret AH. From functional analysis to energy harvesting system design: application to car suspension. *Int J Interact Des Manuf*. Published online 2016. doi:10.1007/s12008-015-0284-1

19. Williams CB, Yates RB. Analysis of a micro-electric generator for microsystems. *Sensors Actuators, A Phys*. Published online 1996. doi:10.1016/0924-

4247(96)80118-X

20. Anton SR, Sodano HA. A review of power harvesting using piezoelectric materials (2003-2006). *Smart Mater Struct.* Published online 2007. doi:10.1088/0964-1726/16/3/R01

21. Meninger S. A low power controller for a MEMS based energy converter. Published online 1999.

22. Gao Y, Ehsani M. Systematic design of fuel cell powered hybrid vehicle drive train. In: *SAE Technical Papers.* ; 2001. doi:10.4271/2001-01-2532

23. Ehsani M, Gao Y, Emadi A. *1 - Modern Electric, Hybrid Electric, and Fuel Cell Vehicles.*; 2017. doi:10.1201/9781420054002

24. Clegg SJ. A Review of Regenerative Braking Systems. *Inst Transp Stud Univ Leeds.* Published online 1996.

25. Pulkit Gupta, Anchal Kumar, Sandeepan Deb S. Regenerative Braking Systems (RBS) (Future Of Braking Systems). *Int J Mech Prod Eng.* Published online 2014.

26. Kalayarasan M IARS and BG. Torsion spring regenerative braking in automobile a conceptual idea. *Int J Appl Res.* Published online 2016.

27. II WWC. *Global Energy Innovation: Why America Must Lead.*; 2011.

28. Hampl J. Concept of the Mechanically Powered Gyrobus. *Trans Transp Sci.* Published online 2013. doi:10.2478/v10158-012-0029-9

29. Arpit .B. Intwala AA. REGENERATIVE BRAKING SYSTEM USING FLYWHEEL. *IJSR - Int J Sci Res.* Published online 2016.

30. Chandrakant Rahane VV. Design and fabrication of regenerative braking system. Published online 2016.

31. Burdzik R, Doleček R. *Doleček: Research of Vibration Distribution in Vehicle Constructive 16.* Vol 4.; 2012. Accessed November 23, 2020. https://pernerscontacts.upce.cz/index.php/perner/article/view/1357

32. Hendrowati W, Guntur HL, Sutantra IN. Design, Modeling and Analysis of Implementing a Multilayer Piezoelectric Vibration Energy Harvesting Mechanism in the Vehicle Suspension. *Engineering.* 2012;04(11):728-738. doi:10.4236/eng.2012.411094

33. Sultoni AI, Sutantra IN, Pramono AS. Vibration Energy Harvesting on Vehicle Suspension Using Rotary and Linear Electromagnetic Generator. *IPTEK J Technol Sci.* 2013;24(1). doi:10.12962/j20882033.v24i1.136

34. Hrovat D. Survey of Advanced Suspension Developments and Related Optimal Control Applications. *Automatica.* Published online 1997. doi:10.1016/S0005-1098(97)00101-5

35. Abdullah MA, Tamaldin N, Mohamad MA, Rosdi RS, Ramlan MNI. Energy Harvesting and Regeneration from the Vibration of Suspension System. *Appl Mech Mater.* Published online 2014. doi:10.4028/www.scientific.net/amm.699.800

36. Lin X, Xuexun G. Hydraulic transmission electromagnetic energy-regenerative active suspension and its working principle. In: *Proceedings - 2010 2nd International Workshop on Intelligent Systems and Applications, ISA 2010.* ; 2010. doi:10.1109/IWISA.2010.5473786

37. KAWAMOTO Y, SUDA Y, INOUE H, KONDO T. Modeling of Electromagnetic Damper for Automobile Suspension. *J Syst Des Dyn.* Published online 2007. doi:10.1299/jsdd.1.524

38. Zuo L, Scully B, Shestani J, Zhou Y. Design and characterization of an electromagnetic energy harvester for vehicle suspensions. *Smart Mater Struct.*

2010;19(4). doi:10.1088/0964-1726/19/4/045003

39. Martins I, Esteves J, Marques GD, da Silva FP. Permanent-magnets linear actuators applicability in automobile active suspensions. *IEEE Trans Veh Technol.* 2006;55(1):86-94. doi:10.1109/TVT.2005.861167

40. Ebrahimi B, Hamesee B. 0 - Development of Hybrid Electromagnetic Dampers for Vehicle Suspension Systems. *Dep Mech Mechatronics Eng.* 2009;Doctor of:172.

41. I. Boldea SAN. *Linear Motion Electromagnetic Devices.* Vol 0. (Taylor & Francis, ed.).; 2001. Accessed November 23, 2020. https://books.google.it/books/about/Linear_Motion_Electromagnetic_Devices.html?id=f0_XvdbL620C&redir_esc=y

42. Vincent Del Toro. *Basic Electric Machines.* Prentice Hall; 1990. Accessed November 23, 2020. https://books.google.it/books/about/Basic_Electric_Machines.html?id=59CXAAAACAAJ&redir_esc=y

43. Arshad WMTPSCBT. Integrated Free-Piston Generators: An Overview. Published online 2002. Accessed November 23, 2020. https://www.osti.gov/etdeweb/biblio/20294289

44. Wang J, Howe D. Analysis of axially magnetised, iron-cored, tubular permanent magnet machines. In: *IEE Proceedings: Electric Power Applications.* ; 2004. doi:10.1049/ip-epa:20040026

45. Ebrahimi B, Behrad ÆM. Permanent magnet configuration in design of an eddy current damper. Published online 2010:19-24. doi:10.1007/s00542-008-0731-z

46. Wang J, Jewell GW, Howe D. A general framework for the analysis and design of tubular linear permanent magnet machines. *IEEE Trans Magn.* Published online

1999. doi:10.1109/20.764898

47. Sodano HA, Bae JS, Inman DJ, Keith Belvin W. Concept and model of eddy current damper for vibration suppression of a beam. *J Sound Vib.* Published online 2005. doi:10.1016/j.jsv.2005.01.016

48. Sodano HA, Bae JS, Inman DJ, Belvin WK. Improved concept and model of eddy current damper. *J Vib Acoust Trans ASME.* 2006;128(3):294-302. doi:10.1115/1.2172256

49. Elbuken C, Khamesee MB, Yavuz M. Eddy current damping for magnetic levitation: Downscaling from macro- to micro-levitation. *J Phys D Appl Phys.* Published online 2006. doi:10.1088/0022-3727/39/18/002

50. Elbuken C, Shameli E, Khamesee MB. Modeling and analysis of eddy-current damping for high-precision magnetic levitation of a small magnet. In: *IEEE Transactions on Magnetics.* ; 2007. doi:10.1109/TMAG.2006.885859

51. Graves KE, Toncich D, Iovenitti PG. 9 - Theoretical comparison of motional and transformer EMF device damping efficiency. *J Sound Vib.* 2000;233(3):441-453. doi:10.1006/jsvi.1999.2820

52. Ebrahimi B, Khamesee MB, Golnaraghi MF. 2 - Design and modeling of a magnetic shock absorber based on eddy current damping effect. *J Sound Vib.* 2008;315(4-5):875-889. doi:10.1016/j.jsv.2008.02.022

53. Patt PJ. Design and testing of a coaxial linear magnetic spring with integral linear motor. *IEEE Trans Magn.* Published online 1985. doi:10.1109/TMAG.1985.1064088

54. Nagaya K, Sugiura M. A Method for Obtaining a Linear Spring for a Permanent Magnet Levitation System Using Electromagnetic Control. *IEEE Trans Magn.* Published online 1995. doi:10.1109/20.376226

55. Bae JS, Kwak MK, Inman DJ. Vibration suppression of a cantilever beam using eddy current damper. *J Sound Vib.* Published online 2005. doi:10.1016/j.jsv.2004.07.031

56. Furlani EP. *Permanent Magnet Applications.*; 2001. doi:10.1016/b978-012269951-1/50005-x

57. Derek J. Craik. *Magnetism: Principles and Applications | Wiley.* (Wiley, ed.).; 1995. Accessed November 23, 2020. https://www.wiley.com/en-us/Magnetism%3A+Principles+and+Applications-p-9780471954170

58. GentaDelpreteTonoli-Analyticalandexpinvestigationofamagneticradialpassivedamper-ISMB31992.pdf.

59. Ebrahimi B, Khamesee MB, Golnaraghi F. 3 - Eddy current damper feasibility in automobile suspension: modeling, simulation and testing. *Smart Mater Struct.* 2009;18(1):015017. doi:10.1088/0964-1726/18/1/015017

60. Tang X, Lin T, Zuo L. Design and optimization of a tubular linear electromagnetic vibration energy harvester. *IEEE/ASME Trans Mechatronics.* 2014;19(2):615-622. doi:10.1109/TMECH.2013.2249666

61. Shan X, Xu Z, Song R, Xie T. A new mathematical model for a piezoelectric-electromagnetic hybrid energy harvester. *Ferroelectrics.* 2013;450(1):57-65. doi:10.1080/00150193.2013.838490

62. Kunchev L, Georgiev Z. Investigation of damping properties of telescopic shock absorber and its rubber mounts in frequency range 50-150 Hz. *Eng Rural Dev.* 2019;18:936-943. doi:10.22616/ERDev2019.18.N367

63. Wikipedia. American wire gauge. https://en.wikipedia.org/wiki/American_wire_gauge